AN EXTERNAL OPTICAL MICRO-CAVITY STRONGLY COUPLED TO OPTICAL CENTERS FOR EFFICIENT SINGLE-PHOTON SOURCES

by

GUOQIANG CUI

A DISSERTATION

Presented to the Department of Physics
and the Graduate School of the University of Oregon
in partial fulfillment of the requirements
for the degree of
Doctor of Philosophy

March 2008

University of Oregon Graduate School

Confirmation of Approval and Acceptance of Dissertation prepared by:

Guoqiang Cui

Title:

"An External Optical Micro-Cavity Strongly Coupled to Optical Centers for Efficient Single-Photon Sources"

This dissertation has been accepted and approved in partial fulfillment of the requirements for the degree in the Department of Physics by:

Hailin Wang, Chairperson, Physics
Michael Raymer, Advisor, Physics
Jens Noeckel, Member, Physics
Stephen Gregory, Member, Physics
Mark Lonergan, Outside Member, Chemistry

and Richard Linton, Vice President for Research and Graduate Studies/Dean of the Graduate School for the University of Oregon.

March 22, 2008

Original approval signatures are on file with the Graduate School and the University of Oregon Libraries.

An Abstract of the Dissertation of

Guoqiang Cui for the degree of Doctor of Philosophy
in the Department of Physics to be taken March 2008

Title: AN EXTERNAL OPTICAL MICRO-CAVITY STRONGLY COUPLED TO OPTICAL CENTERS FOR EFFICIENT SINGLE-PHOTON SOURCES

Approved: _____
Dr. Michael G. Raymer

We present experimental and theoretical studies of a hemispherical, high-solid-angle external optical micro-cavity strongly coupled to nanoscale optical centers for cavity-quantum electrodynamics (QED) strong coupling and efficient single-photon sources.

Implementations of single-photon sources based on various optical centers have been reported in the last three decades. The need for efficient single-photon sources, however, is still a major challenge in the context of quantum information processing. In order to efficiently produce single photons, single optical centers are coupled to a resonant high-finesse optical micro-cavity. A cavity can channel the spontaneously emitted photons into a well-defined spatial mode and in a desired direction to improve the overall efficiency, and can alter the spectral width of the emission. It can also provide an environment where dissipative mechanisms are overcome so that a pure-quantum-state emission takes place.

We engineered a hemispherical optical micro-cavity that is comprised of a planar distributed Bragg reflector (DBR) mirror, and a concave dielectric mirror having a radius of curvature 60 μm. Nanoscale semiconductor optical centers (quantum dots)

are placed at the cavity mode waist at the planar mirror and are located at an antinode of the cavity field to maximize the coherent interaction rate. The three-dimensional scannable optical cavity allows both spatial and spectral selection to ensure addressing single optical centers. This unique micro-cavity design will potentially enable reaching the cavity-QED strong-coupling regime and realize the deterministic production of single photons. This cavity can also be operated with a standard planar dielectric mirror replacing the semiconductor DBR mirror. Such an all-dielectric cavity may find uses in atomic cavity-QED or cold-atom studies.

We formulated a theory of single-photon emission in the cavity-QED strong-coupling regime that includes pure dipole dephasing and radiative decay both through the cavity mirror and into the side directions. This allows, for the first time, full modeling of the emission quantum efficiency, and the spectrum of the single photons emitted into the useful output mode of the cavity.

CURRICULUM VITAE

NAME OF AUTHOR: Guoqiang Cui

GRADUATE AND UNDERGRADUATE SCHOOLS ATTENDED:

University of Oregon, Eugene, Oregon, USA
University of Science and Technology of China (USTC),
Hefei, Anhui, China

DEGREES AWARDED:

Doctor of Philosophy in Physics, 2008, University of Oregon
Master of Science in Physics, 2003, University of Oregon
Master of Science in Optics, 2000, USTC
Bachelor of Science in Applied Physics, 1997, USTC

AREAS OF SPECIAL INTEREST:

Classical Optics and Quantum Optics
Nonlinear Optics at Single-photon Level
Semiconductor Optical Physics
Quantum Information Science and Technology

PROFESSIONAL EXPERIENCE:

Research Assistant:
Raymer Lab, University of Oregon, 2001-2008
Teaching Assistant:
Department of Physics, University of Oregon, 2000-2001
Research Assistant:
Department of Physics, USTC, 1997-2000

AWARDS AND HONORS:

Quantum Control Summer School 2005 Travel Grant, Caltech, 2005

Japanese Enterprize Communication Network Scholarship, USTC, 1998

USTC Excellent Student Scholarship, USTC, 1997

PUBLICATIONS:

Guoqiang Cui and M. G. Raymer, "Emission spectra and quantum efficiency of single-photon sources in the cavity-QED strong-coupling regime," Phys. Rev. A **73**, 053807 (2006).

Guoqiang Cui, J. M. Hannigan, R. Loeckenhoff, F. M. Matinaga, M. G. Raymer, S. Bhongale, M. Holland, S. Mosor, S. Chatterjee, H. M. Gibbs, and G. Khitrova, "A hemispherical, high-solid-angle optical micro-cavity for cavity-QED studies," Opt. Express **14**, 2289 (2006).

Guoqiang Cui and M. G. Raymer, "Quantum efficiency of single-photon sources in the cavity-QED strong-coupling regime," Opt. Express **13**, 9660 (2005).

E. L. Blansett, M. G. Raymer, Guoqiang Cui, G. Khitrova, H. M. Gibbs, D. K. Serkland, A. A. Allerman, and K. M. Geib, "Picosecond polarization dynamics and noise in pulsed vertical-cavity surface-emitting lasers," IEEE J. Quantum Electron. **41**, 287 (2005).

ACKNOWLEDGMENTS

When I am writing this dissertation, it is just like walking that journey through time again. It was February but seven years ago, five months after crossing the Pacific ocean and half a world away from my home country, I was thinking what I really wanted to do for my Ph.D. research and started talking to faculties to look for my niche. Thanks to Prof. Michael Raymer, my current advisor, who then introduced to me this fascinating research field, quantum optics. Late in that September, I started the journey you see here in this dissertation.

I would like to first thank Prof. Michael Raymer, for his guidance, encouragement and support throughout my graduate years at Oregon. Walking through a journey like this with Mike has been a wonderful experience and the most valuable time in my life. I have always been impressed by his insights into every aspects of physics, behind the internet or in the daily life; and have been amazed, sometimes embarrassed by his questions. However, it is this critical thinking that helps prevent me from making mistakes, and helps me to go farther. I also thank him for his generous support in other aspects, particularly when I encountered roadblocks to return to Oregon to continue my study after a visit to my family in China. It was his great effort that put me back on track.

I would like to thank Prof. Hailin Wang for giving me an opportunity to work on one of his projects, to look at the physics I am interested in from a different angle, from which I benefited a lot. I have greatly enjoyed our discussions, both scientific and technical. I would also like to thank Prof. Jens Nöckel for constructive discussions on theoretical aspects of optical resonators, whether having a dimple in it or being a sphere. Thanks to Prof. Stephen Gregory, by his email eight years ago I was advised that I was admitted to the Ph.D. program at Oregon. Eight years later, I am still

getting his advice. Thanks to Prof. Mark Lonergan for helpful suggestions and for letting us use his lab equipment, for which many parts of this experiment were able to be made.

Thanks to Dr. Ethan Blansett, who supervised my first project in the Raymer lab, and for his many helps years afterwards. Thanks to Justin Hannigan, with whom I have been working for almost my entire Ph.D. life. Together we experience every phase of this journey: lows and highs, pain and joy, failure and success. My thanks also go to other fellows in the Raymer lab who have been a help. It is a true pleasure to work in such an open and collaborative environment.

Of most importance and above all is my family, thanks to my wife Qian, my parents and my sister for loving me. How could it be possible for me to go this far without your support, encouragement and patience? I love you all. I dedicate this dissertation to my late grandfather. I was not able to stand by him when he was badly ill, and hope that the completion of this dissertation could fulfill his last wish. May he rest in peace.

To my wife Qian Ye

and our parents

TABLE OF CONTENTS

Chapter Page

Chapter Page

LIST OF FIGURES

Figure Page

Figure Page

Figure Page

CHAPTER I

INTRODUCTION

In this opening chapter, we first review the motivation why we chose this research topic, namely an optical micro-cavity strongly coupled to optical centers, semiconductor quantum dots (QDs) in this research, for efficient single-photon sources (SPS). Following this we give an introduction to the problem and identify what the tasks are, both scientific and technological, to be accomplished. Oriented by the objective, we then describe how to develop the methodology and construct the tools that are necessary to solve the problem. That is: designing and constructing a composite micro-cavity-QD system; understanding the essential dynamics of the interacting cavity-QD system; and developing the theoretical models to define and optimize the quantum efficiency for a SPS. Then, we give the goal and show the accomplishment of this dissertation: what goal we want to reach, what we have accomplished and what foundation we have laid down that is necessary for the future work, before pointing out the challenges. Finally we outline the organization of this dissertation.

1.1 Motivation

The study of optical cavities or resonators has a long history that can be dated as far back as 1897 by Charles Fabry and Alfred Pérot using a transparent plate with two reflecting surfaces, namely a Fabry-Pérot interferometer [1]. Such a device confines light in a volume by resonant recirculation, and due to the effect of multiple beam interference, only certain spatial patterns and frequencies of light field will be sustained while others are suppressed. The Fabry-Pérot interferometer turned out to

be a convenient resonator system in more than one respect, which accounts for its still remaining one of the most widely used geometries for optical resonators.

New physical processes appear as the physical sizes of the optical resonators approach the wavelength of the light. This has resulted in the concept of the micro-cavity. Quality factor (Q) and mode volume figure prominently in applications of these devices. The Q of a cavity is proportional to the confinement time in units of optical period or inversely to the energy dissipation rate relative to the oscillation frequency. Due to its small mode volume along with a high Q, not only does a micro-cavity modify the modes of the vacuum dramatically, giving more sparsely distributed resonant frequencies than that of a macro-cavity, but also changes the radiative behavior of an atom or a semiconductor QD or any optical centers placed inside it. We define optical center as an object, or certain bound electric charges within an object, that could radiate photons at optical frequencies when interacting with electromagnetic fields. For example, an atom, a molecule or an ion, or single defects or color centers in semiconductor nano-structures and diamonds; or either bound electron-ion pairs or bound electron-hole pairs in these objects. The research of high Q, small mode volume optical micro-cavities has been a distinct subject dominating the past decades [2, 3, 4].

As cavities have been reduced in sizes from the conventional Fabry-Pérot micro-cavities having two separable dielectric mirrors [5], with continued improvement in micro-fabrication techniques, the solid-state integrated Fabry-Pérot structure consisting of two semiconductor distributed Bragg reflector (DBR) mirrors have been developed and widely used for vertical-cavity surface-emitting lasers (VCSELs) [3]. A hybrid external Fabry-Pérot micro-cavity consisting of one dielectric mirror and one semiconductor DBR mirror has also been developed recently in our group [6]. Active optical centers such as semiconductor QDs, are incorporated in the cavity for studying light-matter interaction. This is the main topic and focus of this

dissertation. Moreover, other optical centers such as color centers in diamond may also be integrated in such an optical cavity.

In addition to the size reduction, the geometries of optical micro-cavities have been differentiated to various types such as whispering gallery [7] and photonic crystal [8] resonators. Whispering gallery resonators are typically but not limited to dielectric spherical [9] or toroidal [10] structures in which waves are confined by continuous total internal reflection (TIR). The modes of the micro-sphere and micro-toroid resonators are called whispering gallery modes (WGMs) feature ultra-high Q, due to the formation of these structures through surface tension, providing a near atomically smooth surface. Generically, a planar photonic crystal was proposed, which is essentially a two-dimensional (2D) photonic crystal with a finite third dimension. One typical example is an optically thin slab surrounded with lower refractive index material and pattered with a 2D lattice of holes. In such a structure, light is confined in the lateral direction by distributed Bragg reflection, while in the vertical direction by conventional waveguiding or TIR. The modes of the photonic crystals are called defect modes, due to a 'defect', relative to otherwise periodic structure introduced in the 2D lattice. Micro-resonators based on these structures can provide extremely small mode volumes [11]. At present, however, Q values in fabricated photonic crystals are well below theoretical optima [12, 13].

Each of these type of resonators has their own advantages and disadvantages. For the purpose of optical mode coupling, Fabry-Pérot cavities can be free-space coupled in and out along the cavity axis efficiently. For WGMs, however, input beams must be phase matched in order to excite those ultra-high Q modes, which is typically achieved using TIR from the back face of a prism or an optical fiber taper. Other coupling methods such as free-space coupling into a slightly deformed sphere have also been demonstrated [14]. For the application with ultra-high Q modes, there are technological limits imposed by mirror technology in optimizing Fabry-Pérot micro-cavities for cavity quantum electrodynamics (QED) strong coupling

[15]. As noted earlier, photonic crystal defect micro-cavities can provide extremely small mode volumes and large theoretical Q values for certain design, however, the fabricated structures have much lower Q values due to surface roughness introduced in the lithography process. Nonetheless, these optical resonators have found their applications in areas as diverse as optical telecommunication, nonlinear optics, chemical physics, biological and chemical sensing, quantum optics, and cavity QED [16, 2, 3, 4].

Beyond their already important roles in commercial technologies, such as VCSELs, optical micro-cavities are destined to become an essential ingredient in the emerging field of quantum information science and technology. The optical resonator has a size- and geometry-dependent resonant frequency spectrum, upon which the applications strongly depend. For instance, at wavelength-sized cavities, enhanced and suppressed spontaneous emission, squeezed states and chaos are readily observed. More interestingly, if an atom or any other optical center interacts so strongly with a single mode of a micro-cavity that the coherent interaction rate overwhelms all other dissipations to enter the cavity-QED strong-coupling regime [16], a quantum entangled atom-cavity system is possible. Such a system is crucial for a number of applications in quantum information processing (QIP) [17, 18, 19]. Controlling the emission of single photons for example, has been a priority for quantum encryption systems, which is also one of the major practical motivations for this research.

Conventional sources of light, such as light-emitting diodes (LEDs) and lasers, usually consist of a macroscopic number of photons and have a statistical distribution, for instance Poisson statistics in the number of photons. On the other hand, many applications in quantum information science (QIS) require efficient optical sources with strong correlations between single photons. For example, encoding information on single photons provides a means to test the security of optical communications, which could soon be applied to the problem of sharing secret key in quantum cryptography [20]. Although quantum-key-distribution systems based on faint laser

pulses have already been realized for simple point-to-point links, a true single-photon source, an optical source emitting a train of pulses that contain one and only one photon, would improve its ultimate security [21, 22]. Furthermore, a single-photon source that can also produce entangled photon pairs, is important for future quantum communication protocols, such as quantum teleportation—the transfer of an unknown quantum state from one object to a like object [23]. Here quantum networks sharing entanglement could be used to distribute keys over longer distances or through more complex topologies [24].

It is relatively straightforward to use single photons for quantum cryptography and communication. It is not easy, however, to apply single photons for quantum computation because single photons do not interact strongly with each other, which is a prerequisite for a quantum logic gate. Linear-optics quantum computing (LOQC) [25], on the other hand, can get around this problem by using all-linear optical elements such as mirrors and beam splitters plus projective measurements to introduce an effective interaction between the photons. One of the stringent requirements is a high-efficiency SPS, in addition to another crucial requirement that photons be produced in pure states. Please note for secure quantum key distribution, it is important to have a high-efficiency SPS, but is not required for this application that photons be in pure states; but for LOQC, it is required to be able to produce pure-state single-photon wave-packets on demand. These photon packets can then be made to interfere with high visibility, leading to effective quantum computing. Other than the potential applications in QIP, a true single photon source will also become increasingly important for other applications such as weak absorption and precision optical measurements [26, 27, 28] and random number generation [29].

Semiconductor materials offer many potential advantages for efficient single- and pair-photon generations, including high speed, tailored properties and device integration, other than already extensive studies in nonlinear optics and cavity QED [30, 31] and their applications in laser industry. Furthermore, they are optically

addressable and potentially offer scaling up using nanofabrication. One of the quantum systems based on semiconductor materials, semiconductor QDs, or confined electron-hole pairs, are often referred to as 'artificial atoms', as their electron motion is quantized in all three directions, resulting in a discrete energy-level spectrum like that of an atom. In just a few years, remarkable progress has been made in generating indistinguishable single photons and entangled-photon pairs using such structures [32]. It seems possible to realize compact, robust, LED-like semiconductor quantum light sources in the near future. An efficient SPS exploiting semiconductor QDs, however, requires the ability to integrate a single QD with an optical micro-cavity and locate it at an antinode of the cavity field, as this ensures the largest possible coupling and removes background emission, as well as other undesirable effects due to other dots in the cavity.

We believe that before the eventual advent of the all solid-state semiconductor devices for single-photon sources and for QIP, it is important to study the physics of strongly coupled cavity-QD system for single-photon sources using a flexible system such as presented in this dissertation. All these concerns motivated us at the beginning to choose this research topic, and now result in the successful design and construction of a system to incorporate semiconductor QDs into an external optical micro-cavity for efficient SPS, preliminary experimental results showing signatures of significant cavity-QD interaction, and a theory formulated to understand the dynamics of a strongly coupled cavity-QD system and to optimize the quantum efficiency of a single-photon source in the cavity-QED strong-coupling regime.

1.2 Introduction to the Problem

Albeit various implementations of SPS based on atom-like optical centers have been reported based on different systems in the last three decades, such as calcium atoms [33], single ions in traps [34], single molecules [35], a color center in diamond [36], and semiconductor nanocrystals [37] or QDs [38, 39], the need for efficient

single-photon sources, however, is still a major challenge in the context of QIP [40, 41]. In order to efficiently produce single photons on demand, the single optical center is coupled to a resonant high-finesse optical cavity. A cavity can channel the spontaneously emitted photons into a well-defined spatial mode and in a desired direction to improve the collection efficiency, and can alter the spectral width of the emission. It can also provide an environment where dissipative mechanisms are overcome so that a pure-quantum-state emission takes place [42]. The major questions are: how to integrate single optical centers into a cavity and make the interaction strong, what is the dynamics of the interacting single optical centers with a single cavity mode, what are the emission spectra of the composite system when the coherent interaction overwhelms dissipations, and what is the quantum efficiency (QE) of the emission from on such a system?

Achieving cavity-QED strong coupling in semiconductor QD systems is itself very interesting [43], following early studies using planar quantum-well cavity systems, which themselves cannot reach this regime [30]. Cavity-QED strong coupling is also necessarily required for efficient and pure-quantum-state single photons emission. Recent experiments showed signatures of strong coupling in some monolithic semiconductor structures such as micro-pillar [44], photonic crystal nano-cavity [45], micro-sphere [46] and micro-disk [47, 48]. Obvious advantages of using QDs in such schemes are that the QDs stay in a solid-state system and are stationary and do not move a lot as atoms do. Beside, they can be optically or electrically addressed and pumped [39]. The principal disadvantages in these monolithic structures, however, are the lack of efficient control of the spatial and spectral overlap between QDs resonance and cavity modes. It needs careful design followed by a precise fabrication procedure to preset these conditions. It is also challenging to address single QDs spatially and tune the cavity-QD resonance or change samples once a structure has been fabricated. For instance, temperature tuning of the QD has to be used to tune through cavity resonance [44, 45, 47], which

is undesirable because the dipole dephasing rate increases at elevated temperatures [49, 50].

Therefore, the problems may be nailed down to: first, how to incorporate optical centers into a micro-cavity and make them overlap with cavity modes both spatially and spectrally; second, how to design and engineer a composite cavity-optical center system such that the coherent interaction overwhelms all other dissipations to maximize the useful light-matter interaction; third, what is the emission spectra and QE in the useful cavity direction of SPS in the cavity-QED strong coupling regime; fourth, how does the pure dephasing affect the emission spectra and QE when it is introduced unavoidably?

1.3 Dissertation Goal and Accomplishment

This dissertation provides one of the many elegant but unique methods to address the above questions. We chose molecular beam epitaxy (MBE)-grown semiconductor QDs as our optical centers and a hemispherical design for our micro-cavity, taking advantage that, first, high quality semiconductor mirror can be grown by MBE; second, relatively large oscillator strength semiconductor QDs can be grown by interface fluctuation in a one-wavelength spacer layer on top of the mirror; third, a hemispherical optical micro-cavity gives a diffraction-limited beam size at the location of QDs and hence a small mode volume. With the experimental design, we expect to reach the cavity-QED strong-coupling regime, which is challenging by itself, and to make efficient single-photon sources. Theoretically, we want to study the dynamics of the strongly coupled cavity-QD system, the emission spectra and the quantum efficiency of the composite system based on realistic experimental parameters in the cavity-QED strong-coupling regime.

This dissertation presents experimental and theoretical studies of a hemispherical, high-solid-angle, external optical cavity strongly coupled to nanoscale optical centers for cavity-QED strong coupling and efficient production of single photons on demand.

By taking advantages of standard semiconductor growth and processing techniques, our collaborators (H. Gibbs and G. Khitrova) were able to grow QDs formed by interface fluctuation in a thin quantum well and integrate them into a high-reflectivity mirror as one side of the micro-cavity. Furthermore, by design we locate the QDs at an antinode of the cavity field to maximize the interaction. The external cavity approach provides maximum flexibility in scanning laterally to position a QD at the focus of the cavity, as well as providing the capability of scanning the cavity resonance to the spectral position of the isolated QD.

We engineered a hemispherical, high-solid-angle optical cavity [6] that is comprised of a planar semiconductor DBR mirror, and a concave dielectric mirror having a radius of curvature 60 μm. Nanoscale optical centers such as semiconductor QDs are placed at the cavity mode waist at the planar mirror and are designed to be located at an antinode of the cavity field to maximize the coherent interaction. The three-dimensional scannable optical cavity allows both spatial and spectral selection to ensure addressing single optical centers. This unique hybrid micro-cavity design will potentially enable reaching the cavity-QED strong-coupling regime and realize the deterministic generation of single photons on demand.

We formulated a theory using Weisskopf-Wigner method to calculate the emission spectra of interacting cavity-QDs system and the quantum efficiency of single-photon emission in the cavity-QED strong-coupling regime [51] that includes pure dipole dephasing and radiative decay both through the cavity mirrors as well as into the side directions [52]. This allows, for the first time, full modeling of the emission quantum efficiency, as well as the spectrum of the single photons emitted into the useful output mode of the cavity.

Our cavity can also be operated with a standard planar dielectric mirror replacing the semiconductor DBR mirror. Such an all-dielectric cavity may find uses in atomic cavity-QED or cold-atom studies [53], or novel forms of microscopy or interferometry. Atom chips were recently reported using similar hybrid Fabry-Pérot resonators [54].

Other optical centers such as color centers in diamond may also be incorporated in such a cavity. The challenge mainly lays in the stringent fabrication conditions for growing diamond nanocrystals in thin films.

1.4 Dissertation Organization

The dissertation is organized as follows. In Chapter II, we first overview the concept of single-photon sources and the method to generate efficient single-photon sources using a single optical center inside a high-finesse optical micro-cavity. Two light-matter interaction regimes, weak coupling and strong coupling, are discussed. Following that, we describe the advantages to use the hemispherical design and the hybrid dielectric-semiconductor mirror combination for the cavity. Then we discuss the advantages of the interface fluctuation QDs in a thin QW for cavity-QED studies and the MBE growth method to integrate them with a DBR mirror. Finally, we briefly review the physics of designing a DBR mirror to locate optical centers at an antinode of a light field.

In Chapter III, we first describe the detailed procedure to fabricate micro-sized concave mirrors and how to estimate their physical parameters such as the dimple depth and the radius of curvature. Then we discuss the optical coating design for such a highly curved mirror to give a reflectivity of 99.5% or higher over a high-solid angle range. After assembling the micro-cavity onto a sophisticated mechanical system located inside an ultra-high vacuum chamber, we characterize the cavity by investigating mode-matching of a laser beam into a cavity mode and probing the cavity mode structure. Finally, we show some preliminary spectroscopic results of cavity transmission spectra at both room temperature and cryogenic temperatures.

In Chapter IV, using the Weisskopf-Wigner theory for an impulse-excited optical center, we derive analytical formulas for the forward emission and side emission spectra of cavity-modified single-photon sources, as well as the corresponding vacuum Rabi oscillations in the cavity-QED strong-coupling regime. We calculate

the integrated-pulse quantum efficiency of a single-photon source. An analytical expression for the quantum efficiency is obtained. Optimal conditions for a high quantum efficiency and a temporally localized photon emission rate are examined.

In Chapter V, we investigate the effects of pure dephasing, treated in the phase-diffusion model based on a Wiener-Levy process, on the vacuum Rabi oscillations, quantum efficiency and emission spectra, and extend our results in Chapter IV to include the pure dephasing process. We find that the depths of the vacuum Rabi oscillations are reduced, the quantum efficiency is decreased and the spectra are broadened in the presence of pure dephasing.

In Chapter VI, the last chapter, we summarize and conclude the dissertation and give an outlook for the future work.

CHAPTER II

OVERVIEW OF CONCEPTS AND SYSTEM

In this chapter, we first give an overview of concepts of a single-photon source and using a single optical center interacting with an optical micro-cavity for efficient production of single photons. The dynamics of the composite system can be different, depending upon the coupling strength between an optical center and a cavity mode. Two different light-matter coupling regimes, strong- and weak-coupling regimes, are considered. The different efficiencies that determine the overall efficiency of a single photon source are discussed. Then we give a description of a physical system we designed and constructed that is suitable for fulfilling the purpose. Finally we give a brief review of how to design a distributed Bragg reflector (DBR) mirror and how to integrate optical centers with it.

2.1 Overview of Concepts

In 1900, when trying to explain the experimentally observed black-body spectrum, the spectral distribution of the electromagnetic energy radiated by a thermal source, Max Planck found that he could account for the measurements by assuming that the electromagnetic energy E could be emitted only in quantized form [55]. In other words, the energy could only be an integer multiple of an elementary unit $E = h\nu$, or a quantum of electromagnetic radiation, where h is Planck's constant, and ν is the frequency of the radiation. The concept of photon, however was not introduced until 1905 by Einstein to interpret the photoelectric effect [56]. The word 'photon' is now widely used to describe a quantum of electromagnetic radiation, or a minimum-energy packet of electromagnetic radiation. Although there were some arguments in the past

[57] for its usage, it is now largely adopted by the quantum-optics community. One of the most common classical light sources is a thermal source, a light source in thermal equilibrium at a certain temperature, described by Planck's law. The photon number distribution in such a source falls off monotonically with increasing photon number, and is naturally called the thermal distribution or the geometric distribution. It reflects the chaotic nature of a thermal source, as compared with other light sources such as a laser.

In 1916, Einstein laid the foundation for the invention of the laser, which also consists of a macroscopic number of photons, and its predecessor the maser, in a ground-breaking re-derivation of Max Planck's law of radiation based on the concepts of spontaneous and stimulated emissions [58]. The laser, however, was not made until much later in 1960s. Theodore H. Maiman at Hughes Research Laboratories in Malibu, California invented the first working laser in 1960 [59]. The concept of the laser diode was proposed by Nicolay G. Basov in 1959 [60]. A laser diode is a laser where the active medium is typically a semiconductor p-n junction. The first semiconductor laser diode was demonstrated by Robert N. Hall three years later [61]. The early semiconductor lasers, however, could be used only in pulsed operation, and indeed only when cooled to liquid nitrogen temperatures. In 1969 and 1970, Zhores I. Alferov et al. in the Soviet Union and Morton B. Panish et al. of Bell Telephone Laboratories independently developed continuously operating laser diodes at room temperature [62, 63]. The photon number distribution of a laser follows a Poisson distribution, indicating the randomness of the light source. So what is a single-photon source?

2.1.1 Single-photon Sources

Right after the invention of lasers, mainly under Roy J. Glauber's impulsion [64], researchers began to look for specific quantum properties of light that could not be understood in a classical regime. For his contribution to the quantum theory of

optical coherence [65], Glauber shared the 2005 Nobel Prize in Physics. In his work [64], published in 1963, he created a model for photodetection and explained the fundamental characteristics of different types of light, such as a laser light and an ideal single-photon source. Photons in a laser beam follow a Poisson distribution, which refers to the statistical tendency for photons to arrive at a detector randomly. An ideal single-photon source will deliver one and only one quantum of light each time it triggered, which is referred to as antibunching effect, in contrast to a laser. The photon number distribution of a true single photon source is said to be the sub-Poisson distribution, since that of a laser exhibits a Poisson distribution.

One straightforward and maybe naive method to approximately produce single photons is to properly attenuate a pulsed laser such that there is on average only one quantum of light equivalent energy per pulse. However, such strongly attenuated laser pulses differ from 'true' single photons in at least two respects: first, the vacuum probability is much higher than the probability of detecting a photon, so one gets predominantly a 'no-photon' regime with occasional detection of a photon; second, the probability of getting two photons is never zero, because the attenuated pulses are still in coherent states and essentially follow a Poisson distribution. There are other approximated single photon sources: heralded single photons from atomic cascade, spontaneous parametric down-conversion, and spontaneous four-wave mixing [66]. They will be discussed later.

A single-photon source can be achieved using the spontaneous emission of a single optical center, such as an atom in gaseous phase. Early successful generation of single photons showing the antibunching effect was performed using heralded photons based on cascade transitions of calcium atoms, followed by proper spectral filtering and conditional detection [33, 67]. Single photons were also observed in the resonance fluorescence from an attenuated sodium atomic beam, where at most one atom was present in the excitation focus at any time [68]. Although the cascading calcium atoms and the faint sodium beam were the first sources of single photons, their brightness

and efficiency were very low, and a further drawback was that the operation of the source was limited by the density and transit times of the atoms, and could not be controlled.

In parallel, a different mechanism to generate single photons based on nonlinear optical processes had also been developed about at the same time. Optically pumping a nonlinear crystal using a He-Cd laser, pairs of photons, signal and idler photons, highly correlated both in space and time were generated at high rates by spontaneous parametric down-conversion in 1970 [69]. A similar nonlinear process, spontaneous four-wave mixing has also been used to generate correlated pair photons. Provided that the probability of generating two pairs at the same time remains negligible, such correlated pairs can be used as sources of heralded single photons [70]. Please note that in the absence of a convenient way to produce controllable single-photon sources, the parametric sources played an important role in most early experiments in quantum optics [71, 72, 73, 74, 75] and are still the workhorses to date [76, 77].

It is preferable to generate single photons in a controllable fashion like a 'photon gun', an ideal device that delivers photons one by one and is synchronized with an external excitation and trigger source. From the mid-1980s, single ions in magnetic traps provided long observation times with one and the same ion [34]. The long streams of antibunched photons produced in this way came closer to a photon gun, but by no means close enough to a 'photon gun'.

Due to the sensitive detection of fluorescence in single molecules [78] and in single semiconductor heterostructures [79, 80] in the early 1990s, single-photon emissions were detected from single molecules [35] and in other single nano-objects in condensed matter. Since in condensed matter, single objects are much easier to be manipulated as compared to the atoms and ions in gaseous phase, nano-objects were therefor proposed as possible sources of single photons [81, 82]. Soon after, single-photon emissions from semiconductor nanocrystals [83, 84, 85], color centers in diamond [86, 36], single QDs in various geometries [37, 38] and much more were reported.

For most of the applications in QIP, single-photon sources that generate pure single-photon states on demand in response to an external trigger signal are required. Antibunching is an essential test of single photons. But it only means that the probability of emitting two or more photons per trigger is zero and is not sufficient for creating single photons on demand. In addition, we require that the source emits one photon with certainty. That is, the excited state of the optical center must be prepared with certainty, and the emission quantum efficiency need to be unity or as close to it as possible. Other crucial performance measures for an on-demand source are the overall efficiency of such a source, which is the product of the excitation efficiency, quantum efficiency, collection efficiency and detection efficiency which is defined as the fraction of photons collected and detected in the experiment per trigger, and the indistinguishability of single photons emitted from the source at different times.

Then the question is how to meet these requirements and reach the goal. We start with spontaneous emission in free space. Consider a one-electron atom with two electronic levels $|e\rangle$ and $|g\rangle$ separated by an energy interval $E_e - E_g = \hbar\omega_0$. Spontaneous emission appears as a jump of the electron from level $|e\rangle$ to $|g\rangle$ accompanied by the emission of a photon, which can be emitted into any directions. The spontaneous emission process can be understood as resulting from coupling of an atomic electron to the electromagnetic field in its vacuum state. Typical only a fraction of spontaneously emitted photons can be collected and detected, depending upon how large a solid angle is subtended by the collection and detection optics. An essential feature of spontaneous emission in free space is that a photon can be emitted into any mode that enables the conservation of energy and momentum. The time of emission and the particular mode in which the photon is observed are random.

As pointed out above, spontaneous emission is not an intrinsic atomic property, but rather results from the coupling of an atom to the vacuum modes of the electromagnetic field. The most distinctive feature of spontaneous emission is its irreversibility, which comes about because an infinity of vacuum states is available to

the radiated photons. As such, it can be modified by tailoring the electromagnetic states into which the atom can radiate, for instance, by placing an excited atom into a cavity.

The spontaneous emission rate can be enhanced if an atom at rest inside a cavity is resonant with one of the cavity modes [87]; it can also be inhibited if the mode density to which the spontaneous emission is small compared with that in free space [88]. It has also been recognized that spontaneous emission need not be an irreversible process. Indeed, the Schödinger equation always leads to reversible dynamics. Spontaneous decay only appears to be irreversible when the electromagnetic field modes are treated as a Markovian reservoir. If the vacuum modes can not be approximated in this way, qualitatively different types of dynamics can be achieved. Depending upon the ratios of the coherent interaction rate between an optical center and an optical cavity, to the intracavity field decay rate, and to the optical center population decay rate, one can distinguish two regimes of coupling between an optical center and a cavity: strong-coupling and weak-coupling regimes, which are to be discussed in more detail in the following.

In the cavity-QED weak-coupling regime, where the dissipations are still greater than the coherent interaction rate, an optical cavity can channel the spontaneously emitted photons into a well-defined spatial mode and in a desired direction to improve the out-coupling and collection efficiency, and can alter the spontaneous emission rate and the spectral width of the emission. Only if it is coupled to a resonant mode of a high-Q optical cavity, can an optical center realize its full potential as an efficient single-photon emitter. An optical cavity can also provide an environment where dissipative mechanisms are overcome to enter the cavity-QED strong-coupling regime so that a highly-pure-state single-photon emission takes place.

One of the most feasible approaches to the efficient creation of single photons in a well-defined mode is believed to be placing an optical center at an anti-node of the field in a high-finesse optical micro-cavity and optically exciting the optical center at

a known time. In the limit of strong coupling, the ensuing process of spontaneous emission becomes deterministic. That is, the coupling of the optical center's dipole to a privileged cavity mode is far stronger than its coupling to all other modes. Then there will be virtually no emission into the other modes. In addition, there needs to be almost no dephasing of the dipole during the emission process. In this case, the photon is emitted through the cavity mirror in a known, pure wave-packet state that has a well-defined time delay following the excitation. These wave-packets are also emitted as a Gaussian beam in a well-defined direction and can be efficiently coupled out of the cavity and into the subsequent optics. Photon correlation and indistinguishability can be tested with Hanbury-Brown and Twiss (HBT) [89] type photon correlation measurements or balanced-homodyne detection (BHD) [90].

2.1.2 Cavity-QED Weak Coupling versus Strong Coupling

In order to examine and justify the claims made above, we start with a theoretical model of light-matter interaction. The majority of the optical phenomena involving light-matter interaction is the coupling of a two-level optical center with a single mode of an electromagnetic field. The elementary system in cavity QED is a two-level optical center, an atom or QD, interacting resonantly with a single cavity mode as in Fig. 2.1. We know an atom or QD is not a system with only two energy levels, but really multiple levels. A two-level optical system description is valid if the two energy levels involved are resonant or near resonant with the driving field or the cavity mode, while all other levels are highly detuned.

Under certain realistic approximations, an optical center behaves as a simple harmonic oscillator, which couples to the electromagnetic field through its electric moment, typically electric-dipole moment. The electric-dipole interaction energy that results when an atom or QD interacts with a cavity mode is $H_{vac} = \vec{\mu}_{eg} \cdot \vec{E}_{vac}(\vec{r}_0) \equiv \hbar g_0$. Here $\vec{\mu}_{eg}$ is the electric dipole moment for an atomic or excitonic transition and $\vec{E}_{vac}(\vec{r}_0)$ is the electric field vector associated with the vacuum or quantum mechanical

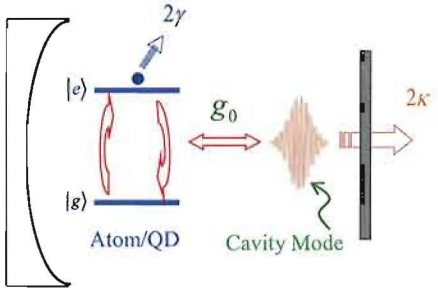

FIGURE 2.1: Schematic description of a lossy two-level optical center interacting with a single mode in a leaky optical cavity. g_0 is the coupling constant between the optical center and the cavity field. 2γ and 2κ are the optical center population decay rate to the sides of the cavity and the cavity field decay rate, respectively.

zero-point motion, at the location of the optical center $\vec{r}_0$. And g_0 is the vacuum Rabi frequency in unit of rad/s. The vacuum-field vector is given by

$$\vec{E}_{vac}(\vec{r}_0) = \sqrt{\frac{\hbar\omega_c}{2\varepsilon_0}}\vec{U}(\vec{r}_0), \tag{2.1}$$

where $\vec{U}(\vec{r}_0)$ is the normalized spatial distribution of the mode's electric field vector. The cavity effective mode volume, V_{eff}, which depends on the location of the optical center $\vec{r}_0$, is defined as the spatial integral of the field intensity, normalized to unity at the maximum,

$$\int |\vec{U}(\vec{r})|^2 d^3r = 1 \equiv |\vec{U}(\vec{r}_0)|^2 \times V_{eff}, \tag{2.2}$$

where the integral is over all space ($\vec{r}$) between the cavity mirrors.

For example, if the mode amplitude can be described as a (paraxial) Gaussian function with 1/e amplitude contours that define a spot size $w(z)$ at the position z along the cavity axis as, and with the field maximized at the boundaries, then

$$|\vec{U}(\vec{r})| = U_0 \frac{\cos(kz)}{w(z)} e^{-\frac{x^2+y^2}{w^2(z)}}, \tag{2.3}$$

where U_0 is a complex number containing the phase information. Plug Eq. (2.3) into Eq. (2.2), and let $\rho^2 = x^2 + y^2$, then we get

$$\int dz |U_0|^2 \frac{\cos^2(kz)}{w^2(z)} \int d\phi \int \rho d\rho \exp\left[-\frac{\rho^2}{w^2(z)}\right] = 1 \equiv |\vec{U}(\vec{r}_0)|^2 \times V_{eff}. \tag{2.4}$$

Then the cavity effective mode volume is,

$$V_{eff} = \frac{1}{4}\pi w_0^2 L, \tag{2.5}$$

where w_0 is the beam waist, L is the cavity length and it is assumed that the optical center is located at an antinode of the standing wave. Clearly we need to make the beam waist and the cavity length both as small as possible, and make certain that the optical center is located at an antinode near the waist.

If we assume the electric-dipole transition is in the electric field direction ($\hat{x}$) with matrix element μ_x, having frequency ω_0, resonant with the cavity mode with frequency ω_c, then the coupling constant g_0 is related to the cavity effective mode volume V_{eff} by

$$g_0 = \mu_x \sqrt{\frac{\omega_c}{2\hbar\varepsilon_0 V_{eff}}}. \tag{2.6}$$

The atomic or excitonic transition also has a dipole decay (dephasing) rate γ. Here we consider only the radiative decay, not including the non-radiative decay. The cavity decay rate is 2κ given by the total mirror transmission-plus-scattering loss $T+S$ and the cavity length L through

$$2\kappa = \frac{c}{2L}(T+S). \tag{2.7}$$

Cavity-QED weak coupling results when dissipation overwhelms the coherent Rabi dynamics. In this regime, the main role of the micro-cavity is to control the spontaneous emission through the Purcell effect, determined by the ratio of the spontaneous rate inside the cavity to that in free space, to enhance radiative decay into a cavity mode of interest and thereby achieve a stream of single-photon pulses. The Purcell spontaneous emission enhancement factor is given by [87]

$$F_p = \frac{3\lambda^3}{4\pi^2}\frac{Q}{V_{eff}} \tag{2.8}$$

where the $Q = (2L/\lambda)\mathcal{F}$ is the cavity quality factor with a cavity finesse $\mathcal{F}$, and V_{eff} is the effective volume of the interacting mode. If the cavity has a preferential output

direction, the Purcell effect will ensure fast and directional emission from the two-level system. These features are highly desirable for improving the overall emission efficiency of single photons. In this regime, for instance, Santori et al. [91] showed the ability to produce largely indistinguishable photons by a semiconductor QD in a micro-cavity using a large Purcell factor.

Cavity-QED strong coupling occurs when the electric-dipole interaction rate between an atom or QD and a single, unoccupied mode exceeds the energy decay rates of the composite system. It means that the coherent coupling frequency g_0 is greater than the cavity and atom or QD decay rates, assuming no atomic or excitonic pure dephasing,

$$g_0 \geq \kappa, \gamma. \tag{2.9}$$

In the super-strong coupling limit, $g_0 \gg \kappa, \gamma$, coherent dynamics (Rabi dynamics) takes place on time scales much shorter than the dephasing times. Use of a weak optical probe reveals that the presence of the QD splits the cavity's transmission spectrum into two distinct peaks, which correspond to eigen-frequencies of the quantum entangled cavity-QD states (states that are not factorable into cavity and QD components).

In the cavity-QED strong-coupling regime, a single photon can saturate an atomic or excitonic state of an optical center, allowing coherent control over the internal state of the optical center; and furthermore the optical center can strongly influence the optical field in the cavity, enabling transfer of information from matter to field. For example, in the cavity-QED strong-coupling regime, one potential application is for quantum communication, where optical centers serve as stationary quantum bits (qubits) storing information while photons as flying qubits transfer information from one storage location to another. The other priority is to control the emission of single photons to deterministically produce single photons on demand. The realizations of cavity-QED strong coupling in the atom-cavity [5] and QD-cavity systems [44, 45, 47, 48] allow researchers to deterministically generate single photons [92, 93, 42]. It is also

possible to observe (even weak) nonlinear optical effects [94] in these strongly coupled systems to provide a mechanism for quantum logic and quantum computation.

The quantum efficiency of a SPS, which is intrinsic to the composite quantum system, can be different in these two regimes because the dynamics of the composite system are different. The overall efficiency of a SPS will also depend on the excitation efficiency [95], collection efficiency and detection efficiency, which are not intrinsic to the composite quantum system; however, they can be greatly affected by the energy structure of the optical center and the geometry of the cavity.

In this dissertation, we intend to exploit a novel approach for generating single photons on demand using a single semiconductor QD interacting strongly with a mode of a hemispherical optical micro-cavity. Why did we choose this approach? As we have already said in Chapter I, we believe that before the eventual advent of the fully integrated and scaled up devices for on-demand production of single photons, it is important to study the physics of strongly coupled optical center/cavity system using a flexible composite system, an external optical micro-cavity with semiconductor QDs. Besides, other solid-state optical centers such as color centers in diamonds may also be integrated in such a cavity for efficient single photon sources. In the next section, we will give a detailed description of our system.

2.2 Overview of System

We have successfully designed and constructed a small-effective-volume, low-f-number, high-Q hemispherical micro-cavity as in Fig. 2.2. In such a geometry the cavity effective volume is given by Eq. (2.5). The minimum mode radius w_0 that is allowed by diffraction in such an open cavity is of the order of one-half the optical wavelength.

The composite cavity-QD system that we use is comprised of an integrated semiconductor distributed Bragg reflector (DBR) mirror adjacent to the QD layer, at the focal plane of a hemispherical dielectric mirror, having a radius of curvature 60 μm.

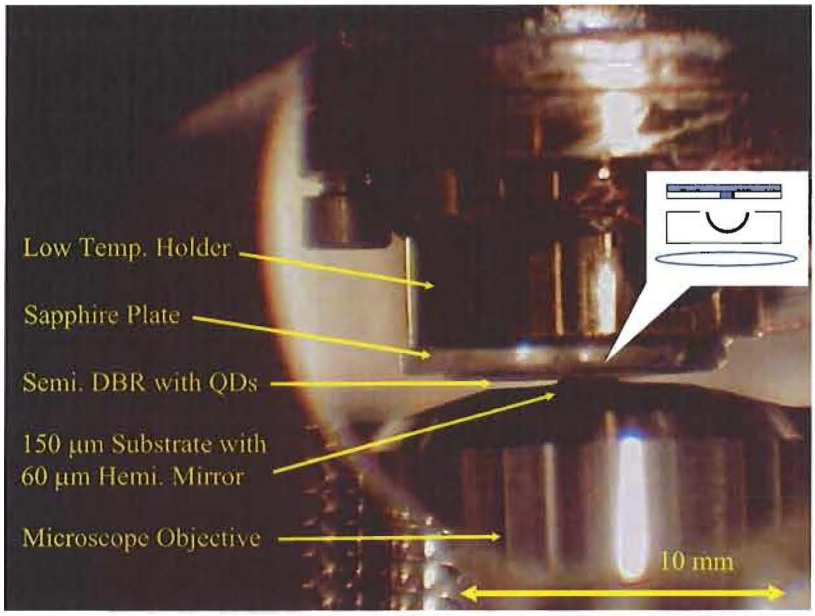

FIGURE 2.2: A hemispherical cavity, comprised of an integrated semiconductor DBR mirror with QDs and a concave dielectric mirror having a radius of curvature 60 μm.

The hemispherical, external-mirror design provides maximum flexibility in spatial and spectral scanning in order to address single QDs, together with a diffraction-limited beam size at the plane of QDs. The method to integrate semiconductor QDs into a cavity has an advantage compared with atomic systems: the QDs are fixed in a solid-state matrix, and do not need to be trapped and held, as do atoms. Moreover, the future practical systems are likely be semiconductor-based, hybrid opto-electronic systems. Our device can be a key ingredient in such a system. Eventually, it may even be possible to integrate photon emission, logic, memory and detection elements into single semiconductor chips to form a photonic integrated circuit for QIP.

The semiconductor DBR mirror is mounted on a tripod system, supported by three Burleigh UHVL Inchworm Motors with a typical mechanical resolution 2 nm, to control precisely its longitudinal position and its angle with respect to the curved mirror. The tripod also contains an x-y nano-scanner, which can laterally scan the mode waist in a $50 \times 50\,\mu\text{m}^2$ region, essential for scanning and addressing single

QDs, and a piezoelectric transducer (PZT) driven by a laser-referenced feedback loop for stabilizing the length of the cavity. Ultra-high-purity copper wires connect the cold finger and the low temperature holder for cooling the DBR mirror to cryogenic temperatures. The thermal insulator between the low temperature holder and the PZT allows cooling down the semiconductor sample to cryogenic temperatures while keeping the PZT at room temperature, preventing from degrading its performance and damaging it. The whole system is shown in Fig. 2.3.

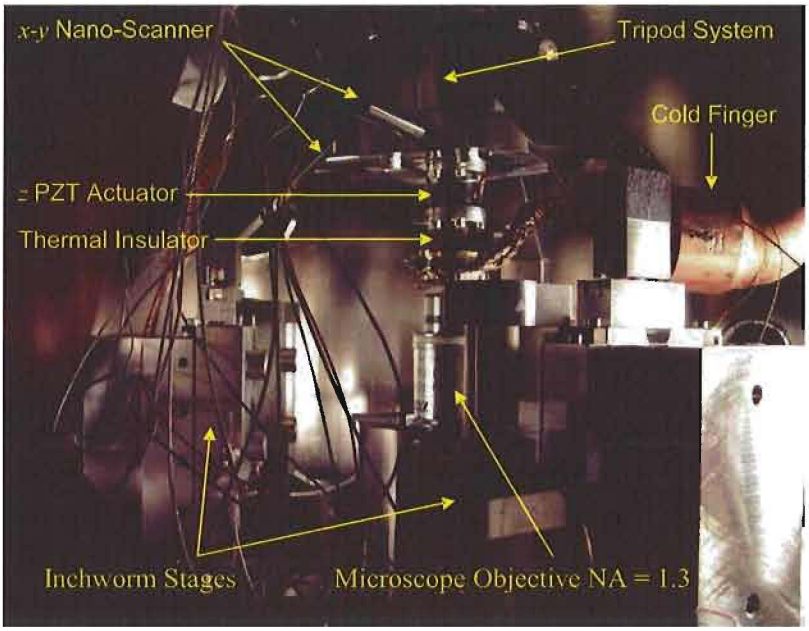

FIGURE 2.3: The cavity assembly: the semiconductor sample is mounted on a five-axis tripod system, sitting on three inchworm stages; curved micro-mirror is glued on top of a high numerical aperture (NA) microscope objective for coupling and focusing an input laser beam properly.

The system operates inside an ultra-high vacuum (UHV) chamber ($10^{-8} - 10^{-9}$ mbar), to allow cooling the DBR mirror to around 10-17 K to reduce QD dephasing rates and to avoid coating of the DBR mirror by cryopumping and attendant absorption and scattering. The UHV chamber, together with the turbo-pump and the ion pump is shown in Fig. 2.4. The turbo pump is used for pre-pumping the

chamber to 10^{-6} mbar. After the turbo pump is shut down, the ion pump starts working and keeps working all the time during the experiment.

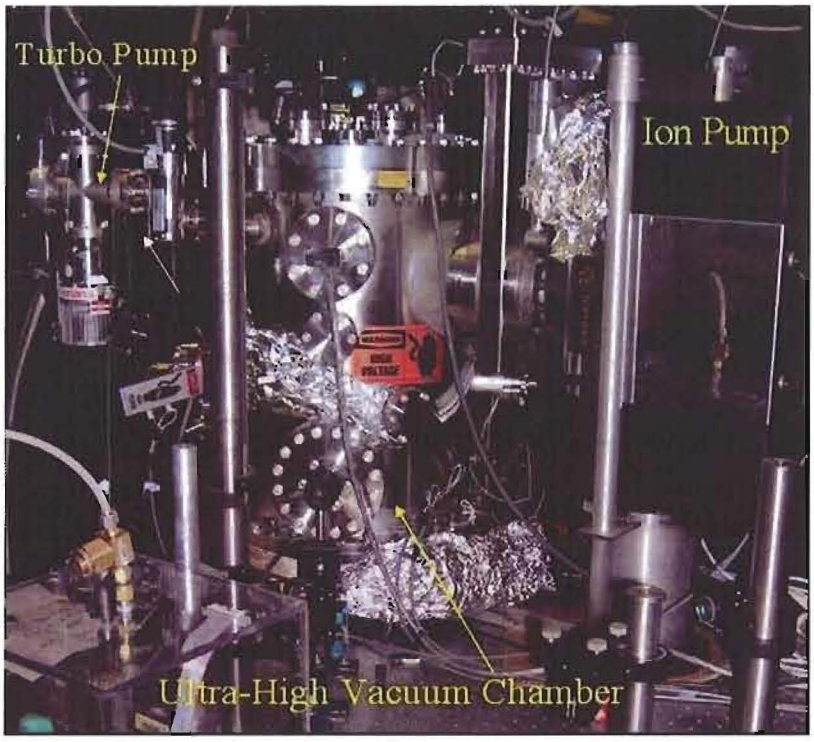

FIGURE 2.4: The ultra-high vacuum chamber with a turbo pump and an ion pump connected.

2.2.1 External Optical Cavity—The Hemispherical Design

As pointed out in Chapter I, there are various geometries of optical resonators. The simplest and most widely used optical resonator is the Fabry-Pérot type, consisting of two curved mirrors facing each other. If the curvatures of these two mirrors correspond to a stable periodic focusing system, and if their transverse dimensions are large enough so that we can neglect edge-diffraction effects, these mirrors thus form an optical resonator which can support a set of lowest-order and higher-order Gaussian modes or beams that will circulate between the two

mirrors. These trapped Hermite-Gauss or Laguerre-Gauss modes form, to a first-order approximation, a set of resonant modes for the two-mirror Gaussian resonator.

In practice, instead of being given a Gaussian beam and asked to fit mirrors to it, we are likely to be asked to find the right Gaussian beam that will just fit properly between two curved mirrors M_1 and M_2 with spacing L, and radii of curvature R_1 and R_2, respectively. See Fig. 2.5. w_0 is the radius of the beam spot at the Gaussian beam waist. w_1 and w_2 are the beam spot radii at two cavity mirrors M_1 and M_2 at positions z_1 and z_2 respectively. We will further discuss how to mode-match a beam into the fundamental spatial mode of a Gaussian resonator in Chapter III.

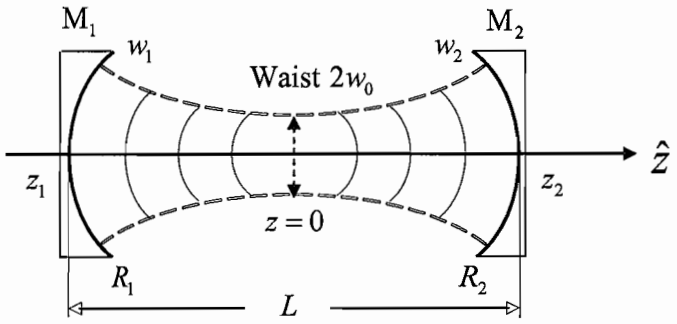

FIGURE 2.5: Model and notation for a stable two-mirror cavity.

Assume that the Gaussian beam has an initially known spot size w_0 and a wavelength λ or Rayleigh range $z_R = \pi {w_0}^2/\lambda$, and the mirrors locate at distances z_1 and z_2 from the location of the beam waist at $z = 0$. Then all the important parameters of this Gaussian beam can be related to the waist spot size w_0 and the ratio z/z_R by the formulas:

$$w(z) = w_0\sqrt{1+\left(\frac{z}{z_R}\right)^2}, \tag{2.10}$$

$$R(z) = z+\frac{z_R^2}{z}, \tag{2.11}$$

$$\phi(z) = \tan^{-1}\left(\frac{z}{z_R}\right), \tag{2.12}$$

where $w(z)$ is the Gaussian spot size at a transverse plane at z, $R(z)$ is the wavefront curvature at plane z and $\phi(z)$ is a phase angle at plane z, or the so-called Gouy phase shift [96]. The essential conditions are then that the wavefront curvature $R(z)$ of the Gaussian beam, as given above, must match the mirror curvature at each mirror, taking into account the specified mirror spacing L. This provides us with three equations, namely,

$$R(z_1) = z_1 + z_R^2/z_1 = -R_1, \tag{2.13}$$

$$R(z_2) = z_2 + z_R^2/z_2 = +R_2, \tag{2.14}$$

$$L = z_2 - z_1. \tag{2.15}$$

The Gaussian wavefront curvature $R(z)$ is usually taken as positive for a diverging beam, or negative for a converging beam, traveling to the right; whereas the mirror curvatures R_1 and R_2 are usually taken as positive numbers for mirror that are concave inward.

The g Factor

Define a pair of resonator g parameters, g_1 and g_2, given by

$$g_1 \equiv 1 - \frac{L}{R_1} \text{ and } g_2 \equiv 1 - \frac{L}{R_2}. \tag{2.16}$$

In terms of these parameters we can rewrite the Rayleigh range the beam spot radius as:

$$z_R^2 = \frac{g_1 g_2 (1 - g_1 g_2)}{(g_1 + g_2 - 2 g_1 g_2)^2} L^2, \tag{2.17}$$

$$w_0^2 = \frac{L\lambda}{\pi} \sqrt{\frac{g_1 g_2 (1 - g_1 g_2)}{(g_1 + g_2 - 2 g_1 g_2)^2}}. \tag{2.18}$$

The locations of the two mirrors relative to the Gaussian beam waist will be given by

$$-z_1 = \frac{g_2 (1 - g_1)}{g_1 + g_2 - 2 g_1 g_2} L, \tag{2.19}$$

$$z_2 = \frac{g_1 (1 - g_2)}{g_1 + g_2 - 2 g_1 g_2} L. \tag{2.20}$$

And the spot size w_1 and w_2 at the ends of the resonator are

$$w_1^2 = \frac{L\lambda}{\pi}\sqrt{\frac{g_2}{g_1(1-g_1g_2)}}, \tag{2.21}$$

$$w_2^2 = \frac{L\lambda}{\pi}\sqrt{\frac{g_1}{g_2(1-g_1g_2)}}. \tag{2.22}$$

Resonator Stability Criterion

It is not difficult to find from the above equations that the real and finite solutions for the Gaussian beam parameters and spot size can exist only if the g_1 and g_2 parameters are confined to a stability range defined by

$$0 \leq g_1g_2 \leq 1. \tag{2.23}$$

This is known as the stability criterion because this is also the condition required for two mirrors with radii R_1, R_2 and spacing L to form a stable periodic focusing system for rays.

A (near) hemispherical optical cavity is an optical resonator bounded by a concave spherical mirror and a planar mirror that is located at the center of curvature of the concave mirror, for which the resonator parameters are $R_1 \equiv R_M = L + \Delta L$ and $R_2 = \infty$, and hence $g_1 = \Delta L/L \approx 0$ and $g_2 = 1$. This resonator has a very small (diffraction-limited) spot size w_2 at the planar mirror end given by

$$w_0^2 = w_2^2 \approx \frac{L\lambda}{\pi}\sqrt{\frac{\Delta L}{L}}, \tag{2.24}$$

$$w_1^2 \approx \frac{L\lambda}{\pi}\sqrt{\frac{L}{\Delta L}} \tag{2.25}$$

for $\Delta L > 0$ and $\Delta L \ll L$.

Justification of Hemispherical Limit—the Order of ΔL

When a collimated Gaussian beam is focused by an ideal lens, the actual focal spot, meaning the position of minimum spot size and maximum energy density, does not in fact occur exactly at the geometric focus of the lens; but rather is located just slightly inside the lens focal length, as shown in Fig. 2.6. The actual waist of the

focused Gaussian beam is at a distance z_f from the position of the ideal thin lens, which is shorter than the focal length f. The radius of curvature of the curved mirror is $R_1 \equiv R_M$. Please note that a hemispherical cavity is indeed a self-focusing imaging system with a focal length $R_M/2$, for a point source at the spherical center of the curved mirror. By definition, a collimated beam passing through a thin lens of focal

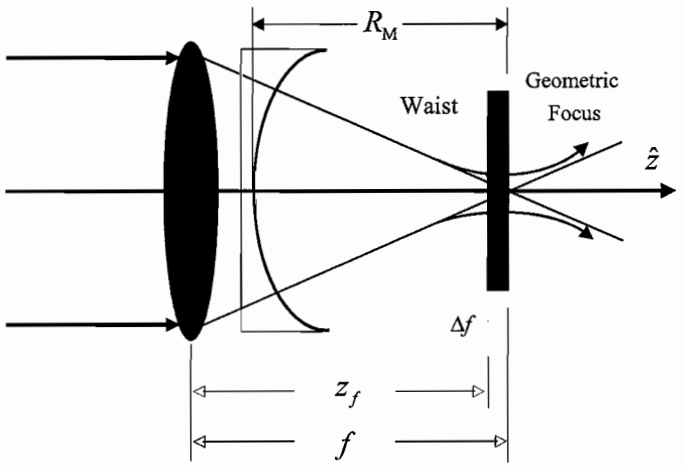

FIGURE 2.6: A collimated Gaussian beam is focused by an ideal thin lens with a focal length f.

length f acquires a wavefront curvature equal to f, therefore

$$R_M(z_f) = z_f + \frac{z_R}{z_f} = f. \tag{2.26}$$

For convenience, here all parameters are used with their absolute value. Subsequently, the difference between the focal length f and the actual distance z_f to the waist is given by

$$\Delta f \equiv f - z_f = \frac{z_R^2}{z_f} \approx \frac{z_R^2}{f}. \tag{2.27}$$

Similarly, for our hemispherical cavity, the derivation of the cavity length from exactly hemispherical is

$$\Delta L = R_M - L = \frac{z_R^2}{L} \approx \frac{z_R}{R_M} z_R. \tag{2.28}$$

Let us make an estimate of the order of the ΔL for our micro-cavity. Assuming the beam waist w_0 at the planar mirror is about the size of the incident laser wavelength λ, then the Rayleigh range $z_R \equiv \pi w_0^2/\lambda \approx \pi\lambda$. Therefor $\Delta L \approx \pi^2\lambda^2/L$. Given a nominal wavelength $\lambda = 765$ nm for a probe laser and a cavity length $L = 60$ μm, we have $\Delta L \approx 96$ nm, which is much larger than the Burleigh UHVL Inchworm Motors' mechanical resolution 2 nm, and we are able to control the cavity length finely enough to reach and probe the hemispherical limit.

The great advantage of the hemispherical design is that the mode alignment difficulties in this design are largely if not completely eliminated. In addition, the use of a hemispherical micro-cavity offers the following advantages:

1. The hemispherical cavity is geometrically stable, in terms of laser cavity stability;

2. The hemispherical mode has a waist size w_0 at the planar DBR mirror that is diffraction limited and consequently leads to a large coupling constant g_0;

3. Our system uses a cavity with adjustable length and a transversely movable focal region, allowing good spatial and spectral overlap of QD resonances with high-Q cavity modes.

4. It enables direct out-coupling of the spontaneously emitted photons into a single-mode traveling wave along the cavity axis;

5. The fundamental modes of the cavity (Gaussian modes) can be efficiently coupled into lens, fiber and other optical components.

Please note that the QD-cavity mode coupling strength is proportional to the amplitude of the normalized cavity mode at the location of the QDs. In order to make the coupling strong, it is necessary to localize highly the transverse extent of the mode function in the vicinity of the QDs, and align the mode polarization vector with the dipole transition matrix elements of the QDs. Determining the precise degree

to which this localization is possible is nontrivial, since the mode structure for such a small cavity is non-paraxial, is non-separable into polarization components, and is non-separable into longitudinal and transverse functions [97, 98].

2.2.2 GaAs Semiconductor Quantum Dots

The optical center used in this research is semiconductor QDs. In this section, we introduce the central physical concepts and results of semiconductor QDs. Rather than provide an exhaustive review, we only highlight important concepts in an introductory manner with experimental or theoretical results that serve our purposes. The QDs used in our experiment are the natural QDs formed by fluctuations in the well width in a thin (3-6 nm) GaAs QW, arising in part from monolayer-high interface islands. However, most of the concepts and results are common to all semiconductor QDs. We will first give a brief introduction of the natural interface fluctuation QDs and the technology to fabricate them. Then we will discuss how to model the energy structures and spectra of the excitons and biexcitons in this type of QDs.

QDs are particles of semiconductor crystals (nano-structures), often embedded in a barrier material, with dimensions that are small enough (10-100 nm) such that quantum confinement of electrons plays a central role in their physics. Their discrete energy spectra and relatively wide energy level spacings minimize many of the relaxation processes that dominate in bulk or two-dimensional samples, resulting in homogeneous linewidths that are generally narrower in QDs. Optical oscillator strengths are also relatively large, and in combination with narrowband lasers or a single mode of a very high finesse micro-cavity tuned to the discrete optical transitions of QDs, strong interaction between light and matter can be achieved in composite QD-cavity systems.

One dominant technology for the production of QDs is epitaxy. The epitaxial growth of QDs is dominated by molecular beam epitaxy (MBE). MBE-grown QDs are mostly from III-V group materials, such as GaAs, InGaAs, InAs and InP, and

occasionally from other groups, such as PbSe and CdSe. The MBE technique allows one to control thickness within one or two monolayers in the growth direction (z). Nearly perfect heterojunctions produced this way give good passivation and therefore most MBE-grown nano-structures are free from surface states. These heterojunctions provide quantum confinement along the growth direction. In the plane (x-y) of the epilayer, quantum confinement is produced either by naturally formed interface fluctuations [99, 100, 101], self-organization [102, 103, 104] or via patterning and lithography [80, 105, 106]. Another dominant technology for the production of QDs is chemical synthesis. Chemically synthesized QDs are also known as semiconductor nanocrystals [107]. Typically, II-VI materials, such as CdSe, CdS, CoO and ZnS, form the QD core and are passivated to form a core-shell structure [108, 109, 110].

The GaAs QDs that we use are naturally formed by interface fluctuations. During MBE-growth of a QW, large monolayer-high islands can be developed at the well-barrier interface during interrupts of a minute or more under an arsenic flux. Much of this roughness persists at an interface as subsequent layers are grown. During growth interrupts, the islands can grow to lateral size about 50-100 nm across, larger than the Bohr diameter of the exciton (bound electron-hole pair), and an order of magnitude larger than the well width (3-6 nm), leading to elliptical disk-like shapes. These types of natural QDs are often referred to as "interface fluctuation quantum dots (IFQDs)" [111, 101, 112]. Figure 2.7 shows the top surface of a GaAs QW imaged with scanning tunneling microscopy (STM). As seen in the figure, the structures tend to elongate along the $[\bar{1}10]$ crystal axis,

Semiconductor DBR mirrors with exceptionally good surface smoothness can be grown by MBE techniques. The high-reflectivity DBR mirror that we use are also grown by MBE. The MBE growth for this study is performed by our collaborators H. Gibbs and G. Khitrova at the University of Arizona (UA). They found that the surface roughness on transverse length scales relevant for our needs ($\sim$ 1 μm) is equal to that of the very best polished super dielectric mirrors of the type used in

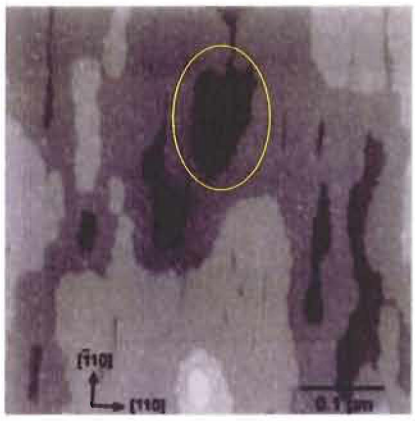

FIGURE 2.7: STM image of a GaAs QW surface showing the large monolayer-high islands. The circled region is referred to as an IFQD, Ref. [110].

atomic cavity-QED experiments [5]. The relevant length scale is about one micron because our cavity design yields a waist size at the DBR mirror of this size. The UA group has succeeded in growing good-quality IFQDs embedded in the middle of a one-wavelength spacer layer on the top surface of high-quality DBRs. Due to the 3D quantum confinement, QDs have atom-like energy-level spectra. The modeling of QDs is relatively simple compared to higher-dimensional systems despite many variables, such as the shapes and the sizes of the QDs. However, we need to introduce the concepts of exciton and biexciton first in order to further model the energy spectra of QDs.

In bulk semiconductors, due to the Coulomb interaction between optically excited electrons and holes, the excitonic effects dominate the optical response below the bandedge. Under the effective mass approximation, an exciton can be regarded as a well-defined single quasi-particle containing an electron and a hole [113, 114]. Its envelope function can be separated into the center-of-mass motion (plane wave in bulk semiconductors) and the relative motion between the electron and the hole. The equation that determines the electron-hole relative motion is called the Wannier equation which has a solution that resembles the electron-ion relative motion in a

hydrogen atom. The Bohr diameter of the exciton, determined by material parameters such as the effective mass of the electron and the hole, must be significantly larger than the lattice constant for the effective mass approximation to hold. This is indeed the case for most materials. For example, GaAs has a Bohr diameter of about 25 nm, compared to the lattice constant of 0.56 nm. This type of exciton is known as Wannier exciton. In the other case that the Bohr diameter of the exciton is comparable to or smaller than the lattice constant, this type of exciton is called Frenkel exciton [115].

In semiconductor QDs, an interacting electron-hole pair is subject to 3D quantum confinement, which generally results from a bandedge offset between the dot material and the surrounding matrix which is usually a semiconductor of higher bandgap. In QDs with weak lateral confinement, such as the natural GaAs IFQDs used in our experiment, the exciton binding energy is larger than the confinement energy, and it is the center-of-mass wavefunction of the exciton that is localized. Localization changes the energy spectrum of the exciton from a continuum into a set of discrete levels, which are referred to as QD exciton states, as shown in Fig. 2.8. The QD energy continuum, for instance can be free electron-hole pairs in the 2D QW.

Excitons in an IFQD are confined in three dimensions by an imperfect GaAs QW. Vertical confinement (in the epitaxial growth direction) is provided by the QW barriers ($Al_xGa_{1-x}As$), while lateral confinement in the QW plane results from natural variations in the effective thickness of the GaAs QW as shown in Fig. 2.9(a). This confinement results from the level mismatch between QW subbands in regions of the well with different thickness. The potential barrier formed by the monolayer-high steps (a few meV), as shown in Fig. 2.9(b), is an order of magnitude less than that for the $Al_xGa_{1-x}As$ potential barrier in the vertical direction (a few hundred meV). Therefore the QD, though providing strong confinement in the vertical direction, is weak in the lateral directions.

The above analysis assumes that only the Coulomb attraction within each particular electron-hole pair state needs to be considered. These discrete states are the

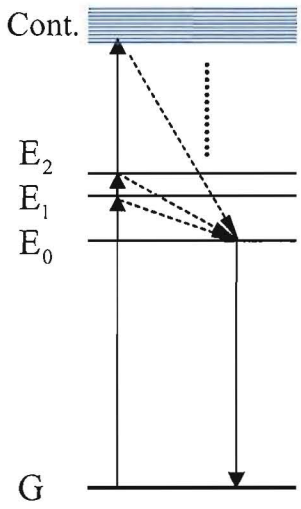

FIGURE 2.8: Schematic diagram of energy levels of a QD. G stands for the ground state of the crystal, or exciton vacuum. E_0, E_1 and E_2 are the ground state, the first two (possible) excited states of the QD. Cont. denotes the QD energy continuum.

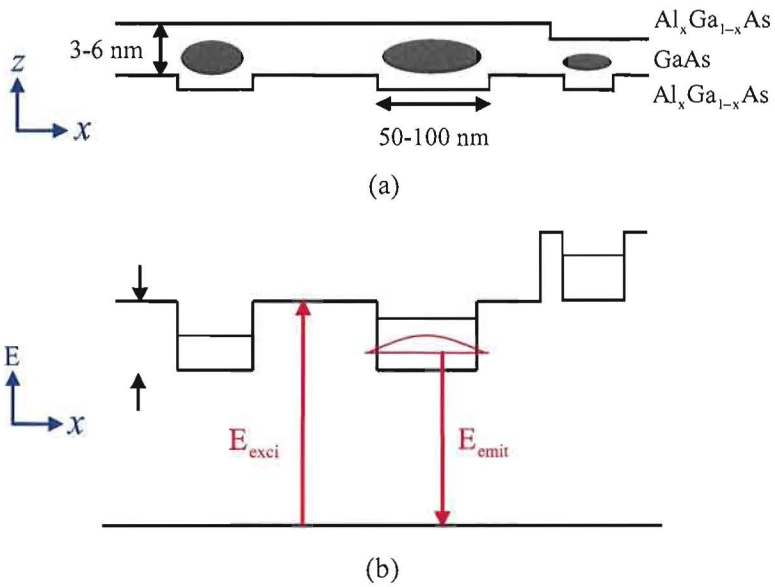

FIGURE 2.9: Schematic diagram of a 3-6 nm QW with large monolayer-high islands at the interface that lead to confinement of the exciton (a), and the corresponding lateral confinement potentials associated with the interface islands (b).

eigenstates of the system where only one electron-hole pair is created. In the case that two electron-hole pairs are excited, the Coulomb interaction between the two electron-hole pairs needs to be considered. Therefore the energy of the two-exciton state does not equal to sum of the two exciton states. The difference reflects the interaction energy between the two excitons. In the perturbation theory, it appears as a higher-order correction and is therefore referred to as a higher-order Coulomb correlation [116]. Its sign and strength are determined by factors such as the electron/hole effective mass ratio, the quantum confinement and the spins of the electrons and holes. The stable binding of the exciton-exciton molecule (with negative binding energy) is referred to as a biexciton. Despite the weak confinement in the lateral directions in IFQDs, evidence for complete localization of excitons and biexcitons has been found using different approaches, including the quantification of the confinement energy, the direct microscopy image of excitons via emission and resonant coherent nonlinear response of excitons. Evidence for localized complex states containing more than two excitons are not observed, possibly due to the limited confinement [117].

As a useful approximation, the energy spectrum of a QD can be separated into energies associated with the vertical and lateral directions. The strong confinement along the z-axis governs many of the properties of the exciton, such as the electron g-factor and exchange Coulomb energies. Here the electron g-factor is a dimensionless quantity which characterizes the magnetic moments of an electron. (Please do no confuse this electron g-factor with the cavity g factor defined in Eq. (2.16) in Sec. 2.2.1.) The low-energy excited states are determined primarily by the lateral size and shape of the QD and have energy splitting on the order of a few meV. Because the light-hole exciton is shifted by tens of meV, the spectra and other properties of these low energy QD states are derived primarily from the lowest energy heavy-hole subband of the QW, and light-hole mixing is weak. The level diagrams that include the crystal ground state (exciton vacuum), the two lowest orthogonal heavy-hole

bright exciton states and the bound biexciton state of relevance to optical studies are shown in Fig. 2.10 below.

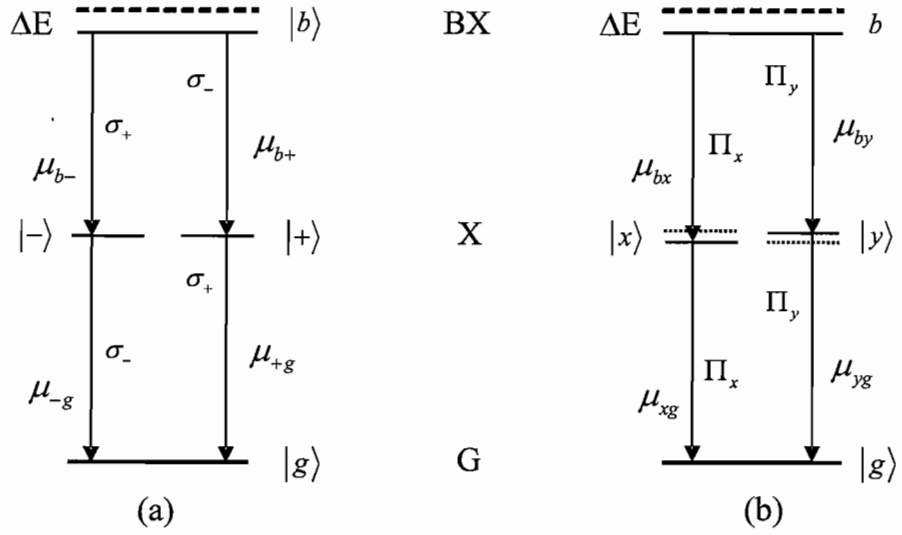

FIGURE 2.10: Model for a GaAs QD. G, X and BX denote the ground, the exciton and the biexciton states respectively. ΔE is the biexciton binding energy. The optical selection rules for transitions in a symmetric and an asymmetric QD are shown in (a) and (b), respectively.

$\Pi_y(\Pi_x)$ is the linear polarization perpendicular (parallel) to the QD elongation (crystal $[\bar{1}10]$ axis or $-\hat{x}$ direction) in the plane of the GaAs layer. Without the magnetic field, the two exciton states are excited using the linearly polarized light and are labeled as $|x\rangle$ and $|y\rangle$. An externally applied magnetic field can diminish the mixing within the heavy hole states [118, 119]. The transitions become circularly polarized. The exciton states are represented by $|+\rangle$ and $|-\rangle$. The dipole moment of various transitions are denoted by μ_{ij}, where i and j are indices representing the final states (b and $-,+$ or x,y) and initial states ($-,+$ or x,y and g) of the dipole transition, respectively.

In the ideal situation, the optical transitions for excitons in QDs of zinc-blend semiconductors such as GaAs are circularly polarized, as indicated by the solid arrows

in Fig. 2.10(a). The right-hand circularly polarized (σ_+) transition leading to the $|+\rangle$ exciton state is between spin-up state of the s-like conduction bandedge with magnetic quantum number $m_j = +1/2$ and the heavy-hole bandedge state with magnetic quantum number $m_j = +3/2$. The left-hand circularly polarized (σ_-) transition leading to the $|-\rangle$ exciton state, however, is between the $m_j = -1/2$ conduction bandedge state and the $m_j = -3/2$ heavy-hole bandedge state.

For the GaAs interface fluctuation QDs under study, however, they are elongated along the crystal $[\bar{1}10]$ axis due to the dynamics in the growth, leading to band mixing and modified optical selection rules due to the long range part of the exchange interaction [114, 120, 119]. It is found that the two excitonic states become mixed and slightly split (a few tens of μeV) and the optical transitions become linearly polarized [111, 121, 119]. This is shown in Fig. 2.10(b). In an ideal and symmetric QD, the cascade exciton emission will produce polarization-entangled photon pairs [122]. The splitting, however, provides 'which-path' information, preventing polarization entanglement of the intermediate exciton emissions. So if the 'which-path' information caused by the frequency splitting can be erased, one would again be able to produce polarization-entangled photon pairs. An externally applied magnetic field can be used to tune the splitting to zero, and polarization-entangled photon pairs have been generated in this way [123]. We will discuss how to use radiative decay cascade of a biexciton in an IFQD based on our system to produce polarization-entangled photon pairs in Chapter VI.

2.3 Distributed Bragg Reflectors

The highly reflective semiconductor planar mirror that we use in our cavity is a distributed Bragg reflector (DBR) mirror with semiconductor QDs embedded in the middle of a one-wavelength spacer layer on top of it. In this section, we give a brief background of a DBR mirror and how to integrate optical centers with it.

There are two well known geometries that utilize interference effects to produce high reflectivity mirrors: one is the quarter wavelength (QWL) stack, typically called a distributed Bragg reflector; the other is the Bragg crystal [124, 125, 126, 127]. The QWL stack gives the fastest increase in reflectivity with increasing number of layers, but deteriorates fast in the performance if one of the layers is absorbing. The Bragg crystal minimizes absorption by positioning the absorbing layers into the nodes of the standing wave produced by the superposition of the incident and reflected waves. A Bragg mirror designed in both ways present a wavelength interval centered at a target wavelength in which the reflection coefficient at normal incidence can be very close to one. In addition, the phase of the reflection coefficient within this region of high reflectivity, called "stop-band", behaves linearly as a function of the frequency.

The QWL stack consists of alternating layers of high (H) and low (L) refractive indices, each of the same optical thickness of a quarter of the target wavelength for normal incidence, such that all boundaries add with equal phase to the reflected wave. For the case that both layer materials are completely absorption free, the QWL stack gives the highest reflectivity with the fewest number of layers and approach a reflectivity very close to one. In a QWL stack, each layer extends from a node to an antinode; if one or both layers are only slightly absorbing the performance of the QWL stack deteriorates fast due to the large absorption losses at the antinodes of the standing wave.

The Bragg crystal consists of unit cells with half wavelength (HWL) optical thickness for normal incidence, which contribute in phase to the reflected wave. An unit cell typically has two constituent layer materials (binary design) with one, usually absorbing, much thinner than the other less absorbing or absorbing free one to suppress the absorption. Each inner layer of an unit cell, however, will not necessarily add up in phase with reflected wave, leading to a narrower stop-band.

For certain demanding applications, unit cell may consist of three materials (ternary design) to compensate the phase differences between the incident and

reflected waves and to locate the most absorbing layers to the nodes of the standing wave fields. This is made plausible due to the fact that the field intensity increases quadratically with distance from the node. This leads to an absorption that decreases as the third power of the thickness for a very thin film [124]. The reflectivity of a very thin film decreases only quadratically with thickness. Therefore, the absorption losses can be greatly reduced compared to the reflectivity if thinner absorbing layers are used. So we can reduce the absorption and optimize the figure of merit using a Bragg crystal, either a binary or a ternary design, to locate the absorbing layers at the nodes of the standing wave field. For the highest possible reflectivity, materials should be selected by the following rules:

1. Select a first material with the lowest possible absorption constant as a spacer material.

2. Find a second material with the largest possible reflection coefficient at the boundary with material one.

3. If several materials give similar reflection coefficients, choose the one with the smaller absorption coefficient.

4. Make sure that the material can be deposited with sharp, smooth boundary in order to eliminate scattering.

Optical centers can be grown in the middle of a spacer, either half-wavelength thick or one-wavelength thick, to locate the optical centers at an antinode of the cavity field. The spacer is on top of a good optical quality DBR mirror, which can be tailored to have a high reflectivity while still maintaining a transmission much larger than the absorption and scattering, at the same time. Such an integrated structure will look like in Fig. 2.11.

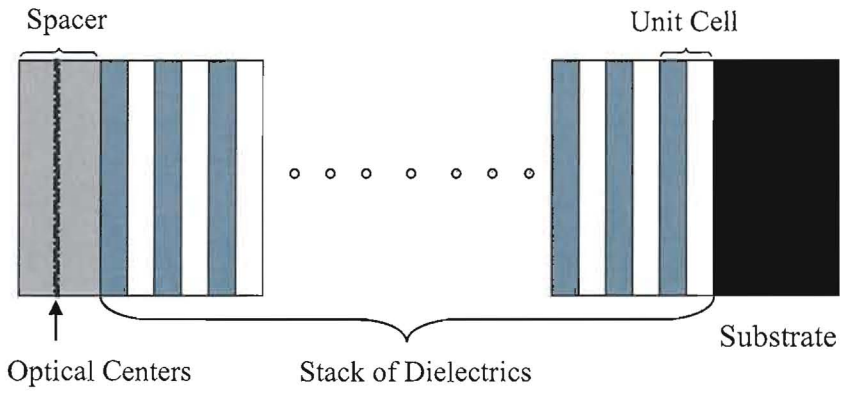

FIGURE 2.11: Schematic structural design of an integrated DBR mirror with active optical centers in the middle of a spacer layer.

2.4 Summary

To summarize, in this chapter, we first gave an overview of concepts using an optical micro-cavity interacting strongly with a single optical center for efficient production of single photons in Sec. 2.1. We developed a method and gave a description of a physical system we designed and constructed that is necessary for fulfilling our purpose. Two different light-matter coupling regimes (strong- and weak-coupling regimes) are considered. Sec. 2.2.1 presents the detailed physical system we constructed. In the last section Sec. 2.3, we gave a brief introduction of how to design a DBR mirror and how to integrate optical centers with it. Armed with concepts introduced in this chapter, we will show how we design, construct and characterize the micro-cavity. Then in the later chapters we will examine this system to see if we can reach our goal.

CHAPTER III

OPTICAL MICRO-CAVITY WITH SEMICONDUCTOR QDS

We have given an overview of the system in Chapter II. In this chapter, we describe the details of design and construction of the whole system, specifically on the state-of-the-art fabrication of a hemispherical micro-cavity that is comprised of a planar semiconductor DBR mirror integrated with QDs, and an external, concave dielectric micro-mirror. Then we discuss the characterization of the micro-cavity system. We model match an input laser beam to the fundamental mode of the micro-cavity in order to excite the mode efficiently so that it interacts with a QD strongly, by adjusting the laser beam's waist size and position. The micro-cavity system operates inside an ultra-high vacuum chamber, to allow cooling the sample to around 10-17 K and to avoid coating of the samples by cryopumping. We tested the cavity transmission spectra at both room temperature and cryogenic temperatures and obtained preliminary spectroscopic results showing evidence of significant cavity-QDs interaction at 17 K. Part of this chapter has been published in Ref. [6].

3.1 Introduction

As pointed out in the previous two chapters, optical micro-cavities have played a central role in achieving strong coupling between a single atom and a mode of an optical cavity, which enables a range of novel phenomena that rely on the control of the mode structure of the vacuum (so-called cavity-QED effects). These include enhanced or suppressed spontaneous emission [87, 128, 129, 130, 131, 132], thresholdless lasing [133, 134], normal-mode splitting [5], and optical nonlinearity at the single-photon

level [135, 136, 94]. In the last two decades, such strong coupling has been achieved in free-space atomic systems, such as a dilute atomic beam passing through a short (10-100 μm length) optical cavity [137, 138, 139], or through a cold microwave cavity [140].

There is also interest in achieving strong cavity-QED coupling in semiconductor systems. The research on semiconductor or excitonic cavity QED started in the late 1980s. The early experiments belong to the weak-coupling regime, for which the spontaneous emission process is still an irreversible process. However, a modified spontaneous emission rate and altered radiation pattern have been demonstrated. It is expected that the quantum efficiency, response time and intensity noise of a single semiconductor light source can be improved by cavity-QED effects. The research on semiconductor cavity QED entered into the strong-coupling regime in the early 1990s with the pioneering experimental work of Claude Weisbuch and coworkers [141, 126], where many excitons in the QW interact collectively with the optical cavity. The QW excitons and the cavity exchange energy coherently, and thus spontaneous emission becomes partially reversible. This rapidly growing field has produced numerous interesting results in the fundamental sciences in the past decade. However, the practical applications of semiconductor cavity QED in the strong-coupling regime have yet to be identified. Semiconductor cavity-QED strong coupling in this context means that a single photon in the cavity can saturate one exciton, and conversely a single exciton can strongly influence the optical field in the cavity, which is different from those early researches mentioned above.

Following early studies using planar QW-cavity systems, which themselves cannot reach this regime [30], recent experiments showed signatures of strong coupling in some monolithic structures such as micro-pillar [44], photonic crystal nano-cavity [45] and micro-disk [47, 48]. Obvious advantages of using QDs in such schemes are that the QDs are stationary and they exist in a solid-state system, which can be optically or electrically pumped [39]. The principal disadvantages in these monolithic

structures, however, are the lack of efficient control of the spatial and spectral overlap between QDs resonance and cavity modes. For instance, temperature tuning of the QD has to be used to tune through cavity resonance, which is undesirable because the dipole dephasing rate increases at elevated temperatures [49, 50].

So we want to use a more flexible system to study this problem. This dissertation, particularly this chapter, focuses on the design, fabrication, modeling and performance of an external, hemispherical micro-cavity for semiconductor cavity QED. The cavity parameters are in a novel range: cavity length = 40-60 μm, finesse = 260 (which should be amenable to increase by an order of magnitude), mode-waist size $\approx 1\,\mu$m, mode divergence angle ± 40 deg. This cavity design contains two unique features—the use of a concave micro-mirror with high-reflectivity over a large-solid angle and the use of an integrated DBR mirror containing the QD sample in an external-cavity configuration. The 40–60-micron curved mirror substrate has a high degree of sphericity and an excellent surface quality, enabling the application of a custom-designed multilayer dielectric coating with 99.5% reflectivity over a high-solid angle [142]. Such large solid angle is unique compared with, for example, a recently reported half-monolithic micro-cavity design for atomic cavity QED [143].

One potential application of such a cavity-QD system is for semiconductor cavity-QED studies; the other is for on-demand generation of single photons or polarization-entangled pair photons. The cavity can also be operated with a standard planar dielectric mirror replacing the semiconductor DBR mirror. Such an all-dielectric cavity may find uses in atomic cavity QED or cold-atom studies [53, 54], or in novel forms of microscopy or interferometry. The cavity components have been fabricated in our collective laboratories—the concave micro-mirror by a novel gas-bubble inside glass technique here at the University of Oregon and the DBR/QD structure by MBE at the University of Arizona.

3.2 Cavity Design Overview

Figure 3.1 shows a real structure and a schematic diagram of the cavity. A transparent, planar substrate with a multilayer DBR coating (made either of semiconductors or optical coating dielectrics) forms one end of the cavity. A transparent concave glass surface with a dielectric multilayer reflective coating forms the other end. In between is air or vacuum. The radius of curvature of the mirror is denoted R_{M}, and can be fabricated in the range 40-100 μm. d is the depth of the dimple, which typically is around one half of the radius of curvature of the dimple. The on-axis distance L between the surfaces of the two mirrors is referred to as the cavity length. In a hemispherical cavity these lengths are equal, $L = R_{\mathrm{M}}$. This places the cavity on the boundary for stability, and (in the paraxial approximation, which actually fails here) leads to the interesting property that the modes fall into groups with a high degree of frequency degeneracy [96]. The radius of the mode waist,

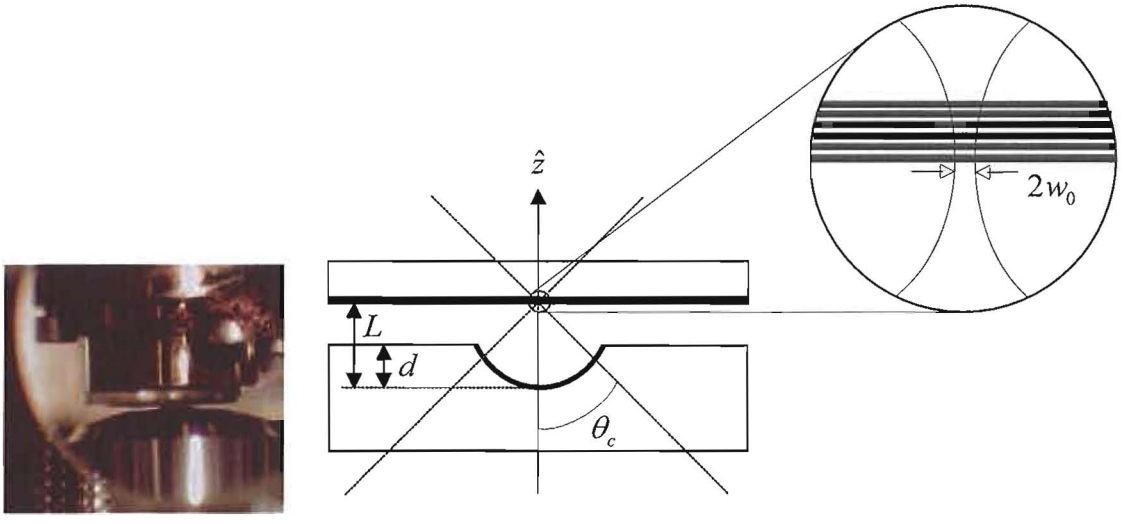

FIGURE 3.1: Hemispherical cavity, comprised of a planar substrate and a concave glass surface with layer reflective coating (shown as grey region). The dashed lines approximate the 1/e intensity contours of the fundamental mode in the cavity and its continuation outside. The blow-up shows the DBR and the mode contours in the waist region.

located at the planar mirror, is denoted w_0. Since the QD is to be placed in this waist, this radius should be minimized in order to maximize the coupling between the QD and the field. The angular half-width of the cavity mode is θ_c. Diffraction dictates that the smaller w_0 is made, the larger θ_c becomes. When w_0 equals one optical wavelength, the angle θ_c is roughly 40 deg. For such large angles, the electromagnetic field cannot be completely transverse to the cavity axis, as would be the case in the paraxial limit where θ_c is restricted to very small values. This indicates a need for a theory, summarized below, beyond the common paraxial treatment.

3.2.1 Concave Micro-mirror Substrates

A unique component of our cavity is the concave micro-mirror. We developed a technique for its in-house fabrication. For use in a high-finesse cavity, it is crucial that the curved surface of the mirror substrate be smooth on nanometer scales. This prevents undue amounts of light scattering that would act as a loss, spoiling the finesse.

Our technique, shown in Fig. 3.2(a), proceeds by melting a stack of small, high-quality borosilicate glass tubes under a nitrogen atmosphere, trapping small gas bubbles. By surface tension the gas bubbles are naturally created with a high degree of sphericity. After the glass cools and hardens, we grind and polish it on a simple optical polishing wheel so that about one-third of a selected bubble remains embedded in the surface. The top surface, where a few bubbles are open, is finished with diamond discs featuring nickel-plated diamonds in a raised dot matrix pattern of 6 μm grit size on a polishing wheel. The bottom surface is polished using a 0.05 μm colloidal silica suspension on a polishing cloth, to achieve an optical-quality finish. Finally, we obtain a flat sample of about 150 μm thickness, which forms our concave mirror substrate. For details of the optical properties of the glass we use and the fabrication procedure, please refer to Appendix A.

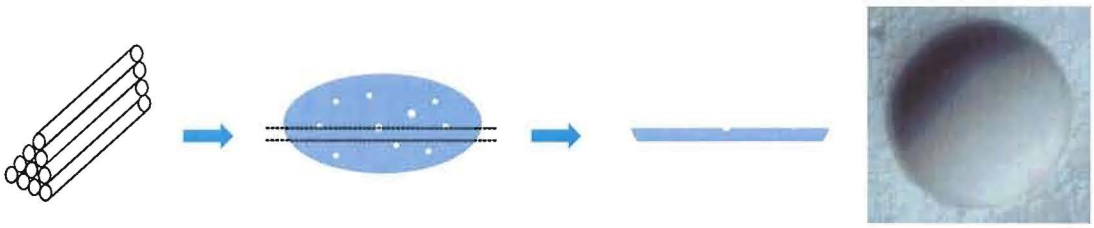

(a) (b)

FIGURE 3.2: (a) Melting borosilicate glass tubes to form nitrogen gas-bubbles in the glass and polishing the glass bulk into a 150 μm-thick slide. (b) 40× pictures of a dimple. Diameter of the dimple = 100 μm.

Figure 3.2(b) shows an image of a typical dimple at 40× magnification. The planar surface on the top side, surrounding the dimples, is very rough, as a result of the final 6 μm-grit used on this side. This was chosen to minimize the amount of contaminating sub-micron glass dust produced during polishing. The inside of the dimple (out of focus here) is far smoother. The dimples will ideally have an opening half-angle of $\theta_c \approx 40$ deg, a radius of curvature of $R_M \approx 60\,\mu$m and a surface with sub-nm roughness.

We expected a good sphericity of the dimple surfaces since for decreasing dimensions the surface tension is an increasingly strong force compared to other forces like gravity. The sphericity has been measured at UA with a Wyko interferometer [144]. Figure 3.3 shows a typical surface scan of the dimples. At the bottom of a dimple, in a circle of 15 μm diameter, the deviations from perfect sphericity where found to be less than 10 nm.

The surface roughness was also measured using a Wyko interferometer that carries out a Fourier-analysis of the surface to determine the power (spatial) spectral density (PSD) of surface roughness as a function of the lateral size of the errors. Figure 3.4 shows the measured PSD of five dimples and that of a commercially polished super dielectric mirror, provided by the Kimble group at Caltech. For errors with a transverse spatial frequency greater than 50 mm^{-1} and up to 500 mm^{-1}, the surface

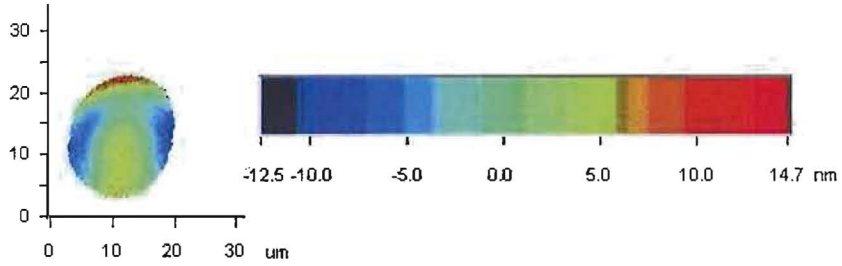

FIGURE 3.3: Measured sphericity at the bottom of a dimple with a Wyko interferometer at the University of Arizona.

quality competes with the best polished super dielectric mirror. Assuming the trend in the data goes on, for length scales smaller than one micron, our dimples should be much smoother than the super dielectric mirror. However the roughness increases dramatically for smaller spatial frequencies (larger length scales). We are not sure whether this represents intrinsic errors like wrinkles formed in the cooling process or debris left from polishing.

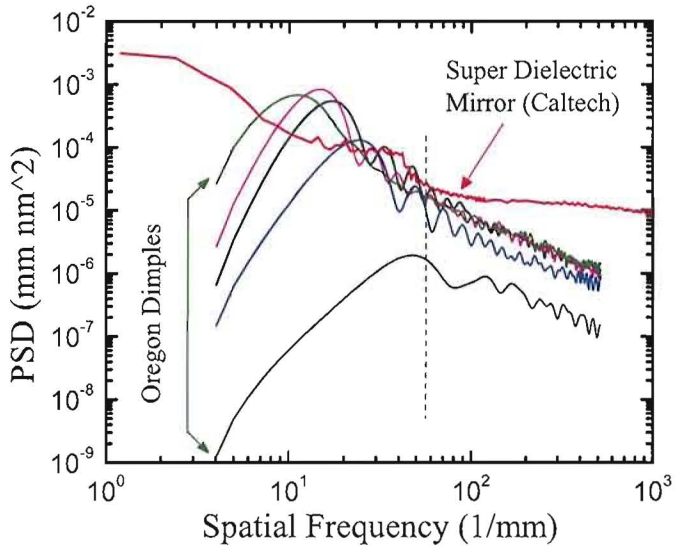

FIGURE 3.4: Measured surface roughness of five dimples fabricated at the University of Oregon and the super dielectric mirror used at Caltech with a Wyko interferometer at the University of Arizona.

3.2.2 Optical Coating for a Curved Micro-mirror

Optical coating of such a small and highly curved dimple substrate is a nonstandard procedure and is challenging. One problem is that the atomic coating beam is incident on the curved surface at a different angle at each different location. This alters the deposition rate in a location-dependent manner, which leads to systematic variation of the layer thickness and therefore of the edge wavelengths of the coating's stop-band. Therefore, we designed a coating scheme (using TFCalc), in a way that compensates for the large change of coating-beam angle across the surface of the substrate.

Our goal is a coating with high reflectivity over a large area of the dimple, with a center wavelength at 765 nm. First, we choose a high-index-contrast TiO_2/SiO_2 coating in order to minimize the required number of coating layers for a given target reflectivity; second, we have a stop-band shifted to longer wavelength (775 nm) at the center of the dimple in order to further compensate for the layer thickness variation towards the edge. Figure 3.5(a) shows a coating design with 6.5 pairs of TiO2/SiO2 quarter-wavelength stack, giving a peak reflectivity 99.61% at the reference wavelength 775 nm. The refractive indices used for the plot are 2.32 and 1.44 for TiO_2 and SiO_2 respectively, at 775 nm, also assuming no absorption for both materials in the plotting wavelength range. For the working wavelength 765 nm, the reflectivity at the dimple center is greater than 99.5% between 738 nm and 813 nm as shown in Fig. 3.5(b).

For locations away from the center, the coating layers become thinner, shifting the stop-band to shorter wavelengths. At some location on the dimple surface (or angle from the optical axis at the mode focus region), the stop-band edge suddenly shifts past the working wavelength, causing a sudden drop of mirror reflectivity, as has also been observed in [143]. The concave-mirror substrate was coated by Spectrum Thin Films [142] using a standard commercial technology, pulsed ion beam technology, which allows coating fragile optics at near room temperature and gives less stress.

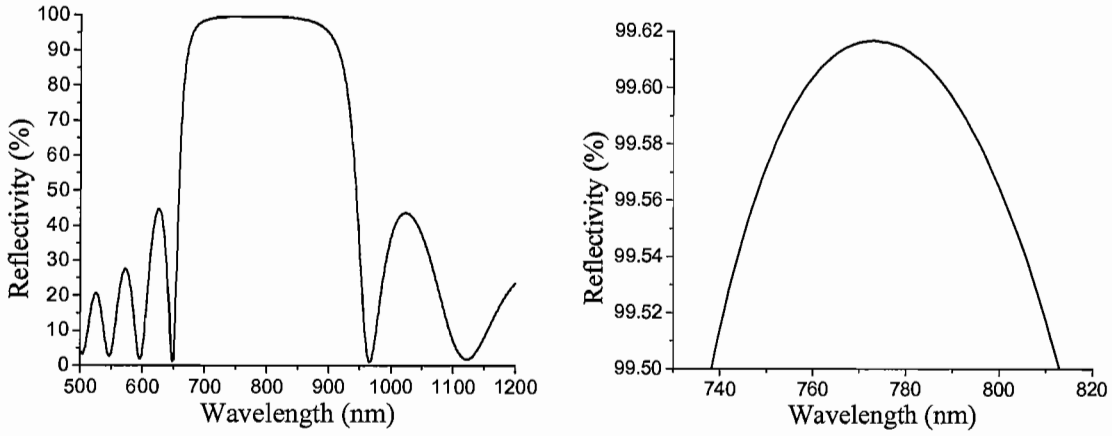

(a) (b)

FIGURE 3.5: (a) TFCalc design of a multilayer dielectric coating for the dimples. (b) Wavelength region where the reflectivity is greater than 99.5%.

Our measurements, shown in Fig. 3.6, of the dimple-mirror transmission versus angle from the optical axis confirms that our design and fabrication has succeeded in giving a high reflectivity (99.5% or higher) over a wide angular range of ±40 deg, which is wide enough to support the hemispherical modes of interest.

The coated curved dimple was then glued, using index-matched, UHV-compatible, ultra-violet (UV) cured optical adhesive (Norland Optical Adhesive 88), to the face of a 100× immersion-microscope objective (Zeiss Plan-NEOFLUAR) with a numerical aperture NA=1.3, in order for efficient mode-coupling over a high-solid angle and proper focusing to get a diffraction-limited beam spot at the focus. To ensure proper positioning of the dimple, we glue it while monitoring interferometrically by a Twyman-Green interferometer [145], in which a laser beam passes into the objective, reflects from the dimple surface and interferes with a reference beam. Figure 3.7(a) shows a set-up used in our experiment, which was initially built by Ruediger Loeckenhoff [146].

A reference laser beam coming from an optical fiber out-coupler, after expanded in size, is directed into a 50/50 cube beam splitter. One branch propagates straight

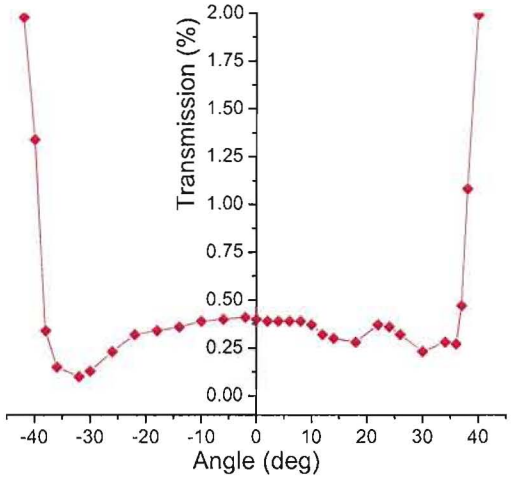

FIGURE 3.6: Measured dimple-mirror transmission versus angle from the optical axis at the mode focus region.

forward hitting a flat mirror and is then reflected back as a reference beam; the other branch is reflected upwards passing through the Zeiss microscope objective (not showing in the Figure) and is reflected by the dimple back to interfere with the reference beam. The Twyman-Green interference patterns are monitored using a CCD camera (also not showing) at the location where the glass slide is, to make sure that the beam wavefronts are aligned to the dimple surface, as shown in 3.7(b), indicated by the proper Twyman-Green interference patterns.

After the optical adhesive is cured, it is desirable to remove the edge of the dimple substrate. This helps prevent the DBR mirror at the other side of the cavity from touching or crashing the substrate when the DBR mirror is slightly tilted, because the gap between the two is only about 20 μm, as shown in Fig. 3.1. We put the microscope objective with the dimple substrate on a lathe and grind the substrate carefully using a tiny drum sander so that a small mesa with a diameter about 3 mm is left. During the grinding, the dimple is covered and protected by Crystalbond 509 from contamination, which can be easily cleaned afterwards. Figure 3.8 shows the finished piece of a glued dimple substrate on top of a Zeiss microscope objective,

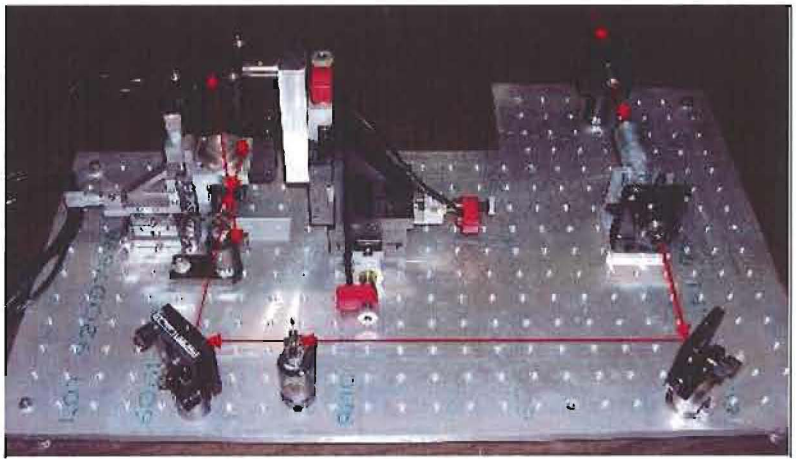

(a)

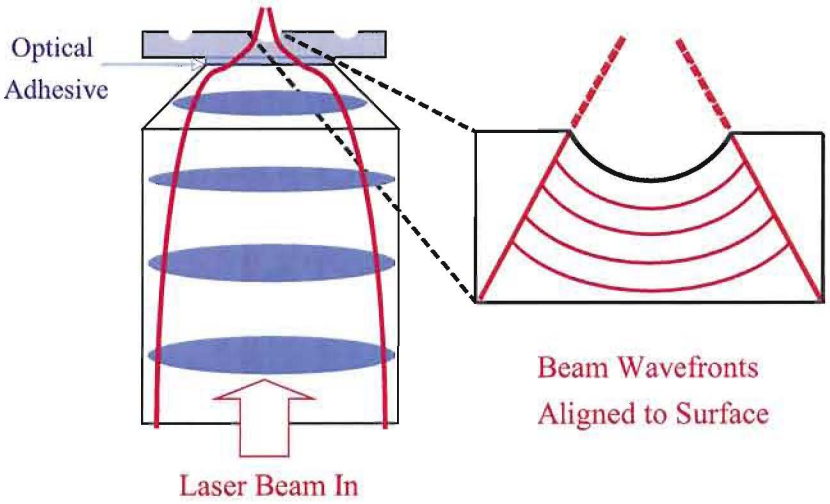

(b)

FIGURE 3.7: (a) A Twyman-Green interferometer. (b) A coated dimple is glued using index-matched optical adhesive to the face of a microscope objective in such a way that the beam wavefronts match the dimple surface.

which now is one end of our micro-cavity. The mesa on top of the objective is the micro-concave mirror substrate. The dimple is in the center of the mesa and is too small to be seen clearly.

(a) (b)

FIGURE 3.8: Top view (a), and side view (b) of a glued micro-concave mirror substrate on top of a Zeiss microscope objective (NA = 1.3).

There are two factors that can change the optical path length inside the optical adhesive layer, which consequently causes the beam wavefronts mismatch to the dimple. One factor is the change of the refractive index of the optical adhesive during UV curing. In order to compensate for this effect, we offset the dimple position a little bit empirically before curing so that after curing the dimple position is close enough if not perfectly, to the right position. The other is the change of the physical thickness of the optical adhesive layer, for instance caused by relatively large change of ambient temperature. Therefore, it is not easy to match the beam wavefronts with the dimple surface perfectly. Even if it is perfectly aligned in the first place, it can still change under other circumstances, for example when cooling down the semiconductor sample at the other side of the cavity. So we need to be able to further control an input beam wavefronts by mode-matching optics, which will be discussed in the next section.

3.2.3 Integrated DBR Mirror with QDs

Semiconductor planar DBR mirrors with exceptionally good surface smoothness and high reflectivity can be grown by MBE techniques [147]. Our UA collaborators found that the surface roughness on transverse length scales relevant for our needs ($\sim 1\,\mu$m) is equal to that of the best polished super dielectric mirrors of the type used in atomic cavity-QED experiments. Figure 3.9 shows a comparison of two kinds of mirrors—the MBE-grown and a commercial super dielectric mirror. The figure plots the power spectral density (PSD) of surface roughness versus transverse spatial frequency, measured with a Wyko interferometer. It is seen that the planar semiconductor mirror has far larger roughness for low spatial frequencies, while the commercial super dielectric mirror is slightly rougher at spatial frequencies above 1000 mm^{-1}, or length scales larger than one micron, the region of interest for our cavity, since the mode waist is on this scale.

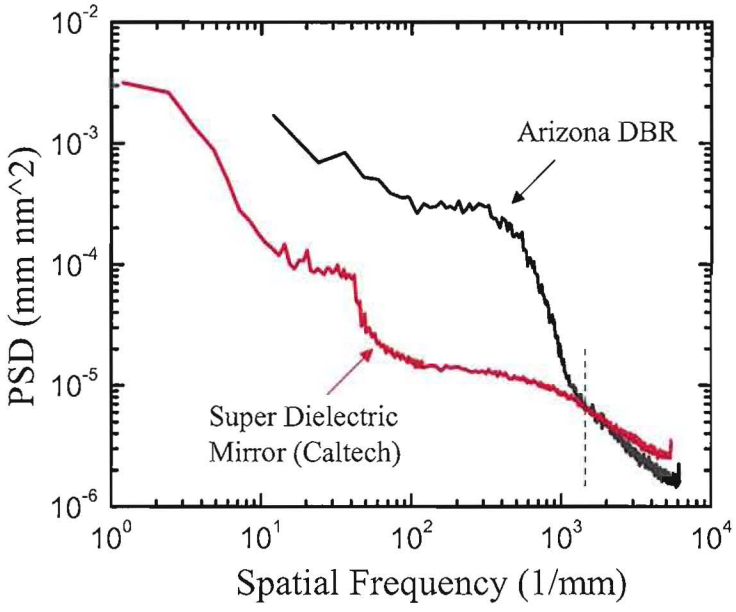

FIGURE 3.9: Measured surface roughness of a DBR mirror grown at the University of Arizona and the super dielectric mirror used at Caltech with a Wyko interferometer.

The GaAs QDs that we use are interface-fluctuation quantum dots (IFQDs). They are formed through the influence of monolayer-thick interface fluctuations during the MBE-growth of a quantum well (QW) [100, 111]. Our team has succeeded in growing good-quality IFQDs on top surface of high-quality DBRs. The sample used in this experiment is CAT96 and its design is shown in Fig. 3.10. The bottom mirror consists of 22.5 pairs of $Al_{0.24}Ga_{0.76}As$/AlAs quarter-wavelength stack grown on a GaAs substrate, which is removed later to reduce optical absorption. The GaAs IFQDs are formed in a 3.86-nm-thick QW embedded in the middle of a wavelength-thick spacer layer on top of the DBR mirror to place the QDs at an antinode of the cavity. The exciton transition in these QDs has a relatively large dipole matrix element ($\sim$ 60 Debye), enabling it to interact strongly with the cavity field.

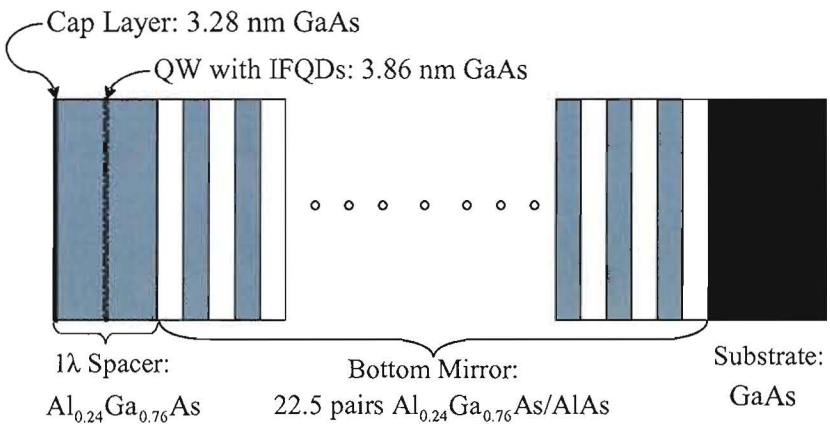

FIGURE 3.10: The design of CAT96. GaAs IFQDs are formed in a 3.86 nm GaAs QW in the middle of the one-wavelength spacer layer ($Al_{0.24}Ga_{0.76}As$). The cap layer is for preventing the spacer layer from oxidizing.

The reflectivity of the DBR mirror versus wavelength at room temperature has also been measured. Figure 3.11 shows the measurements on two different spots on CAT96. Figure 3.11(a) shows the data taken from a spot 10 mm from growth center (GC). The theoretical peak reflectivity of this example is 98.12% at the wavelength 794.83 nm. The dip at the wavelength 773.8 nm in the reflectivity measurement is due to the one-wavelength spacer layer acting as a micro-cavity. This means that a laser

at this wavelength is in resonance with the spacer layer and the light field will have an anti-node right in the middle of the spacer layer where the QDs are. Therefore, it is important to probe the cavity-QD interaction around this wavelength to maximize the interaction.

Since the farther from GC, the thinner the sample is and hence the spacer layer, the dip in the reflectivity measurement will shift to shorter wavelengths. Figure 3.11(b) shows the data taken from a spot 13 mm from GC. The theoretical peak reflectivity is still 98.12% at the wavelength 794.83 nm, but the dip shifts to a shorter wavelength 765.2 nm, as expected. Thus it is also important to scan the sample laterally so that we can probe the cavity-QD interaction at different spectral or wavelength regions. When the DBR mirror is cooled down to 10-17 K, the reflectivity measurement (spectrum) shifts about 10 nm to shorter wavelength as a whole, mainly due to the changes in the refractive indices of the layer materials and their physical thicknesses.

The presence of QDs is verified by photoluminescence (PL) spectra in free space at low temperature (7 K), showing broad (quasi-continuous) emissions in the 750-770 nm wavelength region for CAT96, and 750-790 nm wavelength region for a similar DBR CAT97 (22.5 pairs of $Al_{0.25}Ga_{0.75}As$/AlAs), as shown in Fig. 3.12(a) and (b) respectively. This indicates many QDs overlap spectrally on both DBRs. The PL spectrum was excited with a diode laser at a wavelength 685 nm with a power 33 μW. The difference between x values (0.24 and 0.25) in $Al_xGa_{1-x}As$ for two samples is within the uncertainty of the growth rates.

As shown above, there are many QDs overlap spectrally. It is not easy to identify both spatially and spectrally isolated single QDs, which requires a nano-scope and a high-resolution spectrometer. Figure 3.13 shows a set of nano-scope PL spectra [101] for a sequence of different locations with a spatial step of 300 nm in the QW plane on the DBR CAT97. The broader PL emission lines in the upper traces are inhomogeneously broadened and can be fit approximately by Gaussian distributions,

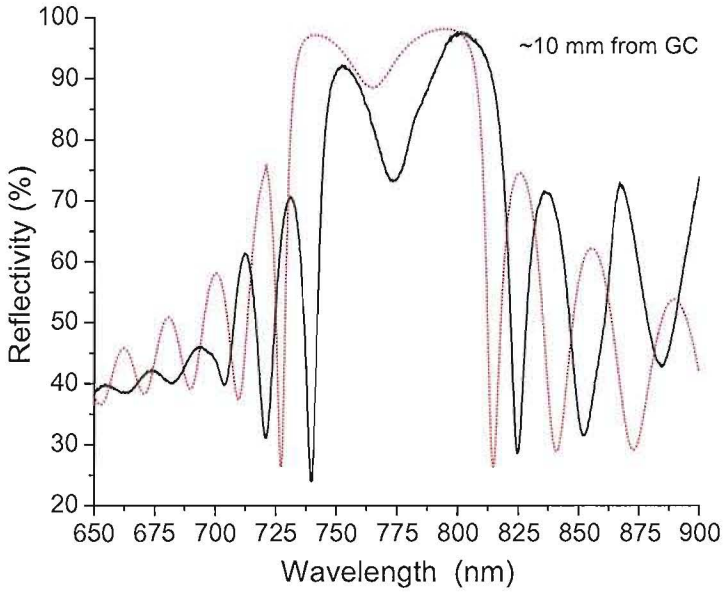

(a)

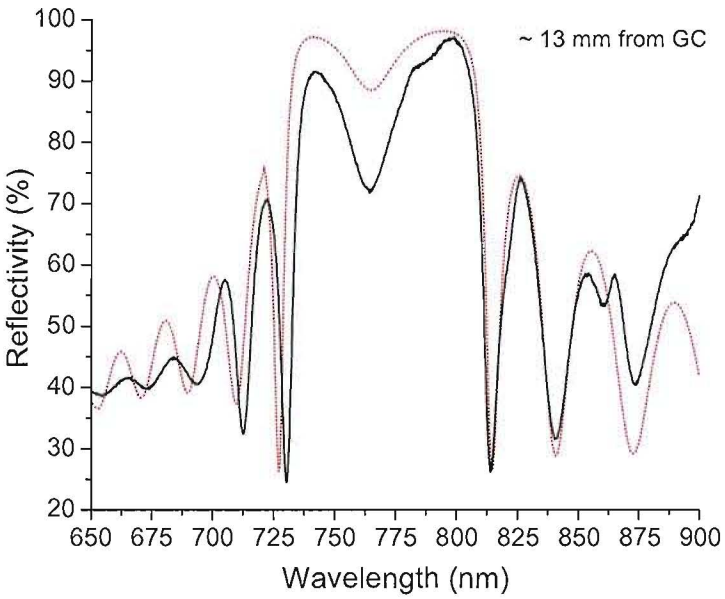

(b)

FIGURE 3.11: Reflectivity versus wavelength of CAT96. The data (solid lines) were taken on spots about 10 mm (a), and 13 mm (b) from GC on the sample at 300 K. The dot lines are the theoretical fits. The fitting parameters are: $\lambda_{\text{target}} = 770$ nm, $n(Al_{0.24}Ga_{0.76}As) = 3.524337$ and $n(AlAs) = 3.003109$ [University of Arizona].

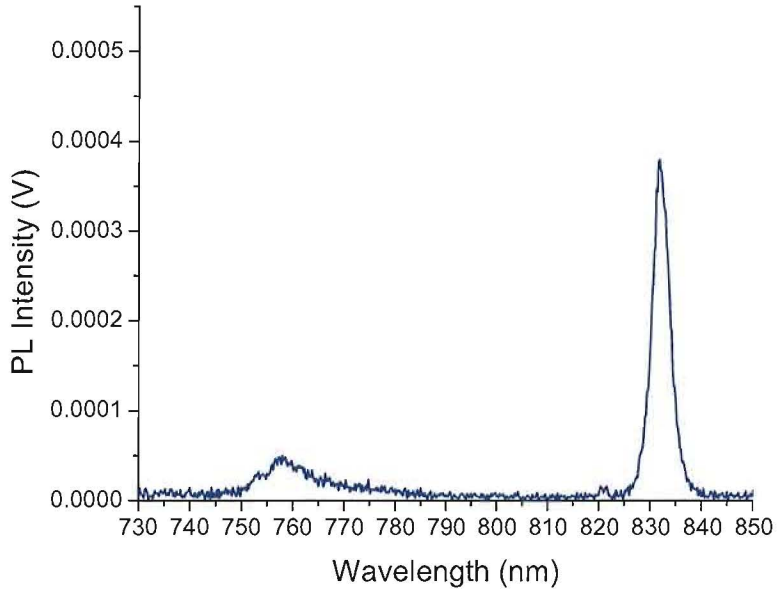

(a)

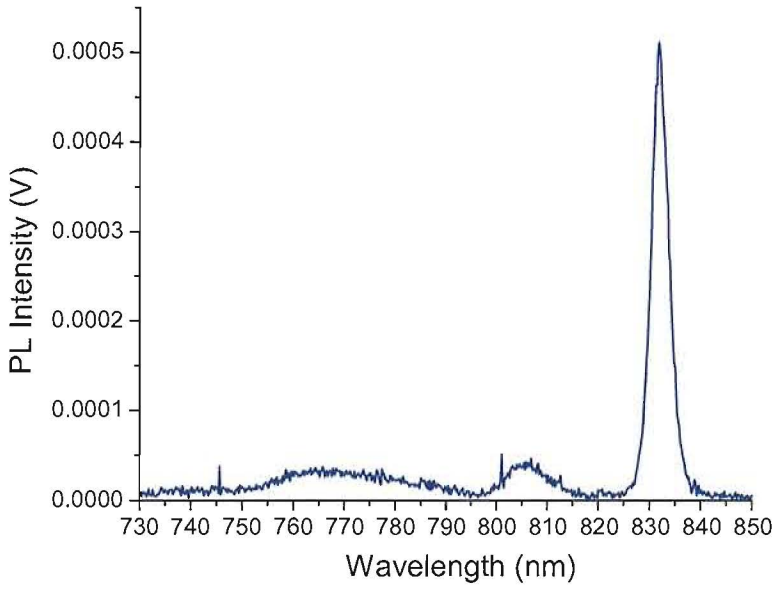

(b)

FIGURE 3.12: PL spectra of samples CAT96 (a), and CAT97 (b) at 7 K. The excitation laser wavelength is 685 nm with an excitation power 33 μW [University of Arizona].

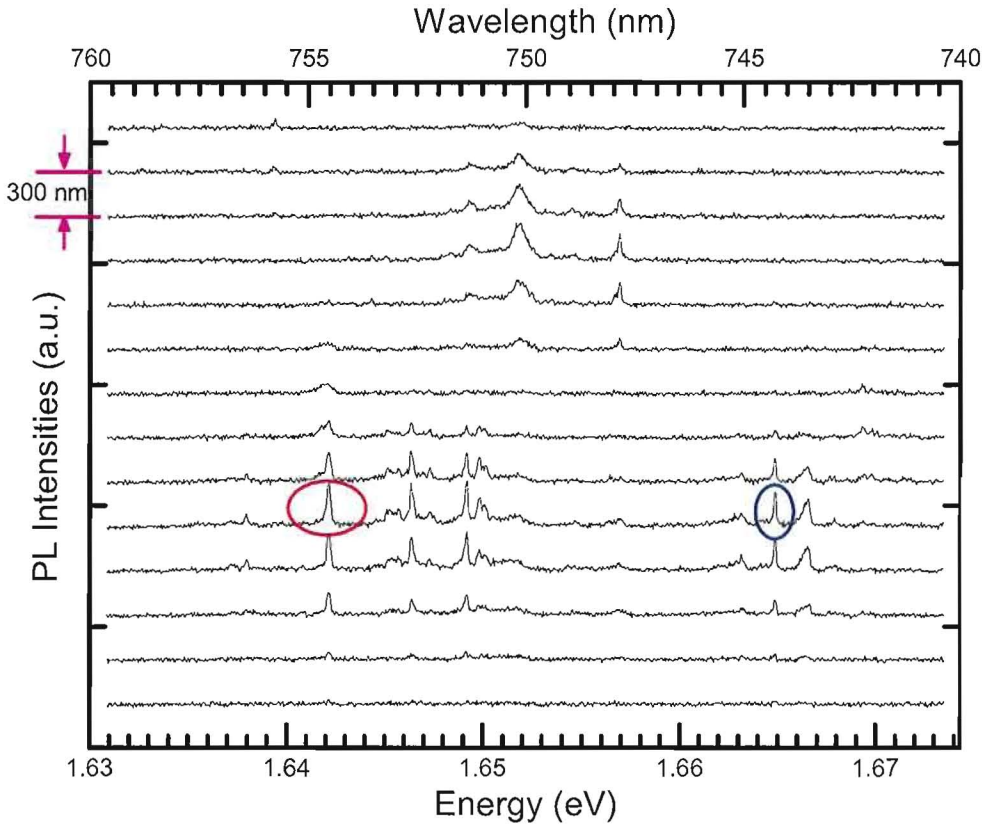

FIGURE 3.13: Nano-scope spectral scans of different spatial locations on UA-grown sample (CAT97) at 7 K, showing spectrally and spatially well isolated single QD emission lines (circled) [University of Arizona].

and are likely caused by emissions from spatially close QDs with different lateral sizes and hence different emission frequencies. Some of the narrower PL emission lines in the lower traces can be fit by Lorentzian distributions, which are homogeneously broadened, signifying isolated single quantum emitters, and can be identified as emissions from single QDs, for example, the circled ones. One of them is in our 750–760 nm target region and is spectrally well isolated. The emission lines at the same energy (wavelength) in the adjacent traces are also from this specific QD and indicate that it is also spatially well isolated ($\sim 600\,\text{nm}$) from other QDs. Based on this measurement on CAT97, we expect there are also isolated single QDs on CAT96.

Before being used as a cavity mirror, the GaAs substrate for growing the DBR mirror needs to be removed in order to reduce absorptions. Figure 3.14 shows the procedure to prepare the sample onto a sapphire disk ready for using in a cavity. We

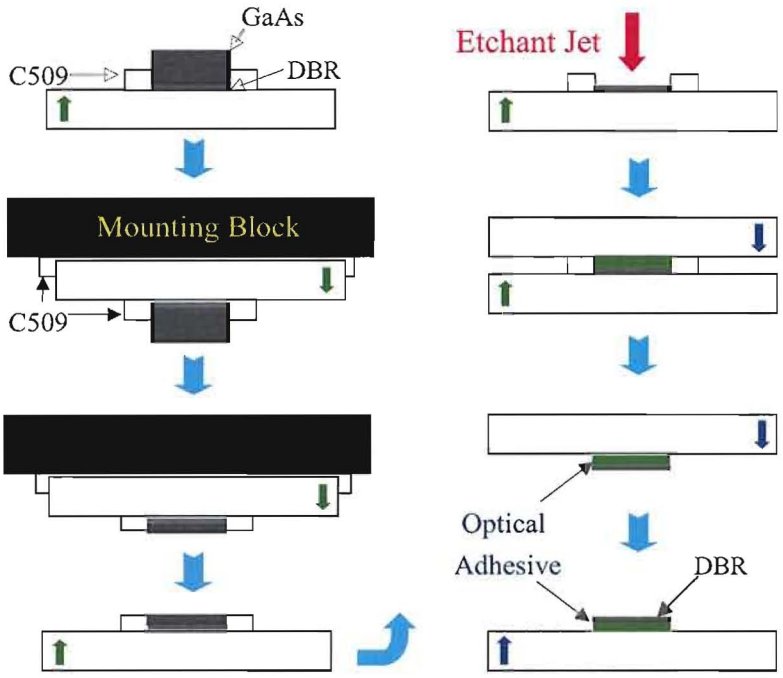

FIGURE 3.14: The procedure to remove the GaAs substrate of a DBR mirror and to glue it onto a sapphire plate.

first glue the spacer layer side of the DBR mirror using a heat adhesive Crystalbond 509 (C509) onto a sapphire plate with GaAs substrate facing upward. Then we glue the sapphire disk onto the mounting block of a lapping fixture (South Bay Technology, Inc.), still with C509. After that, we mechanically polish away most of the GaAs substrate so there is about 25-40-μm-thick sample left, including both the DBR mirror and the leftover GaAs substrate, because we do not want to polish the sample too thin and damage the DBR mirror. The total thickness of the DBR mirror with QDs is about 3 μm thick. The rest of the GaAs substrate will be selectively etched away using a method described in [148]. The sample is placed into position of a Jet Thinning Instrument (South Bay Technology, Inc.) under the jet stream of the etching solution. The etching solution is a mixture of hydrogen peroxide (H_2O_2) 30% concentrated and ammonium hydroxide (NH_4OH) 58% concentrated. After removing all the GaAs so that the first layer of AlAs is exposed, we mount a second sapphire plate onto the AlAs side using the UV-cured optical adhesive (Norland Optical Adhesive 88). AlAs can get easily oxidized in the air, so extra care should be taken during this step and should be finished as quickly as possible. Finally, after curing the optical adhesive, we remove the first sapphire plate so that the spacer layer of the DBR mirror is exposed and will be ready for use as a cavity mirror.

3.3 Cavity Construction, Testing and Modeling

Once both of the cavity mirrors are fabricated and ready for use, like described in Sec. 3.2, we assemble them together with other components and construct a high-quality hemispherical cavity using our 60-micron concave mirror and a planar semiconductor DBR (CAT96), as shown in Fig. 2.2. The sapphire plate with the semiconductor DBR mirror is first glued to a low-temperature holder using thermally conductive epoxy (Epo-Tec T7110); then mounted to a PZT actuator jointed by a thermal insulator, as shown in Fig. 2.3, which is a hollow cylinder made from a polymer (Vespel from DuPont) having a low coefficient of thermal conductivity.

This allows us to cool down the sample while not affecting the PZT. The PZT is driven by a laser-referenced feedback loop for stabilizing the length of the cavity. The sample assembly is mounted on a tripod system, supported by three Burleigh UHVL Inchworm Motors, to control precisely its longitudinal position and its angle with respect to the curved mirror. The tripod also contains an x-y nano-positioner, which can laterally scan the mode waist in a 50×50 μm^2 region, essential for scanning and addressing a single QD, as also shown in Fig. 2.3. The system operates inside a high-vacuum chamber ($10^{-8} - 10^{-10}$ mbar), to allow cooling the DBR mirror to around 10-17 K to reduce QD dephasing rates and to avoid coating of the DBR mirror by cryopumping and attendant absorption and scattering.

As we have mentioned in the previous section, we need to be able to control the input laser beam's wavefronts in order to match it to the dimple, after we have closed up the UHV chamber. In this section, we first discuss how to mode match an input laser beam efficiently into the fundamental mode of the micro-cavity. Then we will discuss tests of the cavity mode structure and compare the mode properties at both room temperature and low temperature. Based on numerical modeling of this hybrid hemispherical cavity, we highlight some interesting phenomena associated with the high solid-angle design and the semiconductor DBR mirror.

3.3.1 Mode-matching a Laser Beam into a Cavity Mode

The strongest interaction between an optical center and a cavity mode is its interaction with the lowest-order transverse mode of the cavity, since the lowest-order transverse mode by definition has the highest spatial confinement and smallest waist size and the lowest leakage or diffraction losses; or in other words, the field has the largest strength (intensity) per photon. For an optical center, the cavity-QED strong coupling will likely first happen between the lowest-order transverse mode and the optical center. In order to probe the interaction between a QD and a cavity mode, we need to be able to mode match a probe laser beam into a desired cavity

mode properly, for example into the HG00 mode. Moreover, there may be other complications associated with higher order spatial modes of a hemispherical cavity, for instance, certain frequency splittings in higher order spatial modes predicted in Ref. [98].

We assume, for a given cavity, that its length has already been stabilized, either passively by filtering and damping or/and actively by a feedback control loop such as the Pound-Drever-Hall scheme [149, 150]. In other words, we have already mode-matched the longitudinal degree of freedom of the cavity. There are two major types of misalignments of the transverse degrees of freedom [151]. Here we use term alignment to mean transverse displacement and angular orientation of an input beam; and mode-matching to indicate waist size and position control. Sometimes, where there is no ambiguity, we use alignment to mean both.

If an input laser beam is slightly misaligned in angle or transversely displaced with respect to the cavity optical axis, first-order HG modes are introduced. Similarly, if a beam waist's size and position do not match the cavity waist's size and position, second-order HG modes (first-order LG modes) are introduced. In terms of phase, a transverse displacement and mismatch of waist size of an input beam with respect to the cavity axis and waist size give rise to inphase coupling to, respectively, the first- and second-order transverse HG modes of the cavity. On the other hand, angular misalignments and waist position mismatch lead to coupling to these modes in quadrature phase.

To excite the fundamental transverse cavity mode efficiently, it is necessary to align an input beam correctly with respect to the cavity optical axis and also shape and focus the input laser beam use mode-matching optics. Let's consider the alignment of a two-mirror Gaussian cavity having two spherical mirrors as discussed in Chapter II, again shown here in Fig. 3.15.

Associated with every stable optical cavity in the paraxial limit is a set of spatial eigenmodes, either HG modes or LG modes, both of which form a complete

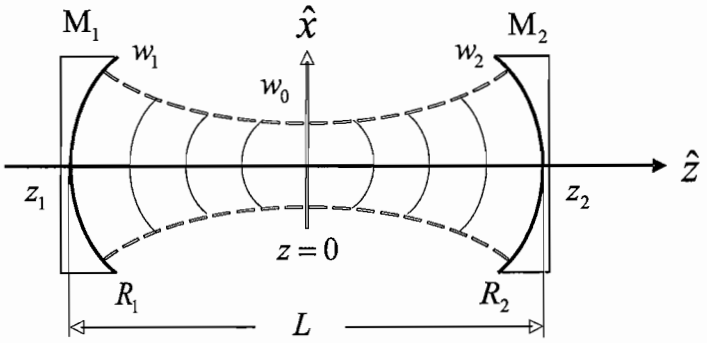

FIGURE 3.15: Analytical model and notation for a stable two-mirror cavity. w_0 is the radius of the beam spot at the Gaussian beam waist $z = 0$. w_1 and w_2 are the beam spot sizes at two cavity mirrors M_1 and M_2 with radii of curvatures R_1 and R_2 at positions z_1 and z_2, respectively. L is the cavity length.

set. Physically, these eigenmodes describe electric field distributions which can propagate back and forth between the mirrors along the cavity optical axis with minimum diffraction losses and without changing shapes. A general input beam can be expanded and expressed as a linear combination of these eigenmodes. There are six parameters which describe an input beam alignment and mode matching: two rotations, two transverse translations and the waist size and axial position, all measured at or from the cavity waist at $z = 0$.

For simplicity, we discuss the transverse displacement and angular rotations only in the x dimension, since the y dimension will have identical expressions. The normalized spatial eigenmodes in Cartesian coordinates are HG modes; the three lowest orders are:

$$U_0(x) = \left(\frac{2}{\pi w_0^2}\right)^{1/4} \exp\left[-\left(\frac{x}{w_0}\right)^2\right] \tag{3.1}$$

$$U_1(x) = \left(\frac{2}{\pi w_0^2}\right)^{1/4} \frac{2x}{w_0} \exp\left[-\left(\frac{x}{w_0}\right)^2\right] \tag{3.2}$$

$$U_2(x) = \left(\frac{2}{\pi w_0^2}\right)^{1/4} \left(\frac{4x^2}{w_0^2} - 1\right) \exp\left[-\left(\frac{x}{w_0}\right)^2\right], \tag{3.3}$$

where w_0 is the waist size, as defined and given in Eq. (2.18) by cavity-g factors.

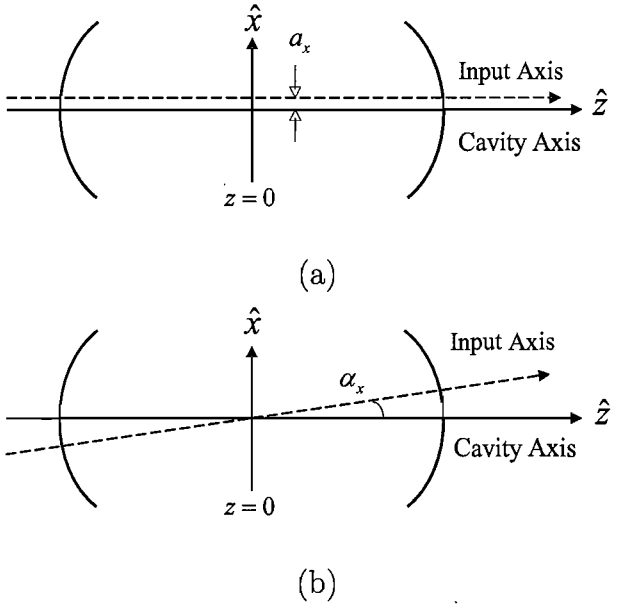

FIGURE 3.16: Misalignments of an input beam axis with respect to the cavity axis: (a) transverse displacement a_x; (b) tilt through an angle α_x.

Rewrite it explicitly using the cavity mirrors' radii of curvatures and the cavity length L,

$$w_0^2 = \frac{\lambda}{\pi}\sqrt{\frac{L(R_1-L)(R_2-L)(R_1+R_2-L)}{(R_1+R_2-2L)^2}}. \tag{3.4}$$

U_0 describes the fundamental mode, U_1 and U_2 are the first and second off-axis modes, respectively. We assume that the input beam $\Psi(x)$ is Gaussian and aligned, so that $\Psi(x) = AU_0(x)$ and if we translate the input beam a small amount a_x, as in Fig. 3.16(a), $\Psi(x)$ becomes

$$\Psi(x) = AU_0(x-a_x) \tag{3.5}$$

$$= A\left(\frac{2}{\pi w_0^2}\right)^{1/4}\exp\left[-\left(\frac{x-a_x}{w_0}\right)^2\right]. \tag{3.6}$$

The exponential can be expanded and if $a_x/w_0 \ll 1$, we keep only the first order term:

$$\Psi(x) \simeq A\left(\frac{2}{\pi w_0^2}\right)^{1/4}\left(1+2a_x\frac{x}{w_0^2}\right)\exp\left[-\left(\frac{x}{w_0}\right)^2\right], \tag{3.7}$$

or

$$\Psi(x) \simeq A\left[U_0(x) + \frac{a_x}{w_0}U_1(x)\right]. \tag{3.8}$$

Thus we see that a small transverse displacement of the input beam gives rise to an in-phase coupling of the first off-axis mode of the cavity.

Now we consider the case when an input beam is traveling along the cavity axis z and is tilted with respect to the cavity axis. In general, the wave-front curvature along the axis of travel is spherical so that the off-axis phase is different from the on-axis phase. At the waist, however, the curvature is infinite so that the phase is constant along the transverse plane. We will assume here that the input beam waist matches the cavity waist and it is rotated about the cavity waist through a small angle α_x as shown in Fig. 3.16(b). As we project the input beam onto the cavity transverse plane, we see in Eq. (3.10) that its magnitude is no different from the input to first order in α_x

$$|\Psi(x)| = |\Psi(x')|(\cos\alpha_x)^{-1} \tag{3.9}$$

$$\simeq |\Psi(x')|(1 + \alpha_x^2/2 + O(\alpha_x^4)). \tag{3.10}$$

However, the phase of the wave now varies along x

$$\varphi(x) = \left(\frac{2\pi}{\lambda}\right) x \sin\alpha_x \simeq \frac{2\pi\alpha_x x}{\lambda}, \tag{3.11}$$

or

$$\Psi(x) \simeq AU_0(x)\exp\left(i\frac{2\pi\alpha_x x}{\lambda}\right). \tag{3.12}$$

The exponential may be expanded, and only the lowest-order terms are kept when $(2\pi\alpha_x w_0)/\lambda \ll 1$. Physically this limit says that the tilt angle is smaller than the far-field divergence angle of the beam. $\Psi(x)$ becomes

$$\Psi(x) \simeq AU_0(x)\left(1 + i\frac{2\pi\alpha_x w_0}{\lambda} + O(\alpha_x^2)\right), \tag{3.13}$$

or

$$\Psi(x) \simeq A\left[U_0(x) + i\frac{\pi\alpha_x w_0}{\lambda}U_1(x)\right]. \tag{3.14}$$

In words, a tilt couples into the first off-axis mode as does a transverse displacement but with a 90^0 phase shift.

Then we calculate coupling due to small mode-mismatching, it is more convenient to work in polar coordinates [96]. The eigenmodes of the cavity are given by the generalized Laguerre polynomials L_l^p weighted by a Gaussian. p and l are the radial and angular mode numbers, respectively. We are interested here in the modes with no angular dependence and so set $l = 0$. At the waist the two lowest-order radial modes are

$$V_0(r) = \sqrt{\frac{2}{\pi}}\frac{1}{w_0}\exp\left(-\frac{r^2}{w_0^2}\right), \tag{3.15}$$

$$V_1(r) = \sqrt{\frac{2}{\pi}}\frac{1}{w_0}\left(1-\frac{2r^2}{w_0^2}\right)\exp\left(-\frac{r^2}{w_0^2}\right), \tag{3.16}$$

where r is the radial coordinate and the cavity waist size is still w_0. Note that the first order LG mode is similar and equivalent to second order HG mode.

This time suppose that the input beam is aligned and almost mode-matched except that the beam waist size w_0' is different from the cavity waist size w_0 by a small fraction ε, $w_0' = w_0(1+\varepsilon)$ as in Fig. 3.17(a). Now the wavefunction is

$$\Psi(r) = A\sqrt{\frac{2}{\pi}}\frac{1}{w_0}(1+\varepsilon)\exp\left[-\frac{r^2}{w_0^2}(1+\varepsilon)^2\right]. \tag{3.17}$$

Expanding the exponential and retaining terms to first order in ε

$$\Psi(r) \simeq A[V_0(r) + \varepsilon V_1(r)]. \tag{3.18}$$

Thus a small size mismatching excites a fraction ε of the first order LG radial mode, or equivalently second order HG mode.

The last case to be treated is the one in which the beam size is correctly matched, but the position of the waist is not as shown in Fig. 3.17(b). The input beam waist

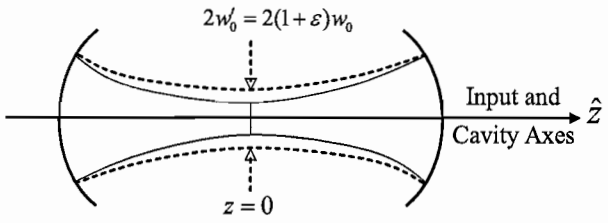

(a)

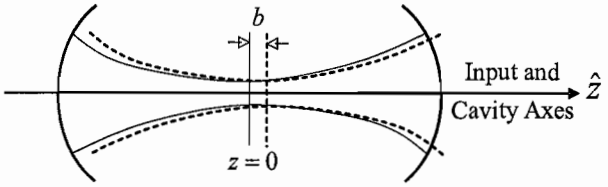

(b)

FIGURE 3.17: Mode Mismatch of an input beam (dashed curve) with respect to the cavity mode (solid curve): (a) waist size mismatch; (b) axial waist position shift.

is displaced a distance b along the cavity axis z from the cavity waist position at $z = 0$. This means that at the cavity waist the input beam has a finite radius of curvature. In order to describe the modes evolve along the z axis, we need to express the eigenmodes in a more general form. Neglecting a common phase factor, the two lowest-order modes are

$$V_0(r,z) = \sqrt{\frac{2}{\pi}}\frac{1}{w(z)}\exp\left[-r^2\left(\frac{1}{w^2(z)} + i\frac{\pi}{\lambda R(z)}\right)\right], \tag{3.19}$$

$$V_1(r,z) = \sqrt{\frac{2}{\pi}}\frac{1}{w(z)}\left(1 - 2\frac{r^2}{w^2(z)}\right)\exp\left[-r^2\left(\frac{1}{w^2(z)} - i\frac{\pi}{\lambda R(z)}\right)\right]. \tag{3.20}$$

$w(z)$ and $R(z)$ are the spot size and the radius of curvature of the wave front at position z along the cavity axis, respectively, as given in Eqs. (2.10) and (2.11)

$$w(z) = w_0\sqrt{1 + \left(\frac{z}{z_R}\right)^2}, \tag{3.21}$$

$$R(z) = z + \frac{z_R^2}{z}, \tag{3.22}$$

where $z_R \equiv \pi w_0^2/\lambda$ is the Rayleigh range. At a short distance b from the cavity waist so that $\beta \equiv b/z_R \ll 1$, the curvature becomes $R(b) = \beta^{-2}$. And, to first order in β, the spot size is essentially that of the waist $w(b) \simeq w_0$. Therefore, the axially translated input beam at the cavity waist looks like

$$\Psi(r,b) = A\sqrt{\frac{2}{\pi}}\frac{1}{w_0}\exp\left[-\frac{r^2}{w_0^2}(1-i\beta)\right]. \tag{3.23}$$

Expanding an exponential gives the expression for the translated beam in terms of eigenmodes

$$\Psi(r,z) = A\left[V_0(r,z) + i\frac{b}{2z_R}V_1(r,z)\right]. \tag{3.24}$$

We see that an axial displacement of the input waist with respect to the cavity waist causes a coupling to the first order LG radial eigenmode or second order HG eigenmode, but in quadrature with the fundamental mode. We conclude that any small misalignments causes a coupling into one of the lowest-order modes with a phase dependent upon the types of misalignment.

Looking from a different point of view, a misalignment can occur not only by changing the input beam direction and so forth but also by changing the orientation or position of the cavity mirrors. The positions are usually fixed, but the orientations are often subject to drift. In general, a mirror tilt through an angle θ will cause a transverse displacement as well as a rotation of the optical axis, thereby giving rise to a linear combination of the inphase and inquadrature components of the first off-axis mode. Conversely, for each dimension, a proper linear combination of tilts from the two mirrors will give rise to a pure transverse displacement and a pure rotation of the optical axis.

Name the mirror tilts θ_1 and θ_2. The distances $|z_1|$ and $|z_2|$ of the waist from the mirrors as shown in Fig. 3.15 are given by Eq. (3.26)

$$z_1 = -\frac{g_2(1-g_1)}{g_1+g_2-2g_1g_2}L, \tag{3.25}$$

$$z_2 = \frac{g_1(1-g_2)}{g_1+g_2-2g_1g_2}L. \tag{3.26}$$

Note that if mirror M_1 is located to the left of the beam waist, so that the waist is inside the cavity as in Fig. 3.15, the z_1 as measured from the waist will be a negative number. Geometrical considerations show that the optical axis executes a pure transverse displacement when

$$\theta_2 = \frac{R_1}{R_2}\theta_1, \tag{3.27}$$

giving a transverse displacement

$$a = R_1 \sin\theta_1, \tag{3.28}$$

and a pure rotation about the waist when

$$\sin\theta_2 = \frac{1 - z_2/R_2}{1 - |z_1|/R_1} \sin\theta_1, \tag{3.29}$$

giving a tilt angle

$$\sin\alpha = \frac{\sin\theta}{1 - |z_1|/R_1}. \tag{3.30}$$

In the above expressions R_1 and R_2 are both positive if the centers of curvatures are as drawn in Fig. 3.15; z_1 is negative and z_2 is positive as shown. Positive θ is counterclockwise.

For a hemispherical cavity, we will see that a tilt of the planar mirror causes a pure rotation, a tilt of the concave mirror induces a pure displacement, both of which will give rise to first order off-axis HG modes misalignments. In experiment, the misalignments, for a hemispherical cavity, can be greatly suppressed and even eliminated by careful alignments of the input probe laser, however, it is not easy to eliminate the mode mismatch without additional mode-matching optics. We use a system consisting three lenses, two convex lenses and a concave lens, which is similar to an afocal system, or a zoom-lens system, to control the mode matching of our hemispherical cavity, see Fig. 3.18.

We mount our mode-matching optics on a linear rail. The optics can be easily inserted into and removed away from the optical path without ruining the beam

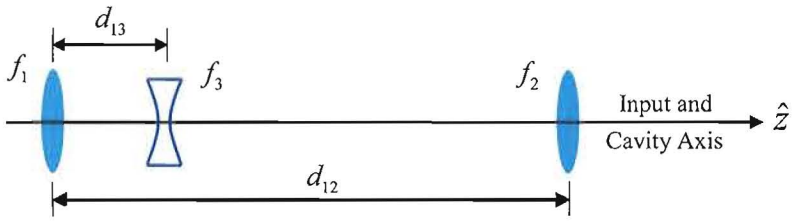

FIGURE 3.18: The zoom-lens system used in our experiment: $f_1 = f_2 = f$, $(-f_3) < f/2$. d_{12} is the distance between the two convex lenses and d_{13} is the distance between the first convex lens and the concave lens.

alignment, enabling us to compare the cavity transmission spectra with and without mode-matching optics. Figure 3.19 shows six well-defined cavity mode images observed for different cavity lengthes or frequencies without mode-matching optics in position. We label them using HG and LG notations, since they are qualitatively similar to the Hermite-Gauss (HG) or Laguerre-Gauss (LG) modes that are applicable in the paraxial limit [96].

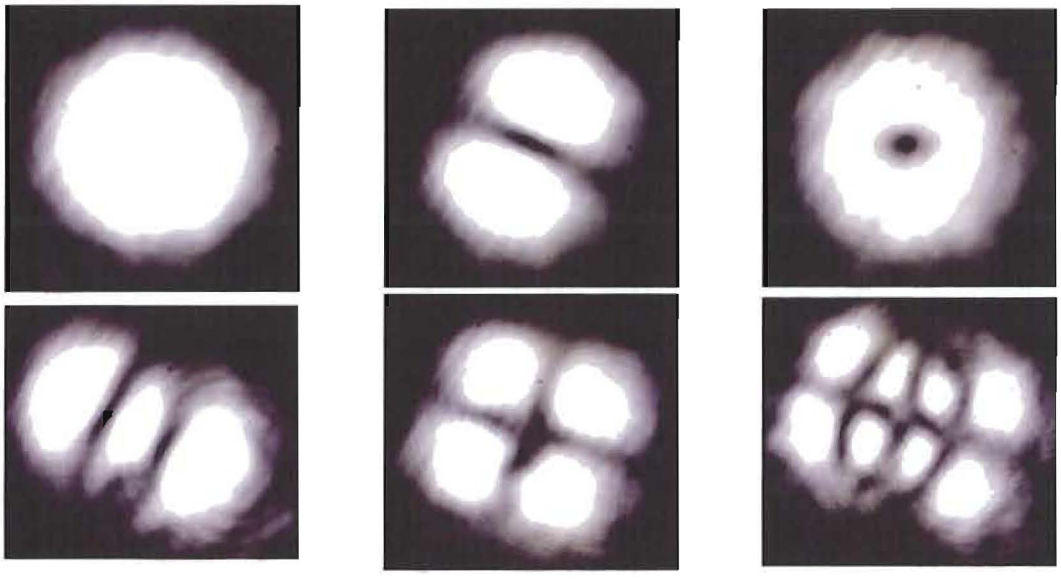

FIGURE 3.19: Measured mode images of the 60 μm hemispherical cavity. The modes are HG00, HG01, and LG01, top left to right; HG02, HG11, and HG13, bottom left to right, respectively.

By using this zoom-lens mode-matching system, for a given Gaussian beam, we are able to mode-match most of the beam into the fundamental mode of the cavity HG00 or LH00, by varying d_{13}. Figure 3.20(a) shows a laser-wavelength scan of the cavity transmission versus laser wavelength without the mode-matching optics. The strongest mode is the fundamental mode of the cavity, HG00 or LG00 mode, by which there are two higher-order even modes: HG02 (HG11) and HG13 (HG04 or HG22). The structure repeats itself every cavity free spectral range (FSR). The two small peaks at half FSR in between are two odd modes HG01 and HG03 (HG12). Figure 3.20(b), (c) and (d) show three laser-wavelength scans of the cavity transmission corresponding to three different d_{13} while keeping $d_{12} = 330$ mm, as compared with that of no mode-matching optics, as shown in Fig. 3.20(a). We can see that there is an optimal lens spacing $d_{13} = 110$ mm where the second order and the fourth order HG modes are greatly suppressed. But when the lens spacing is either longer or shorter than it, the higher order HG even modes come back. The third order HG mode is also suppressed, which is mainly due to better displacement and tilt alignments rather than the zoom-lens system. This example is for a given Gaussian beam used in our experiment. In general for other input beams, one can still achieve better mode matching by adjusting both d_{12} and d_{13}, or even using different lens combinations.

3.3.2 Testing and Modeling the Cavity Modes

Once we gained the ability to control the mode matching, we tested the cavity by passing a laser light through it and observing the cavity transmission and measuring its finesse. We probed and measured the transmission versus laser wavelength for a cavity containing a layer of QDs. Figure 3.21 shows four scans over the range of wavelength where the QDs absorb (745-765 nm).

The transverse-mode frequency-spacings become smaller as we approach the hemispherical limit by making the cavity longer. Our results are consistent with predictions for the hemispherical limit, paraxial-mode theory [96], which predicts

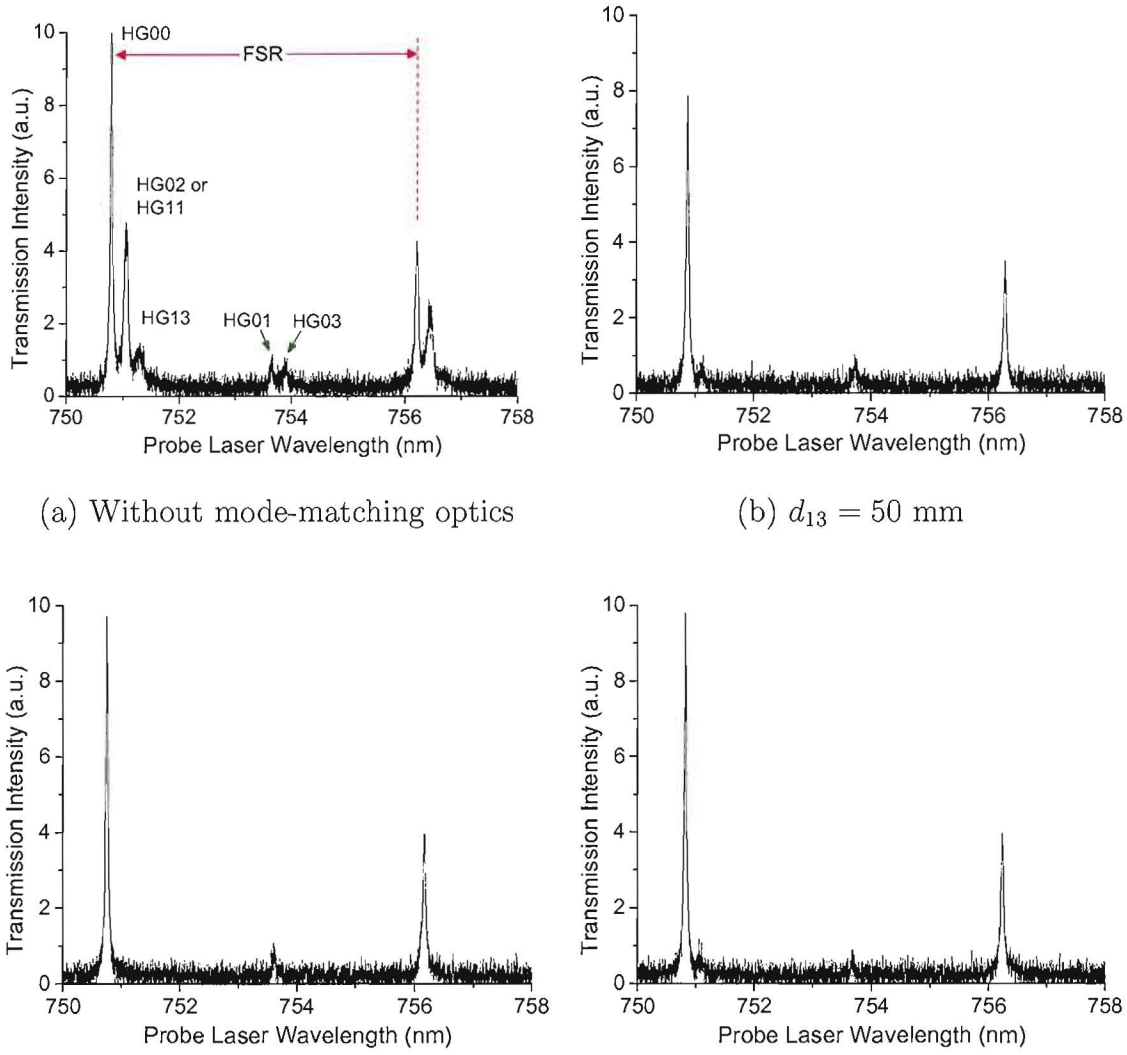

(a) Without mode-matching optics

(b) $d_{13} = 50$ mm

(c) $d_{13} = 110$ mm

(d) $d_{13} = 170$ mm

FIGURE 3.20: Mode-matching with different lens spacings d_{13}. In this experiment $f_1 = f_2 = +500$ mm and $f_3 = -200$ mm.

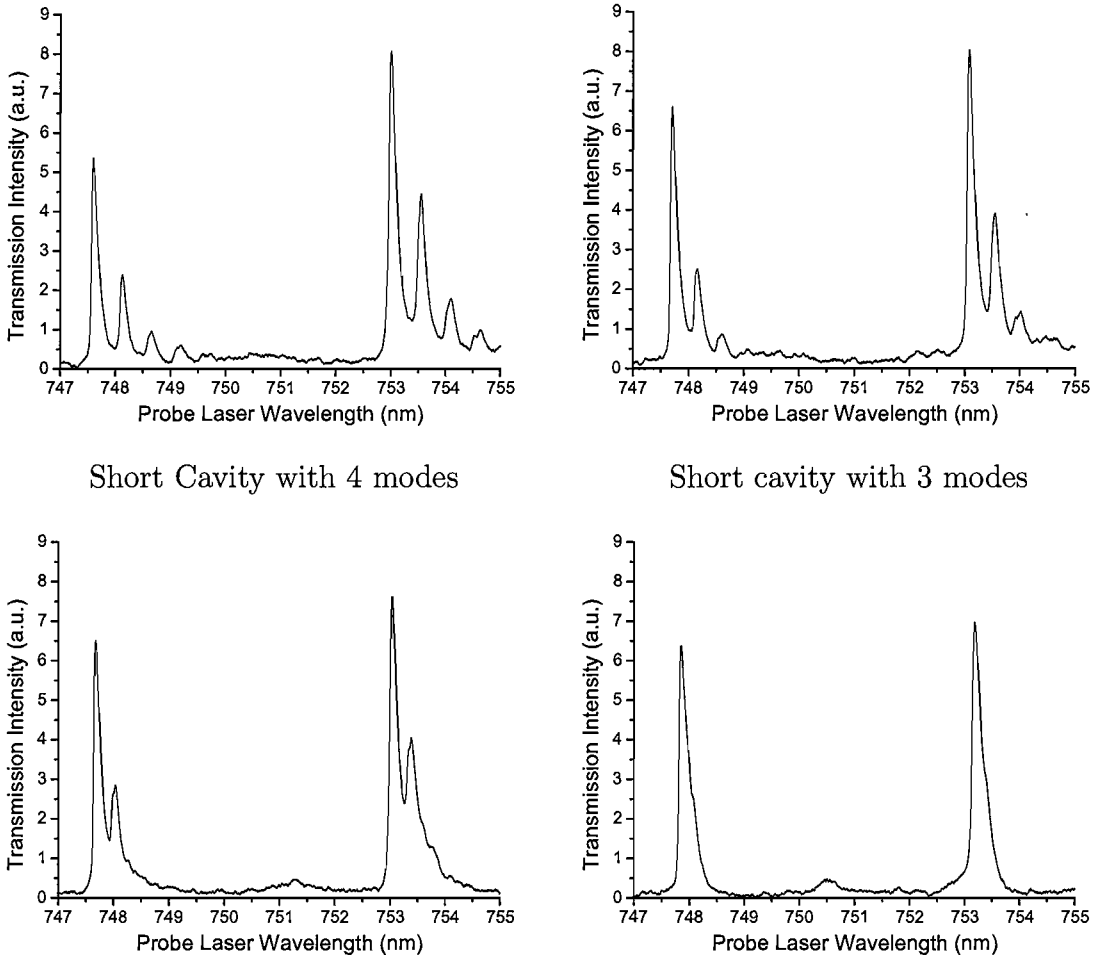

Short Cavity with 4 modes

Short cavity with 3 modes

Short Cavity with 2 modes

Hemispherical Limit

FIGURE 3.21: 60 μm hemispherical cavity transmission versus laser wavelength at room temperature. The cavity finesse is about 50 and the FWHM of the HG00 mode is about 50 GHz.

degenerate sets of modes, separated by $c/4L$, where L is the cavity length. The finesse is about 50 at room temperature and the full linewidth at half maximum (FWHM) of the HG00 mode is about 50 GHz. When we do a similar scan near 780 nm, where there is less absorption, the finesse increases to 200. This is an indication at room temperature that we are observing optical absorption of the QD layer in 745-755 nm range. The predicted finesse is 600 based on reflectivity measurements of the mirror alone. The lowered finesse is likely due to residual contamination in the mirror dimple.

When the DBR with QDs is cooled down to cryogenic temperature, there will be less absorption compared with that at room temperature, mainly due to fact that the absorption shifts about 10 nm to shorter wavelength such that we are probing at the red side of QDs distribution (absorption) where there are fewer QDs. Figure 3.22 shows three scans at 16.6 K. The highest finesse measured is 260, giving a cavity linewidth as narrow as 10 GHz. The typical homogenous linewidth of GaAs IFQDs that we use is broader than 15 GHz. The inhomogeneous linewidth of these QDs, however, can be as broad as hundreds of GHz. So with these parameters, our micro-cavity is capable of spectrally resolving single QDs.

If an input laser beam, typically a Gaussian beam, is not properly aligned and mode-matched to the transverse pattern of the lowest-order mode or the fundamental mode of the cavity HG00, the laser will also excite other higher-order transverse modes in the cavity, such as HG01, HG11 and LG01 modes, as shown in Fig. 3.19, or even a mixture of these modes. Since these transverse modes usually have slightly different resonant frequencies, tuning the probe laser allows us to observe a number of separate and frequency-shifted resonances for different transverse modes; but since the higher-order modes often have larger diffraction losses and thus lower Q values, the cavity response in the higher-order modes is often weaker than in the lower-order transverse mode, as shown in both Fig. 3.21 and Fig. 3.22.

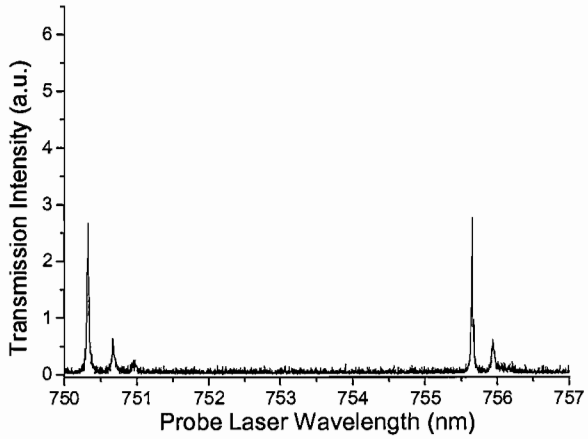

Short Cavity with 3 modes

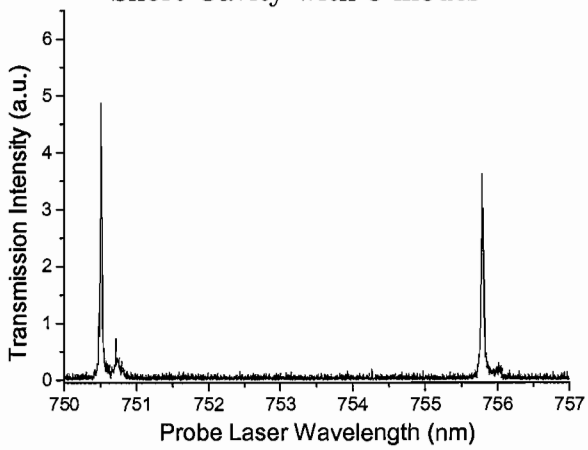

Short Cavity with 2 modes

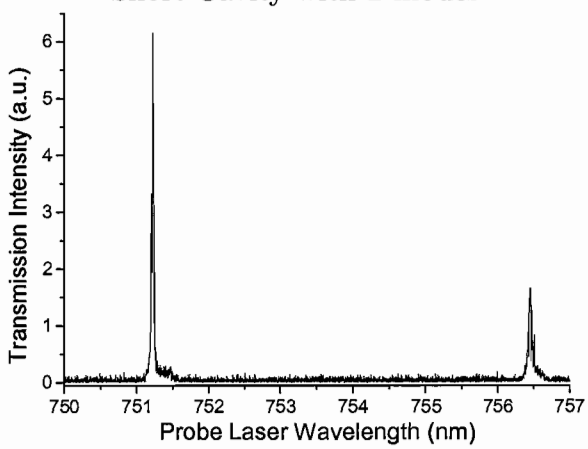

Hemispherical Limit

FIGURE 3.22: 60 μm hemispherical cavity transmission spectra with QDs at 16.6 K. The cavity finesse is about 260 and the FWHM of the HG00 modes is about 10 GHz.

The cavity mode-QD coupling strength is proportional to the amplitude of the normalized cavity mode at the location of the QD. In order to make the coupling very strong, it is necessary to localize highly the transverse extent of the mode function in the vicinity of the QD, and align the mode polarization vector with the dipole transition matrix element of the QD. Determining the precise degree to which this localization is possible is nontrivial, since the mode structure for such a small cavity is non-paraxial, is non-separable into polarization components, and is non-separable into longitudinal and transverse functions [97].

Our collaborators have taken two approaches to modeling the modes of the near-hemispherical micro-cavity. The two approaches are a fully numerical one—finite-difference-time-domain (FDTD) [152], and a hybrid analytic-numerical method [97]. The computations account fully for the distributed nature of the planar DBR mirror, an important aspect since plane waves of different incident angles undergo different phase shifts upon reflection there. The curved mirror is treated as a perfect reflector, an approximation expected to be adequate since the mode wave fronts are well matched to the mirror curvature. An example of the FDTD method, showing the calculated energy density of the mode versus position, is shown in Fig. 3.23. The QD

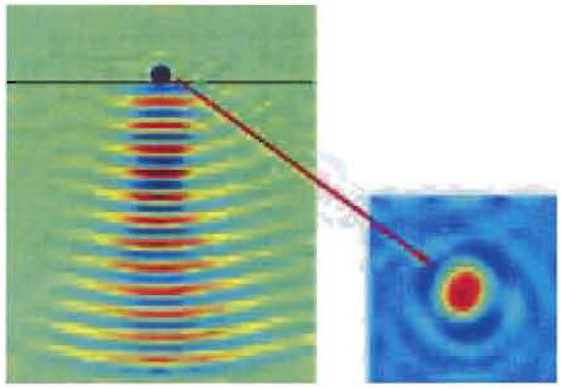

FIGURE 3.23: Numerical model for micro-cavity mode energy density, where the planar DBR structure is at the top and the curved mirror is in the lower half of the figure [151].

sits in a bright local maximum region in the first layer of the DBR. The calculations show that even in the presence of the DBR angle-dependent phase shifts, the mode waist in the non-paraxial regime is smaller than one wavelength.

An interesting result of the hybrid analytic-numerical method is a novel DBR-induced spin-orbit coupling of modes, which leads to small frequency splitting previously not identified [97]. The method also predicts a spatial splitting of the fundamental Gaussian mode (and other Gaussian modes) into a non-axis-symmetric inverted "V" shape.

3.4 Preliminary Spectroscopic Results and Potential Applications

In previous sections, we have characterized each component of the micro-cavity and tested the cavity as a whole. From the PL spectra in free space, we know certainly there are both spatially and spectrally isolated single QDs in the semiconductor DBR sample. And it is possible to find single QDs using a nano-scope in combination with a narrowband laser. We also learned from the cavity transmission spectra that the fundamental mode of the cavity is capable of spectrally resolving single QDs. In addition, numerical calculation predicts that the cavity mode waist in the non-paraxial regime is smaller than one wavelength. Now assume we are able to find a single QD. In order to make the coherent interaction between a single QD and a single cavity mode strong, which is through dipole coupling, we need to optimize three conditions: using a QD with large dipole moment, making the cavity mode volume small and locating the QD at an antinode of the cavity field with its dipole matrix element aligned with the mode polarizing direction. In this section, we address these issues in order to optimize the cavity-QD interaction. Through the preliminary spectroscopic results, we recognized the QDs polarizing direction, identified the spectral region of interest, and observed evidence of significant interaction between QDs and cavity modes.

3.4.1 Preliminary Spectroscopic Results

The dipole transition moments of the QDs can be obtained through fitting the linear absorption data from single QD states. Based on the studies carried out in this kind of IFQDs by our collaborators and from others, we know that the dipole matrix elements of these IFQDs range from 50-100 Debye [153, 117], which is large enough and suitable for studying cavity-QED strong coupling and is one of the reasons that we chose them for this purpose. Based on our DBR mirror (CAT96) design, the QDs are grown in the middle of a one-wavelength $Al_{0.24}Ga_{0.26}As$ spacer layer. For a laser resonating with the spacer layer, this automatically puts them at an antinode of the cavity field. So the tasks left for us now are to find a single QD, align the polarization of a probe laser to be parallel with its dipole matrix element and make the beam spot at the QDs location as small as possible and hence minimize the effective cavity mode volume. Let's start with PL spectra, which is now filtered by the cavity and is compared with that in free space.

As shown in Sec. 3.2.3, based on nano-scope PL spectra measured in free space at 7 K, there are both spatially and spectrally isolated single QDs at certain locations on the sample. However, it is not easy to isolate a single QD spatially alone, which requires a spatial resolution better than 600 nm, as shown in Fig. 3.13. For our micro-cavity operating near hemispherical limit, the beam waist is typically 1 μm for the fundamental mode at the planar mirror. For the worst scenario estimate, there can be as many as 400 QDs within the beam spot assuming that QDs have nominal lateral sizes 50 nm and are closely packed. So we need to combine the spectral selection ability in order to address single QDs.

In experiment, an excitation laser beam having a wavelength 658 nm is coupled co-linearly with the probe laser beam into the micro-cavity from the curved-mirror side, and the QDs in the DBR mirror at the other side of the cavity are excited. PL signals are collected by an aspherical lens (NA=0.65) after the DBR mirror and are recorded by a spectrometer. Figure 3.24 shows four PL spectra at one specific

location on the sample taken at 17 K. The PL emission (envelope) is in the 750-770 nm wavelength region and is consistent with the PL measurement taken by UA group, as shown in Fig. 3.12(a), but is now filtered by the cavity. The PL data are taken with the cavity operating near hemispherical limit, where the beam spot is close to minimum. The wavelength spacing between the peaks are about 2.2 nm, which is roughly half of a cavity FSR. The three strongest modes separated about 4.4 nm in the central part of the spectra are nearly degenerate even-order modes, while nearly degenerate odd-order modes are in between them alternatively. This effect is very clear in wavelength range 757.5-768.0 nm because this region is where our cavity has higher finesse and is where the cavity effect is manifested.

By scanning the DBR mirror in the x-y plane, we are able to map out the regions where there are fewer QDs indicating by weaker PL signals. Furthermore, we want to probe the red tail of the PL spectra where presumably there are even fewer QDs, giving higher chance to address single QDs spectrally. The other important information we can obtain from PL is that we can find out the polarization orientation of the QDs after they were incorporated with the cavity, which is now inside the vacuum chamber. We know from STM image of the GaAs QW where IFQDs are formed as shown in Fig. 2.7, that they tend to elongate along the crystal $[\bar{1}10]$ axis and hence are maximally polarized in this direction. But we do not know in which physical direction they are maximally polarized, particularly after putting the sample inside the vacuum chamber. By putting a polarizer in the optical path before sending the PL signal into the spectrometer, we are able to recognize the direction in which the PL signal is maximized by changing the angles of the polarizer in the transverse plane, as shown in Fig. 3.24. The PL spectrum with maximum intensity is designated as the QDs' polarizing direction and the angle of the polarizer is thus defined as 0^0. The one with minimum intensity is with the polarizer angle changed $\pm 90^0$ from the 0^0 angle position. The other two in between correspond to $\pm 30^0$ and $\pm 60^0$ angle changes from the 0^0 position, respectively.

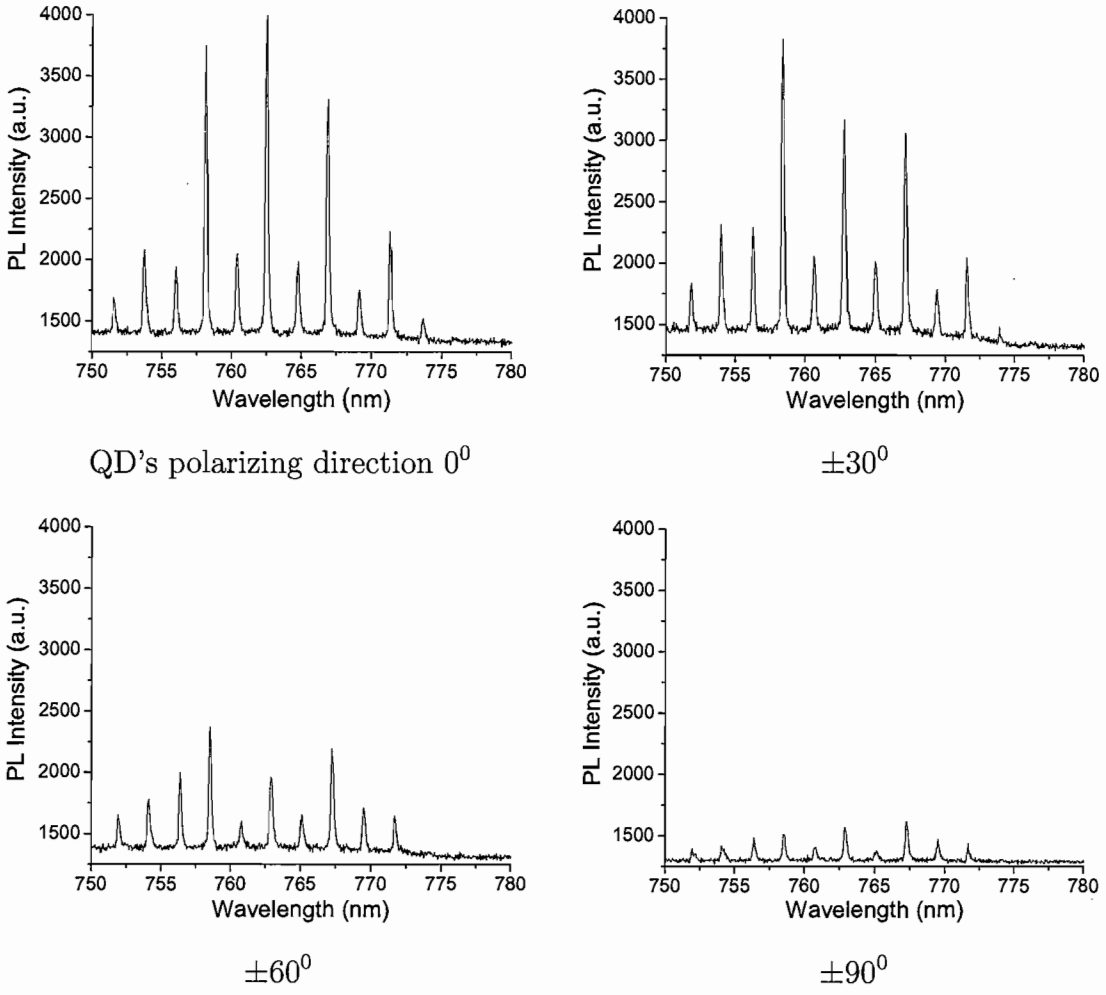

FIGURE 3.24: Four PL spectra showing the polarizing direction (0^0) of the GaAs IFQDs. The excitation laser has a wavelength 658 nm with a power 318 μW before entering the UHV chamber, which is coupled co-linearly with the probe laser into the micro-cavity.

Once we know the polarization of the QDs, we couple a spectroscopic laser at this polarization into the cavity to probe the interaction between the QDs and a cavity mode. We operate the cavity near hemispherical limit, where the beam spot is close to the diffraction limit, yielding a one-micron spot size. We first stabilize the cavity length through a feedback control loop and lock it with a reference laser beam at a specific wavelength that is monitored and calibrated by a wavelength meter; then we scan the probe laser's wavelength and measure the spectrum. By adjusting the reference laser wavelength step by step, we are able to tune a cavity resonance through a QD (or QDs) at a specific absorbing wavelength. Figure 3.25 shows eight transmission scans obtained in this way. The four traces (a)-(d) are with the reference laser wavelength at 785.72 nm, 785.75 nm, 785.77 nm and 785.80 nm, respectively. At this wavelength, 0.01 nm wavelength step corresponds to 4.86 GHz frequency step. The four traces (e)-(h) correspond to the reference laser with wavelength at 785.81 nm, 785.82 nm, 785.83 nm and 785.85 nm respectively.

The two strongest modes in the transmission in Fig. 3.25(a) are HG00 or LG00 modes and are separated by one cavity free spectral range (FSR), which is 5.0 nm in wavelength, corresponding to 2.6 GHz in frequency. The small hump at half FSR in between the two HG00 modes is the group of nearly degenerate odd-order modes. The weaker hump adjacent to the HG00 mode is either the broadened HG02 (HG11) mode or few closely clustered higher order even modes. From these data, we can deduce that the cavity length in this case is 57.7 μm. The maximum cavity finesse for the HG00 mode is 79, giving a linewidth about 0.06 nm (33 GHz). The wavelength step for taking the data is 0.01-0.03 nm increasing, equivalently with a frequency step 4.86-14.6 GHz at the reference wavelength 785.8 nm.

One can see that the HG00 mode initially at 759.40 nm becomes weaker and weaker as we tune the cavity resonance through the wavelength 759.43 nm, as indicated by the dashed arrow line. We believe that there is a strong absorption at the wavelength 759.43 nm. It could be either a single QD or a few inhomogeneously

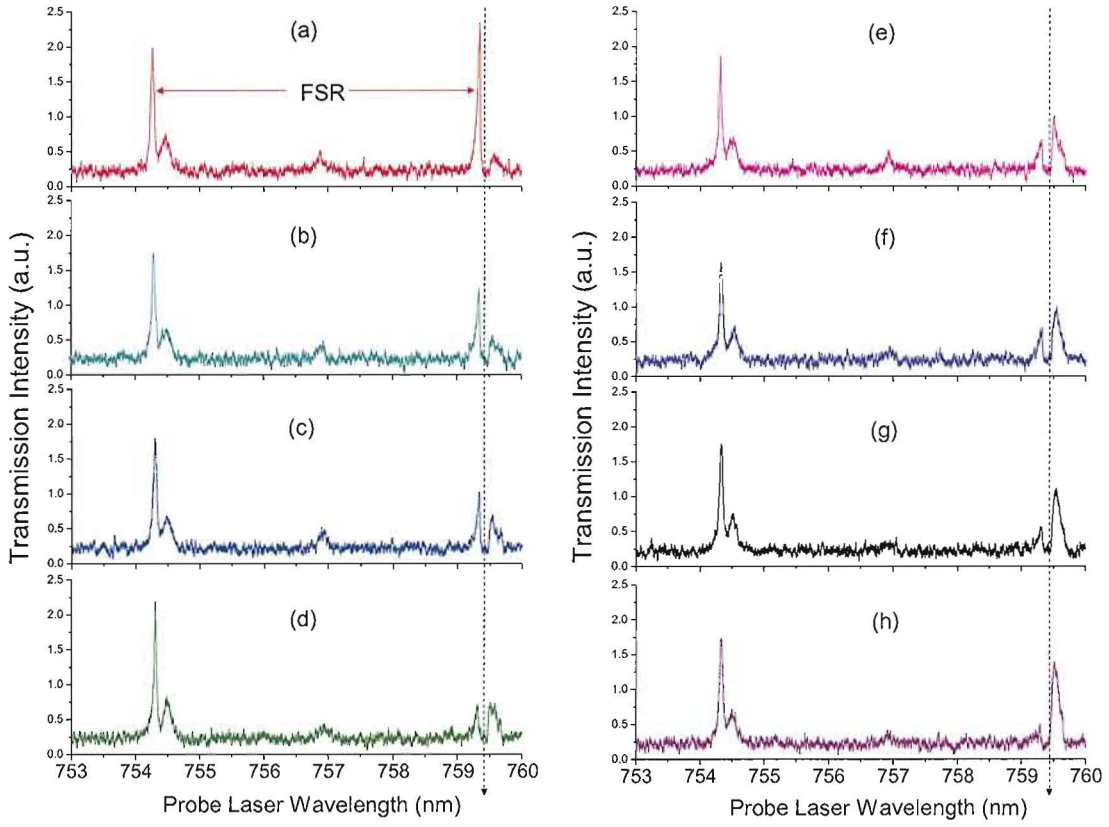

FIGURE 3.25: Eight transmission scans of the composite cavity-QD system by tuning the cavity length or cavity resonance through QDs resonance.

broadened QDs lying within the cavity linewidth. We cannot discriminate these two cases at this moment. Please note that the modes one FSR away around 754.2 nm are not affected by the wavelength tuning. We think there is no noticeable absorption happening (no QD resonance) there and therefore use it as a reference. The other interesting phenomenon that needs pointing out is that the higher-order mode (modes) around 759.50 nm becomes stronger and stronger as the adjacent HG00 mode gets absorbed. One possible explanation is that the photons on the blue side of the spectra get absorbed and re-emitted into the red side of the spectra at 759.5 nm which is in resonance with the cavity mode.

According to the PL spectra inside the cavity shown in Fig. 3.24, there are still a lot of QDs around the 759.0 nm wavelength region. It is not easy to address single QDs around there. There will be a better chance to address single QDs in the red side of the PL spectra while still being within the cavity stop-band in the vicinity of 765.0 nm, where presumably there are fewer QDs. Unfortunately, we do not have the right laser which can scan in 760.0-770.0 nm region in our lab at this moment. We are working to have the right laser to probe this spectral region. The other thing that needs mentioning is that we have scanned the x-y plane of the DBR mirror in a $50 \times 50\,\mu\text{m}^2$ region. We found that there are QDs almost everywhere. Without opening the UHV chamber and manually changing the sample lateral position by a few millimeter, we are not able to scan the x-y more than this to investigate other locations where potentially there are fewer QDs. So in the future, we want to move to other locations where there are fewer QDs and probe the cavity-QD interaction with the right laser. We believe we will have a better chance to address single QDs and study the strong interaction between single QDs and a single cavity mode, which in turn will enable us to apply this flexible external micro-cavity with integrated QDs in cavity QED and for efficient production of single photons.

3.4.2 Potential Applications

The hemispherical micro-cavity we have fabricated has an excellent prospect to achieve both strong coupling and efficient generation of single photons on demand. The hemispherical design is geometrically stable with the only loss (other than surface scatter) being by transmission through the end mirrors, not by diffraction losses as occurs in other micro-structures [154]. The use of a concave micro-mirror with high-reflectivity over a high-solid angle makes the mode waist size at the planar DBR diffraction limited and consequently leads to a large coupling strength. It enables a direct out-coupling of the spontaneously emitted single photons into a single-mode traveling wave, which is highly desirable for the efficient and on-demand single-photon generation. In addition, our system uses a cavity with adjustable length and a transversely movable focal region, allowing good spatial and spectral overlap of QD resonances with high-Q cavity modes. The preliminary spectroscopic results presented in the previous section are very promising. In the rest of this chapter, we give a brief discussion of two potential applications of this micro-cavity: cavity QED strong coupling and photons on demand.

Cavity-QED Strong Coupling

As stated in the earlier parts of this chapter, cavity-QED strong coupling occurs when the electric-dipole interaction frequency between an atom or QD and a single, unoccupied mode exceeds the energy decay rates of the composite system. The signature of strong coupling is a frequency splitting in the laser transmission spectrum approximately equal to twice the coupling constant, the so called normal-mode-splitting, which arises from the coherent interaction of two degenerate systems—the single QD and the single cavity mode. Such splitting can be viewed as a lifting of degeneracy. In the next chapter, we will examine this carefully and calculate the emission spectra, both into the useful forward direction and the open sides of the cavity, based on a single optical center interacting strongly with a single cavity mode in the Weisskopf-Wigner approximation.

IFQDs can have dipole matrix elements as large as 50-100 Debye [153, 117], yielding a vacuum Rabi splitting of 49-81 μeV, assuming a cavity waist of 1 micron and a cavity length of 60 microns. As required for strong coupling, this projected splitting would exceed the sum of the oscillator dissipation linewidth, typically 15 μeV, and the cavity dissipation linewidth, 8 μeV for a length of 50 microns and a reflectivity of 99.6%.

The transmission of an empty Fabry-Perot cavity has a series of single peaks with high transmission at each resonance, as shown in Fig. 3.22. In the strong-coupling regime, one of the peaks, preferably the HG00 mode, splits into two peaks, with a minimum located at the position of former peak. This shows a strong enhancement of system absorption at resonance. This interaction is suitable for coherent quantum engineering concepts, such as those being developed in attempts to achieve quantum-information processing [155, 156].

Photons on Demand

Another important application of such strongly coupled cavity-QD systems is the deterministic generation of single photons [92, 157, 93, 42] or of photon pairs on demand [158]. Such sources have wide applications in the emerging field of quantum information sciences [159]. This is particularly true for quantum cryptography, in which an essential element of secure quantum key distribution (QKD) is an optical source emitting a train of pulses that contain one and only one photon [160]. For example, a source having zero probability for generating two or more photons in a pulse and greater than 20% probability of generating one photon would lead to a great advance in QKD in daylight through the atmosphere [161, 162, 163]. A high quantum efficiency single-photon source will certainly make the QKD more secure. For other applications in quantum information processing such as in linear-optics quantum computing, one of the stringent requirements is a single-photon source with high efficiency ($> 99.9\%$). But the questions are: what is the quantum efficiency of a

single-photon source in the cavity-QED strong-coupling regime and how to optimize it? We will study these issues in Chapter V.

3.5 Summary

In this chapter, we first showed the state-of-the-art fabrication of a hemispherical micro-cavity that is comprised of a planar integrated semiconductor DBR mirror, and an external, concave micro-mirror. Then we characterized each component of the micro-cavity system: the concave micro-mirror and the semiconductor mirror with integrated QDs. We described different cases that can lead to modal mismatch of an input laser beam to the fundamental mode of the micro-cavity and used a simple afocal system to correct the mode mismatch. We tested the cavity transmission spectra at both room temperature and liquid helium temperature. We obtained preliminary spectroscopic results of cavity-filtered PL spectra and cavity transmission spectra showing evidence of significant cavity-QDs interaction at cryogenic temperature. At the end, we gave two examples of potential applications of this novel system operating in the cavity-QED strong-coupling regime. In the next two chapters we will show detailed calculations of the emission spectra and the quantum efficiency of single-photon sources in the cavity-QED strong-coupling regime respectively, in a more general way.

CHAPTER IV

THEORY OF SINGLE-PHOTON SOURCES IN THE CAVITY-QED STRONG-COUPLING REGIME

In Chapter III, we have discussed the design and the fabrication of a micro-cavity with semiconductor QDs as optical centers located at an antinode of a cavity field. It is believed that this system will find its applications in both cavity-QED studies and efficient production of single photons. In this chapter, we build a theoretical model for the interaction of a single optical center and a quantized single-mode field in a cavity and examine the claims made in the previous chapters. The state of the field that is generated in the process of emission from the cavity in which the photon is can be regarded as a single-photon wave-packet state. The composite system can be used as a single-photon source. In this chapter, we present the first calculation of the quantum efficiency and the spectra of single photons emitted both to the open sides and in the forward beam in the cavity-QED strong-coupling regime. All results are obtained in the Weisskopf-Wigner approximation for an impulse-excited optical center. Part of the work presented here has been published in Refs. [51, 52].

4.1 Introduction

In free space, an optical center interacts with a continuum of modes of a radiation field, the vacuum, and spontaneously emits photons to all 4π of solid angle of free space, as long as the conservation of energy and momentum is satisfied. The interaction is through electric dipole coupling. The coupling is characterized by a coupling constant g_0, which is often referred to as the Rabi frequency of the vacuum, is the frequency at which the optical center and the field exchanges energy, given that

there is only a single mode of the field. The photon emission rate, the probability of photon emission per unit time, is proportional to the square of the vacuum Rabi frequency g_0 and to the mode density. Assuming an optical center is excited to its excited state at time zero, the probability of finding an optical center is still in its excited state at time t obeys an exponential decay law, leading to an irreversible process. The source of irreversibility is the continuum of field modes resonantly coupled to the optical center. The vacuum field acts as a huge reservoir in which the phase information of the electric dipole is lost.

When an optical center is placed inside a two-mirror cavity, it will interact with an altered vacuum, where the density of states is structured due to the boundary conditions imposed on the region enclosed by the cavity mirrors. If the cavity mirrors are not able to cover all solid angle, the optical center inside the cavity can still spontaneously emit photons into the open sides of the cavity which acts as a reservoir, leading to dissipation. How an optical center inside the cavity behaves depends upon the ratio of the vacuum Rabi frequency g_0 to the cavity linewidth κ, whose inverse will be the density of modes "seen" by the optical center, or the lifetime of a photon in the cavity. If the ratio g_0/κ is smaller the one, the spontaneously emitted photon is dissipated rapidly and an optical center behaves much as it does in free space but at an enhanced rate if it is resonant with the cavity. The emission may also be inhibited if the optical center is not in resonance with any cavity mode.

However, if the ratio g_0/κ is larger than one and the coupling between the optical center and a cavity mode is stronger than its coupling to side modes, new behavior takes place: a radiated photon can stay in the cavity so long that it has a high probability to be re-absorbed by the optical center before it dissipates. Spontaneous emission becomes reversible and oscillating, as the optical center and field exchanges energy at a rate g_0. Such behavior is well known for the interaction of an atom with a classical monochromatic field and is called "Rabi oscillation" in optical transient experiments [164]. In cavity QED we are discussing here, however, the optical center

couples to its own one-photon field without an external applied field. This effect is called "vacuum Rabi oscillation".

In this chapter, we discuss the coherent interaction of a quantized radiation field inside a cavity with a two-level optical center described by a Hamiltonian in the dipole and the rotating-wave approximations. This problem was studied as early as in 1963 by Edwin T. Jaynes and Frederick W. Cummings [165] for an ideal lossless system. For a single-mode field it reduces to a relatively simple form yet still gives a lot illuminating results in the cavity QED and quantum optics. In our calculations presented here, we include dissipations, such as losses to the open sides of a cavity and emission into the forward direction of a cavity, to model realistic experiments. Perhaps most importantly, the results can be tested experimentally through the recently spectacular advances in the development of various high-Q micro-cavities already discussed in Chapter I.

Based on the solutions of the probability amplitudes using Weisskopf-Wigner theory [166], we first examine the widely cited Purcell effect in the cavity-QED weak-coupling regime. Then we derive the vacuum Rabi oscillations, or normal mode oscillations in the cavity-QED strong-coupling regime in Sec. 4.2. We define and calculate the integrated-pulse quantum efficiency of a single-photon source in this regime in Sec. 4.3. Then we generalize the definition of the Wiener-Khintchine spectrum for a stationary and ergodic process to a non-stationary process appropriate in this case, and derive the analytical formulas for the cavity-modified forward emission and side emission spectra of single photons emitted from a cavity in Sec. 4.4.

4.2 Probability Amplitude Method—Weisskopf-Wigner Theory

Our model system consists of a two-level optical center, an atom or QD, located at an antinode of the field in an optical microcavity with a length L. Damping plays an

important role in this model. These include the decay of an atom/QD in an excited state to the lower (ground) state and the decay of the radiation field inside a cavity with partially transparent mirrors. In general, damping of a system is described by its interaction with a reservoir with a large number of degrees of freedom, which can be represented by an infinite number of harmonic oscillators, as in Fig. 4.1. M_1 is a perfect 100%-reflecting mirror and M_2 is a partially transparent one, from which a sequence of single photons emerges.

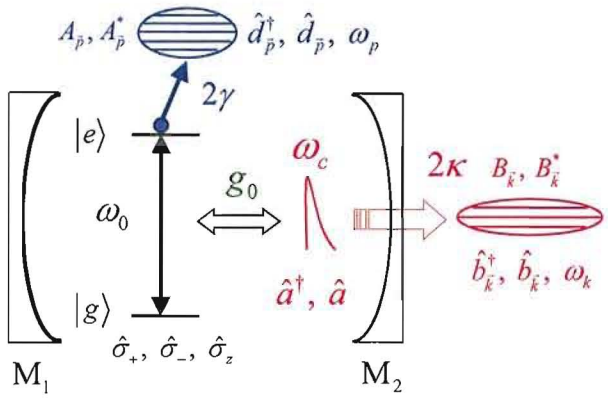

FIGURE 4.1: Analytical model for a lossy two-level optical center interacting with a single mode in a leaky optical cavity. g_0 is the vacuum Rabi frequency. 2γ and 2κ are the optical center population decay rate to the sides and the cavity field decay rate to the forward direction, respectively.

The coupling constant or the vacuum Rabi frequency g_0 has been introduced in Chapter II, given by

$$g_0 = \mu_x \sqrt{\frac{\omega_c}{2\hbar\varepsilon_0 V_{eff}}}, \tag{4.1}$$

where μ_x is the dipole matrix element of either atomic or excitonic transition in the electric field direction $\hat{x}$ having frequency ω_0. ω_c is the frequency of the cavity mode of interest. V_{eff} is the effective cavity mode volume, defined in Eq. (2.5). The coupling between either the optical center or the cavity field to their respective reservoirs R_s and R_f can be the decay of the excited-state population associated with all processes

(radiative recombination and nonradiative relaxations) except emission into the single cavity mode of interest in the case of optical center or simple cavity damping in the case of field. In both cases, the net result is to dampen the mode of interest, in which the single photons are. We model these dampings by linear interaction terms in the Hamiltonian. The coupling constants between the two-level optical center, a single photon and their respective reservoir fields are $A_{\vec{p}}$, $A^*_{\vec{p}}$ and $B_{\vec{k}}$, $B^*_{\vec{k}}$.

The total Hamiltonian $\hat{H}$ for this system in the Schrödinger picture in the dipole approximation and the rotating wave approximation (RWA) is well-known [167]

$$\hat{H} = \hat{H}_0 + \hat{H}_I, \tag{4.2}$$

where

$$\hat{H}_0 = \hbar\omega_0 \frac{\hat{\sigma}_z}{2} + \hbar\omega_c \hat{a}^\dagger \hat{a} + \hbar \sum_{\vec{p}} \omega_p \hat{d}^\dagger_{\vec{p}} \hat{d}_{\vec{p}} + \hbar \sum_{\vec{k}} \omega_k \hat{b}^\dagger_{\vec{k}} \hat{b}_{\vec{k}} \tag{4.3}$$

$$\hat{H}_I = \hbar g_0 \left(\hat{\sigma}_+ \hat{a} + \hat{\sigma}_- \hat{a}^\dagger\right) + \hbar \sum_{\vec{p}} \left(A^*_{\vec{p}} \hat{\sigma}_- \hat{d}^\dagger_{\vec{p}} + \text{H.c.}\right) + \hbar \sum_{\vec{k}} \left(B^*_{\vec{k}} \hat{a} \hat{b}^\dagger_{\vec{k}} + \text{H.c.}\right). \tag{4.4}$$

$\hat{H}_0$ consists of the energies of the two-level optical center (atom or QD), the single-mode field of the cavity, both the side reservoir modes and the free field reservoir modes. $\hat{H}_I$ is the interaction energy and takes form of a sum of the atom-cavity interaction, atom-reservoir and field-reservoir interaction terms. The operators $\hat{a}$ and $\hat{a}^\dagger$ are the annihilation and creation operators for the single mode of the cavity under consideration, while $\hat{\sigma}_z$ and $\hat{\sigma}_\pm$ are the Pauli operators for the atomic (Fermionic QD) inversion, raising, and lowering, respectively. ω_0 and ω_c are the atomic and cavity resonance frequencies. Here we assume that both reservoirs consist of many Bosonic oscillators (e.g. phonons, other photon modes etc.) with closely spaced frequencies ω_p and ω_k, annihilation and creation operators $\hat{d}_{\vec{p}}$, $\hat{b}_{\vec{k}}$, $\hat{d}^\dagger_{\vec{p}}$, $\hat{b}^\dagger_{\vec{k}}$, respectively.

It is convenient to work in the interaction picture, in which the Hamiltonian $\hat{V}(t)$ is obtained by an unitary transformation of the Hamiltonian $\hat{H}$ in the Schrödinger picture

$$\hat{V}(t) = e^{i\hat{H}_0 t/\hbar} \hat{H} e^{-i\hat{H}_0 t/\hbar}. \tag{4.5}$$

For two operators $\hat{A}$ and $\hat{B}$ that do not necessarily commute, the operator expansion theorem says $e^{\alpha\hat{A}}\hat{B}e^{-\alpha\hat{A}} = \hat{B} + \alpha[\hat{A},\hat{B}] + \frac{\alpha^2}{2}[\hat{A},[\hat{A},\hat{B}]] + ...$, where α is a c-number. It can be readily seen that the interaction Hamiltonian $\hat{V}(t)$ in the interaction picture for this system in the dipole approximation and the RWA is [167]

$$\begin{aligned}\hat{V}(t) =& \hbar g_0 \left(\hat{\sigma}_+ \hat{a} e^{i\Delta t} + \text{H.c.}\right) \\ &+ \hbar \sum_{\vec{p}} \left(A^*_{\vec{p}} \hat{\sigma}_- \hat{d}^\dagger_{\vec{p}} e^{i\delta_p t} + \text{H.c.}\right) \\ &+ \hbar \sum_{\vec{k}} \left(B^*_{\vec{k}} \hat{a} \hat{b}^\dagger_{\vec{k}} e^{i\delta_k t} + \text{H.c.}\right),\end{aligned} \tag{4.6}$$

where $\Delta = \omega_0 - \omega_c$, $\delta_p = \omega_p - \omega_0$, and $\delta_k = \omega_k - \omega_c$ are the detunings of the optical center-cavity, optical center-reservoir, and cavity-reservoir. Here we treat the atomic or excitonic transition frequency ω_0 as constant. Later in the next chapter we allow it to fluctuate, to model pure dephasing.

Given that there is only one excitation in the system and the optical center is excited to its excited state at time $t = 0$, then at any time t, the state vector is a linear superposition of the states $|e,0\rangle$, $|g,0\rangle$ and side- and forward-reservoir modes. The state vector is therefore

$$\begin{aligned}|\psi(t)\rangle =& E(t)|e,0\rangle|0\rangle_{R_s}|0\rangle_{R_f} + C(t)|g,1\rangle|0\rangle_{R_s}|0\rangle_{R_f} \\ &+ \sum_{\vec{p}} S_{\vec{p}}(t)|g,0\rangle|1_{\vec{p}}\rangle_{R_s}|0\rangle_{R_f} \\ &+ \sum_{\vec{k}} O_{\vec{k}}(t)|g,0\rangle|0\rangle_{R_s}|1_{\vec{k}}\rangle_{R_f}\end{aligned} \tag{4.7}$$

Here $|e,0\rangle$ is the state in which the optical center is in the excited state and the cavity field has zero photon. A similar description exists for $|g,0\rangle$. However, due to the side and forward reservoirs, a photon can also be lost to the open sides or emitted to the forward direction of the cavity. $|j_{\vec{p}}\rangle_{R_s}|l_{\vec{k}}\rangle_{R_f}$ $(j,l = 0,1)$ corresponds to j photons in the $\vec{p}$ mode (other than the privileged cavity mode) of the side reservoir R_s and l photons in a single-mode $(\vec{k})$ traveling wave of the one-dimensional photon reservoir

R_f in the forward direction of the cavity. $E(t)$, $C(t)$, $S_{\vec{p}}(t)$, and $O_{\vec{k}}(t)$ are the slowly varying probability amplitudes, as we are using interaction picture.

The equations of motion for the probability amplitudes are obtained by substituting $|\psi(t)\rangle$ and $\hat{V}(t)$ into the Schrödinger equation in the interaction picture

$$i\hbar\frac{\partial}{\partial t}|\psi(t)\rangle = \hat{V}(t)|\psi(t)\rangle, \tag{4.8}$$

and then projecting the resulting equations onto different bra states respectively. We then obtain

$$\dot{E}(t) = -ig_0 e^{i\Delta t}C(t) - i\sum_{\vec{p}} A_{\vec{p}} e^{-i\delta_p t} S_{\vec{p}}(t), \tag{4.9}$$

$$\dot{C}(t) = -ig_0 e^{-i\Delta t}E(t) - i\sum_{\vec{k}} B_{\vec{k}} e^{-i\delta_k t} O_{\vec{k}}(t), \tag{4.10}$$

$$\dot{S}_{\vec{p}}(t) = -iA^*_{\vec{p}} e^{i\delta_p t}E(t), \tag{4.11}$$

$$\dot{O}_{\vec{k}}(t) = -iB^*_{\vec{k}} e^{i\delta_k t}C(t), \tag{4.12}$$

where dots indicate time derivatives. In this context, we assume the optical center is prepared in an excited state $E(0) = 1$, $C(0) = 0$ at time $t_0 = 0$ (more generally, it can be prepared in an arbitrary single-quantum state), and there is no photon elsewhere. By first integrating Eqs. (4.11) and (4.12), then substituting them into Eqs. (4.9) and (4.10) we obtain

$$\dot{E}(t) = -ig_0 e^{i\Delta t}C(t) - \sum_{\vec{p}} |A_{\vec{p}}|^2 \int_0^t dt'' e^{-i\delta_p(t-t'')}E(t''), \tag{4.13}$$

$$\dot{C}(t) = -ig_0 e^{-i\Delta t}E(t) - \sum_{\vec{k}} |B_{\vec{k}}|^2 \int_0^t dt' e^{-i\delta_k(t-t')}C(t'). \tag{4.14}$$

These are non-perturbative equations. We have replaced four linear differential equations by two linear differential-integral equations. In order to solve these coupled equations, we have to make approximations and we do so using Weisskopf-Wigner theory [166, 167].

Since the side reservoir modes are closely spaced in frequency, we first replace the summation over the wave vector $\vec{p}$ in Eq. (4.13) by an integral:

$$\sum_{\vec{p}} \rightarrow \frac{2V_{R_s}}{(2\pi)^3}\int_{4\pi-\Omega_c} d\Omega \int_0^\infty dpp^2 = \frac{2V_{R_s}}{(2\pi c)^3}\int_{4\pi-\Omega_c} d\Omega \int_0^\infty d\omega_p {\omega_p}^2, \tag{4.15}$$

where V_{R_s} is the quantization volume of the side reservoir R_s, Ω_c is the solid angle covered by the cavity and p is the amplitude of the wave vector $|\vec{p}|$, given by ω_p/c. Eq. (4.13) becomes

$$\begin{aligned}\dot{E}(t) = &- ig_0 e^{i\Delta t}C(t) \\ &- \frac{2V_{R_s}}{(2\pi c)^3}\int_{4\pi-\Omega_c} d\Omega \int_0^\infty d\omega_p {\omega_p}^2 |A(\omega_p)|^2 \int_0^t dt'' e^{-i\delta_p(t-t'')}E(t'').\end{aligned} \tag{4.16}$$

In the emission spectrum, the intensity of light associated with the emitted radiation is going to be centered about the atomic or excitonic transition frequency ω_0. The frequency ω_p^2 and $|A(\omega_p)|^2$ vary little around $\omega_p = \omega_0$ for which the time integral in Eq. (4.16) is not negligible. We can therefore replace ω_p^2 by ω_0^2 and $|A(\omega_p)|^2$ by $|A(\omega_0)|^2$ and the lower limit in the ω_p integration by $-\infty$. Using the definition for the delta function

$$\int_{-\infty}^{\infty} d\omega_p e^{-i(\omega_p-\omega_0)(t-t'')} = 2\pi\delta(t-t''), \tag{4.17}$$

we obtain the following equation for $E(t)$, in the WWA

$$\dot{E}(t) \;=\; -ig_0 e^{i\Delta t}C(t) - \gamma E(t), \tag{4.18}$$

where $2\gamma \equiv [V_{R_s}/(4\pi^2 c^3)]\int_{4\pi-\Omega_c} d\Omega\omega_0^2|A(\omega_0)|^2$ is the atomic population decay rate into the modes other than the cavity mode, and can be given approximately by $2\gamma \approx 2\gamma_0(1-\Omega_c/4\pi)$, with $2\gamma_0$ being the free-space spontaneous emission rate, if Ω_c is small compared with 4π.

However, for the photons escaping from the cavity, they are going to be in a one-dimensional traveling-mode (continuous-mode) state propagating in the forward direction from the cavity. It is advantageous to take the limit of a quantization axis of

infinite extent parallel to the cavity axis ($\hat{z}$) but to retain a finite cross-sectional area perpendicular to the axis. Then the one-dimensional continuous-mode variable can be taken equivalently as the wavevectors $\vec{k} = \pm(\omega_k/c)\hat{z}$ or the frequency $\omega_k = c|\vec{k}|$. The one-dimensional mode spacing is thus $2\pi c/L$, which is just the inverse of the density of states for the one-dimensional photon reservoir $D(\omega_c) = L/2\pi c$ [168]. Similarly we obtain the equation for $C(t)$ in the WWA

$$\dot{C}(t) = -ig_0 e^{-i\Delta t}E(t) - \kappa C(t), \tag{4.19}$$

where $\kappa \equiv \pi D(\omega_c)|B(\omega_c)|^2$ [168], is one-half the decay rate of the intracavity field. The solutions to $S_{\vec{p}}(t)$ and $O_{\vec{k}}(t)$ are straightforward once we can solve $E(t)$ and $C(t)$, by integrating Eqs. (4.11) and (4.12). To summarize, we have the following results:

$$\dot{E}(t) = -ig_0 e^{i\Delta t}C(t) - \gamma E(t), \tag{4.20}$$

$$\dot{C}(t) = -ig_0 e^{-i\Delta t}E(t) - \kappa C(t), \tag{4.21}$$

$$S_{\vec{p}}(t) = -iA^*_{\vec{p}}\int_0^t dt'' e^{i\delta_p t''}E(t''), \tag{4.22}$$

$$O_{\vec{k}}(t) = -iB^*_{\vec{k}}\int_0^t dt' e^{i\delta_k t'}C(t'), \tag{4.23}$$

where γ and κ are one-half the radiative decay rates of the atomic population (other than the privileged cavity mode) and the intracavity field, respectively. The general solutions to the coupled differential Eqs. (4.20) and (4.21) are

$$\begin{pmatrix} E(t) \\ C(t) \end{pmatrix} = e^{-Kt/2}\begin{pmatrix} e^{i\Delta t/2} & 0 \\ 0 & e^{-i\Delta t/2} \end{pmatrix} \times \left[e^{i\lambda t}\begin{pmatrix} \frac{1}{2} - \frac{\Delta + i\Gamma}{4\lambda} & -\frac{g_0}{2\lambda} \\ -\frac{g_0}{2\lambda} & \frac{1}{2} + \frac{\Delta + i\Gamma}{4\lambda} \end{pmatrix} + e^{-i\lambda t}\begin{pmatrix} \frac{1}{2} + \frac{\Delta + i\Gamma}{4\lambda} & \frac{g_0}{2\lambda} \\ \frac{g_0}{2\lambda} & \frac{1}{2} - \frac{\Delta + i\Gamma}{4\lambda} \end{pmatrix} \right] \times \begin{pmatrix} E(0) \\ C(0) \end{pmatrix}, \tag{4.24}$$

where $K \equiv \kappa + \gamma$, $\Gamma \equiv \kappa - \gamma$, and $\lambda = \sqrt{g_0^2 - [(\Gamma - i\Delta)/2]^2}$.

4.2.1 Cavity-QED Weak Coupling

As we have claimed in Chapter II, in the cavity-QED weak-coupling regime, the main role of the cavity is to control the spontaneous emission through the Purcell effect to enhance radiative decay into a cavity mode of interest. Now we can examine the claim based on the results obtained above. Let's consider the case when the optical center is in resonance with a cavity mode, $\Delta = \omega_0 - \omega_c = 0$. The cavity-QED weak-coupling regime is defined by $(\kappa - \gamma)^2 > g_0^2$ so that the complex frequency λ is purely imaginary and equals $i\sqrt{(\Gamma/2)^2 - g_0^2}$. For convenience, define $\lambda \equiv i\lambda_0$ with λ_0 is purely real. The solutions to the probability amplitudes simplify to

$$\begin{pmatrix} E(t) \\ C(t) \end{pmatrix} = e^{-Kt/2} \times \left[e^{-\lambda_0 t} \begin{pmatrix} \frac{1}{2} - \frac{\Gamma}{4\lambda_0} & -\frac{g_0}{i2\lambda_0} \\ -\frac{g_0}{i2\lambda_0} & \frac{1}{2} + \frac{\Gamma}{4\lambda_0} \end{pmatrix} + e^{\lambda_0 t} \begin{pmatrix} \frac{1}{2} + \frac{\Gamma}{4\lambda_0} & \frac{g_0}{i2\lambda_0} \\ \frac{g_0}{i2\lambda_0} & \frac{1}{2} - \frac{\Gamma}{4\lambda_0} \end{pmatrix} \right] \begin{pmatrix} E(0) \\ C(0) \end{pmatrix}, \tag{4.25}$$

and the solutions subject to the initial condition, $E(0) = 1$ (atom in excited state), $C(0) = 0$ (cavity empty) at time $t_0 = 0$ are

$$E(t) = e^{-Kt/2} \left[\left(\frac{1}{2} - \frac{\Gamma}{4\lambda_0} \right) e^{-\lambda_0 t} + \left(\frac{1}{2} + \frac{\Gamma}{4\lambda_0} \right) e^{\lambda_0 t} \right], \tag{4.26}$$

$$C(t) = \frac{ig_0}{2\lambda_0} e^{-Kt/2} \left(e^{-\lambda_0 t} - e^{\lambda_0 t} \right). \tag{4.27}$$

For a low-Q cavity that subtends a large solid angle at the optical center so that the spontaneous emission to the sides is negligible, $\kappa \gg \gamma$, then in the cavity-QED weak coupling regime, we can approximate $(\Gamma/2)^2 \gg g_0^2$ as $\lambda_0 \approx \Gamma/2 - g_0^2/\Gamma$. We keep both terms of λ_0 in the exponential functions and only the first term in their coefficients. Then the probability amplitudes become, to first order in g_0/κ,

$$E(t) = e^{-\gamma\left[1 + g_0^2/(\kappa\gamma)\right]t}, \tag{4.28}$$

$$C(t) = -\frac{ig_0}{\kappa} \left\{ e^{-\gamma\left[1 + g_0^2/(\kappa\gamma)\right]t} - e^{-\kappa t} \right\}. \tag{4.29}$$

We know that in free space the atomic population decay obeys an exponential law with a decay rate $2\gamma_0$. With the cavity, based on the results given in Eqs. (4.28) and (4.28), we find that the atomic population now decays with an enhanced rate $\gamma' = \gamma\left[1 + g_0^2/(\kappa\gamma)\right]$, or

$$\frac{\gamma'}{\gamma} - 1 = \frac{g_0^2}{\kappa\gamma}. \tag{4.30}$$

The Purcell factor, widely referred to in the cavity-QED weak-coupling regime, is given in Ref. [87] by $F_p = (3\lambda^3/4\pi^2) \cdot (Q/V)$, which can be shown to be equal to $g_0^2/(\kappa\gamma_0)$. Therefore, we can readily see from Eq. (4.28) and the first term of Eq. (4.29) that the cavity indeed enhances both the spontaneous emissions to the sides and to the cavity mode by a factor that is exactly the Purcell factor F_p

$$\frac{\gamma' - \gamma}{\gamma_0} = F_p. \tag{4.31}$$

This justifies our claim made before. The Purcell factor is usually calculated based on Fermi's golden rule by comparing the density of modes in a cavity with that of in free space. Here we showed that it can be derived from solving the dynamics of the coupled system in the time domain. This has also been shown in Refs. [169, 170] by solving the equations of motion in Heisenberg picture. The other point we would like to point out is that the photon emission from the cavity now is dominated by the atomic spontaneous emission since the second term in Eq. (4.29) is much smaller than the first term, which results from the enhanced spontaneous emission.

Another case that is complementary to the above example is that when $\gamma \gg \kappa$, for a relatively high-Q cavity while the spontaneous emission to the sides is not negligible, $\gamma \approx \gamma_0$. Similarly one obtains the solutions to the probability amplitudes, to first order in g_0/γ as follows

$$E(t) = e^{-\gamma t} \tag{4.32}$$

$$C(t) = -\frac{ig_0}{\gamma}\left\{e^{-\kappa\left[1+g_0^2/(\kappa\gamma)\right]t} - e^{-\gamma t}\right\}. \tag{4.33}$$

In this case one would find that the spontaneous emissions into both the sides and the cavity are not affected, as seen from Eq. (4.32) and the second term in Eq. (4.33); but the photon emission from the cavity now is dominated by the cavity itself with an enhanced factor $g_0^2/(\kappa\gamma)$ that is almost exactly the Purcell factor $g_0^2/(\kappa\gamma_0)$. The enhanced cavity decay rate reflects the fact that the cavity Q is spoiled and the linewidth is broadened by an absorber inside the cavity, as also discussed in Ref. [170].

4.2.2 Cavity-QED Strong Coupling

In the cavity-QED strong-coupling regime, defined by $g_0 \gg \kappa, \gamma$, the real part of λ is much larger than its imaginary part. Then λ can be approximated as $\lambda \approx g \equiv \sqrt{g_0^2 + (\Delta/2)^2 - (\Gamma/2)^2}$, which is the generalized vacuum Rabi frequency. Note that for the case when the optical center and cavity are in resonance, $\Delta = \omega_0 - \omega_c = 0$, the complex frequency λ is purely real and equals $\sqrt{g_0^2 - (\Gamma/2)^2}$. This leads to sinusoidal oscillation rather than an exponential decay and will be justified below. The general solutions to the probability amplitudes in the cavity-QED strong-coupling regime are re-written as

$$\begin{pmatrix} E(t) \\ C(t) \end{pmatrix} = e^{-(K/2)t} \begin{pmatrix} e^{i\Delta t/2} & 0 \\ 0 & e^{-i\Delta t/2} \end{pmatrix} \times \begin{pmatrix} \cos(gt) + \dfrac{\Gamma - i\Delta}{2g}\sin(gt) & -i\dfrac{g_0}{g}\sin(gt) \\ -i\dfrac{g_0}{g}\sin(gt) & \cos(gt) - \dfrac{\Gamma - i\Delta}{2g}\sin(gt) \end{pmatrix} \begin{pmatrix} E(0) \\ C(0) \end{pmatrix}, \quad (4.34)$$

and the solutions subject to the same initial conditions used above are

$$E(t) = e^{-[(K-i\Delta)/2]t}\left[\cos(gt) + \frac{\Gamma - i\Delta}{2g}\sin(gt)\right] \quad (4.35)$$

$$C(t) = -\frac{ig_0}{g}e^{-[(K+i\Delta)/2]t}\sin(gt). \quad (4.36)$$

From a quick examination of these solutions, we can get a hint that the probabilities will undergo a number of oscillations before finally being damped away.

This is the so-called vacuum Rabi oscillations or the normal-mode oscillations and is a characteristic of the cavity-QED strong coupling. The normal-mode oscillations can be viewed either in the dressed-state picture or in the bare-state picture. Here we look at them in the bare-state picture where the oscillations are easier to calculate. The probability of finding the system in the excited atomic state is

$$\begin{aligned} P_e(t) =& |E(t)|^2 \\ =& \frac{e^{-Kt}}{2}\left[1+\frac{\Gamma^2+\Delta^2}{4g^2}+\left(1-\frac{\Gamma^2+\Delta^2}{4g^2}\right)\cos(2gt)+\frac{\Gamma}{g}\sin(2gt)\right], \end{aligned} \tag{4.37}$$

and the probability of finding the photon in the single cavity mode is

$$P_c(t) = |C(t)|^2 = \frac{g_0^2}{g^2}e^{-Kt}\sin^2(gt). \tag{4.38}$$

The strong interaction between an excited two-level optical center and a single cavity mode leads to single-quantum Rabi oscillation in the time domain or a frequency splitting in the frequency domain, the so-called normal-mode splitting, which arises from the coherent interaction of two degenerate systems—the single optical center and the single cavity mode. In this section, we discuss the normal-mode oscillations of such a system in the cavity-QED strong-coupling regime, while the emission spectra will be discussed in the next section. We first investigate the normal-mode oscillations by calculating the probabilities of finding the composite system in different states.

Consider the case when the optical center and cavity are in resonance, $\Delta = \omega_0 - \omega_c = 0$. Figure 4.2 shows plots of the two probabilities with both linear and logarithmic scales. The probabilities oscillate sinusoidally with an exponential decay envelope. However, they have opposite phases, which indicate the coherent oscillatory energy exchange between the excited optical center and the cavity field. And the envelope decay rate now is the sum of the spontaneous emission rate and the cavity decay rate, not just either of them; neither is the enhanced nor the suppressed spontaneous emission rate.

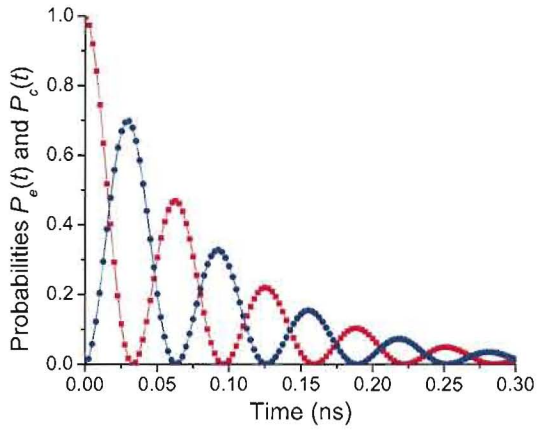

(a)

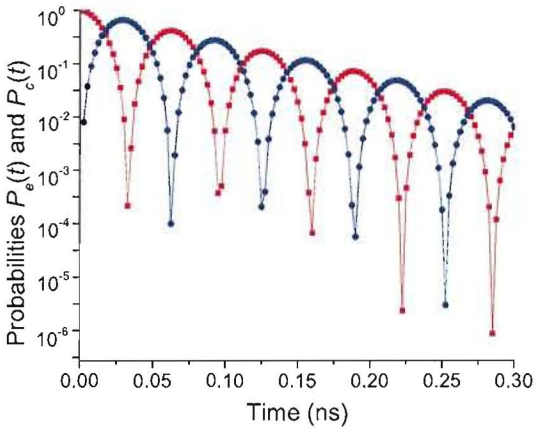

(b)

FIGURE 4.2: The probability of finding the optical center in its excited state and the probability of finding a photon in the single cavity mode, square and dot curves respectively: (a) linear scale, and (b) logarithmic scale, given $(g_0, \kappa, \gamma)/2\pi =$ (8.0, 1.6, 0.32) GHz.

4.3 Quantum Efficiency of a Single-photon Source in the Cavity-QED Strong-coupling Regime

The realizations of cavity-QED strong coupling in the atom-cavity [5] and QD-cavity systems [44, 45, 47, 48] allow researchers to deterministically generate single photons [93, 92, 42]. Single-atom lasers in the strong-coupling regime have also been studied [171]. A major question is what is the quantum efficiency (QE) of the emission from such systems. While not in the strong-coupling regime, Santori et al. [91] showed the ability to produce largely indistinguishable photons by a semiconductor QD in a micro-cavity using a large Purcell effect [87]. The QE of a single-photon source (SPS), which is intrinsic to the composite quantum system, can be different in these two regimes because the dynamics of the composite system is different, like we have shown in the previous section. The overall efficiency of SPS will also depend on the excitation efficiency [95], collection efficiency and detection efficiency, which are not intrinsic to the composite quantum system; however, they can be greatly affected by the energy structure of the optical center and the geometry of the cavity. Qualitative discussions of different efficiencies based on a particular system in the Purcell regime have been reported in the literature elsewhere [38]. In the following section, we define the quantum efficiency for a single-photon source in the cavity-QED strong-coupling regime, based on the theory developed in the previous sections and compare it with another definition defined by Law and Kimble that is often referred to [172].

4.3.1 Calculation of Quantum Efficiency

A single photon will certainly be emitted from the excited optical center, but it might not be coupled into a single-mode traveling wavepacket because it can also spontaneously decay to the side reservoir. We define the emission probability $P_o(t)$ to be the probability of finding a single photon in the output mode of the cavity between

the initial time $t_0 = 0$ and a later time t. This equals

$$P_o(t) = 2\kappa \int_0^t dt' \, |C(t')|^2 = \eta_q \left\{ 1 - e^{-Kt} \left[1 + \frac{K^2}{2g^2} \sin^2(gt) + \frac{K}{2g} \sin(2gt) \right] \right\}, \quad (4.39)$$

where

$$\eta_q \equiv \left[g_0^2/(g_0^2 + \kappa\gamma) \right] \left[\kappa/(\kappa + \gamma) \right], \quad (4.40)$$

given by the single-photon emission probability $P_o(t)$ in the sufficiently long-time limit $t \gg K^{-1}$. It may be decomposed as $\eta_q = \eta_c \cdot \eta_e$, with

$$\eta_c = \frac{g_0^2}{g_0^2 + \kappa\gamma} \equiv \frac{2C_0}{2C_0 + 1}, \quad (4.41)$$

$$\eta_e = \frac{\kappa}{\kappa + \gamma} \quad (4.42)$$

where $C_0 \equiv g_0^2/(2\kappa\gamma)$ is the cooperativity parameter per optical center [173].

We define η_q as the quantum efficiency of a SPS in the cavity-QED strong-coupling regime, which can be viewed as the product of the coupling efficiency (η_c) of the optical center to the cavity mode and the extraction efficiency (η_e) of the single photon into a single-mode traveling wavepacket. Despite extensive past study of this system, this general formula for quantum efficiency had not been published prior to our study [51]. The coupling efficiency characterizes how strong the optical center is coupled to the privileged cavity mode. The extraction efficiency determines how large the fraction of light is coupled to a single wave-packet, outward-traveling-wave mode. We emphasize that the cavity decay is not considered as a loss, but rather as a coherent out-coupling, because our goal is to extract single photons from the cavity.

The photon emission rate $n(t)$, defined as the time derivative of the emission probability, gives the rate of a single photon emerging from the cavity mirror M_2 and is

$$n(t) \equiv \frac{dP_0(t)}{dt} = 2\kappa \frac{g_0^2}{g^2} e^{-Kt} \sin^2(gt) \quad (4.43)$$

We expect the shape of $n(t)$ to be sufficiently narrow in time as to define a well-localized photon wavepacket and a well-specified time interval between successively emitted single photons.

From Eqs. (4.41) and (4.42), we can see that the larger the ratios $g_0^2/(\kappa\gamma)$ and κ/γ, the higher the coupling efficiency and the extraction efficiency, respectively. For a given optical center, with no pure dephasing, the dipole dephasing rate is limited by its population decay rate. However, we can design a cavity with a proper cavity decay rate κ to optimize the QE of a SPS and the shape of the photon-emission rate. Figure 4.3 shows plots of the emission probabilities and the emission rates for three (optimal, good and bad) cavity regimes where we varied the cavity decay rate, with $\kappa/2\pi$ = (8.0, 3.2, 16) GHz respectively, given realistic parameters $(g_0, \gamma)/2\pi$ = (8.0, 0.16) GHz in each case. We find that the optimal condition for a high QE and a temporally narrow emission rate, by optimizing the three parameters in Eq. (4.40), is $\kappa = g_0^2/\kappa \gg \gamma$, as shown by the dotted curves in Fig. 4.3. The QE is 96%, predicted by Eq. (4.40) in this example. The photon emission rate is well localized on the time axis. The width of $n(t)$ is about 32 ps.

4.3.2 Discussion of Quantum Efficiency

An earlier result obtained in the bad-cavity limit by Law and Kimble is given by [172],

$$P(t) \approx \frac{2C_1}{2C_1 + 1} \tag{4.44}$$

where $C_1 = g_0^2/(\kappa\gamma_1)$ is is the single-atom cooperativity parameter. Note that the γ_1 in definition Eq. (4.44) is the full width of the atomic absorption line. The cooperativity parameter defined in this context is $C_0 \equiv g_0^2/(2\kappa\gamma)$ because here γ is the half width, so these definitions are the same. Comparing our analytical result with that given by Eq. (4.44), we see that Eq. (4.44) is valid in the limit that spontaneous atomic decay is negligible, as treated in [172], or equivalently the extraction efficiency η_e is unity. This is not necessary for strong coupling and is also not implied by the strong-coupling condition. However, for deterministic production of single photons on demand, we not only require that the coupling of the optical center to the single cavity mode is far stronger than its coupling to all other modes ($g_0^2/\kappa \gg \gamma$), but also that there

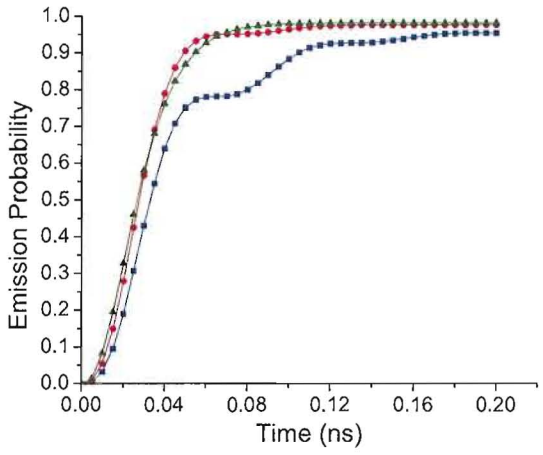

(a)

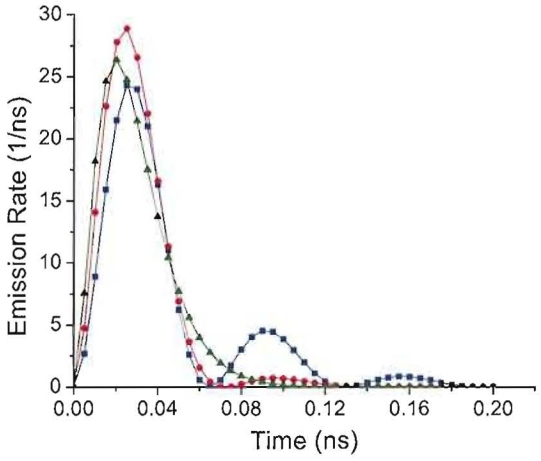

(b)

FIGURE 4.3: (a) The emission probability $P_o(t)$ of single photons, and (b) the emission rate $n(t)$, in three different cavity regimes: optimal cavity regime for $\kappa = g_0^2/\kappa \gg \gamma$, good cavity regime for $g_0^2/\kappa > \kappa \gg \gamma$, and bad cavity regime for $\kappa > g_0^2/\kappa \gg \gamma$, (dot, square and triangle, respectively).

needs to be almost no dephasing of the optical center during the emission process ($\gamma^{-1} \gg \kappa^{-1}$). This keeps the emission process deterministic and hence guarantees that the consecutively emitted photons are indistinguishable.

Using the definition of the Purcell factor, we can relate it to the cooperativity parameter C_0 by $F_p = g_0^2/(\kappa\gamma_0) \equiv 2C_0 \cdot f$, where $f \equiv \gamma/\gamma_0$ is the fraction of the spontaneous emission to the side modes and is often very close to one. So our result for QE can also be written as [51]

$$\eta_q = \frac{F_p}{F_p + f} \cdot \frac{\kappa}{\kappa + \gamma} = \beta \cdot \frac{\kappa}{\kappa + \gamma} \tag{4.45}$$

where $\beta \equiv F_p/(F_p+f)$ is called the spontaneous-emission coupling factor, the fraction of the light emitted by an optical center that is coupled into one particular mode [154, 174]. In Ref. [175], the authors discussed the coupling factor and the extraction efficiency in terms of the quality factor of the mode. The result Eq. (4.45) quantifies this discussion.

To conclude, our result for the QE of a SPS in the cavity-QED strong-coupling regime is more general than earlier results in [172, 175]. It can be used to estimate the QE of single photons deterministically generated in the cavity output in the cavity-QED strong-coupling regime [48], instead of using the Mandel-Q parameter [93]. One can improve the QE and performance of a SPS by optimizing the three parameters in the analytical result Eq. (4.40). The QE is crucial for a practical use of a SPS, for example, a high efficiency is required for implementing the linear-optics quantum computation schemes proposed by Knill et al. in [25]; while a low efficiency will severely limit the practical application of a SPS in quantum key distribution, as shown in [21].

4.4 Emission Spectra of a Single-photon Source in the Cavity-QED Strong-coupling Regime

It may seem strange to talk about the spectrum of a single-mode field since we normally associate a single mode with a single frequency. Here we are dealing,

however, with what should more correctly be called a quasimode, a mode defined in a leaky optical cavity, which therefore has a finite linewidth. For a stationary and ergodic process, the Wiener-Khintchine theorem [176] states that the spectrum is given by the Fourier transform of the two-time correlation function of the radiated field. In the strong-coupling regime and for an impulsive excitation of the system, however, this relation between the correlation function and spectrum fails because the coherent interaction overwhelms the relaxations here. There is no time t after which the correlation function depends only on the time difference. Thus the dipole correlation and the emitted field correlation cannot be stationary. We need to generalize the definition of the Wiener-Khintchine spectrum appropriate in this case.

We first introduce the forward emission, the emission of single photons through the cavity mirror into a single wave-packet, outward-traveling wave, and the side emission, the spontaneous emission of the excited optical center into the free-space other than the cavity (side modes or leak modes). We recognize from Eq. (4.23) that $O_{\vec{k}}(t)$ is proportional to the Fourier transform of the probability amplitude $C(t')$,

$$O_{\vec{k}}(t) = -iB_{\vec{k}}^{*} \int_{0}^{t} dt' e^{i(\omega_k - \omega_c)t'} C(t'). \tag{4.46}$$

We define the spectrum as the absolute value squared of the Fourier transform of the probability amplitude in the long-time limit, which is proportional to the Fourier transform of the convolution of the probability amplitude, as will be shown later. For simplicity, we consider the case that the atom/QD-cavity is in resonance. Therefore, the forward emission spectrum is given by

$$S_{f.e.}(\omega - \omega_c) = \lim_{t \to \infty} D(\omega_c) \left| O_{\omega}(t) \right|^2, \tag{4.47}$$

where we have changed the probability amplitude from $O_{\vec{k}}(t)$ to $O_{\omega}(t)$ by using the density of states for the one-dimensional photon reservoir $D(\omega_c) = L/2\pi c$. Using the solution to the probability amplitude $C(t)$ and the expression of $O_{\vec{k}}(t)$ in Eq. (4.46),

we can calculate the spectrum

$$\begin{aligned} S_{f.e.}(\omega-\omega_c) =& D(\omega_c)\,|B(\omega_c)|^2 \\ & \times \lim_{t\to\infty}\int_0^t dt' e^{i(\omega-\omega_c)t'}C(t')\int_0^t dt'' e^{-i(\omega-\omega_c)t''}C^*(t''). \end{aligned} \tag{4.48}$$

Then using the definition of the decay rate of the intracavity field $\kappa \equiv \pi D(\omega_c)|B(\omega_c)|^2$ [168] and defining a new variable $\Omega \equiv \omega - \omega_c$, the emission frequency centered at the cavity resonance ω_c, and $\tau \equiv t' - t''$, we obtain the forward emission spectrum

$$S_{f.e.}(\Omega) = 2\kappa\frac{1}{\pi}\mathrm{Re}\left\{\int_0^\infty d\tau e^{i\Omega\tau}\left[\int_0^\infty dt' C(t'+\tau)C^*(t')\right]\right\}. \tag{4.49}$$

The normalized forward emission spectrum is

$$s_{f.e.} = \left(2\kappa\int_0^\infty dt\,|C(t)|^2\right)^{-1} S_{f.e.}. \tag{4.50}$$

Similarly the side emission spectrum and the normalized side emission spectrum, in the long time limit, are given by

$$S_{s.e.}(\Omega) = 2\gamma\frac{1}{\pi}\mathrm{Re}\left\{\int_0^\infty d\tau e^{i\Omega\tau}\left[\int_0^\infty dt' E(t'+\tau)E^*(t')\right]\right\} \tag{4.51}$$

$$s_{s.e.} = \left(2\gamma\int_0^\infty dt\,|E(t)|^2\right)^{-1} S_{s.e.}. \tag{4.52}$$

In the long-time limit ($t \gg K^{-1}$), substituting the Eqs. (4.35) and (4.36) into Eqs. (4.51) and (4.49), we obtain the unnormalized emission spectra

$$S_{s.e.}(\Omega) = \frac{\gamma}{\pi}\left|\frac{\kappa - i(\Omega+\Delta)}{(K/2 - i\Delta/2 - i\Omega)^2 + g^2}\right|^2, \tag{4.53}$$

$$S_{f.e.}(\Omega) = \frac{\kappa}{\pi}\left|\frac{-ig_0}{(K/2 + i\Delta/2 - i\Omega)^2 + g^2}\right|^2. \tag{4.54}$$

The side emission spectrum here is the same as the spontaneous emission spectrum calculated alternatively by solving the master equation by Carmichael and others [177]. The forward emission spectrum is what we expect to measure by an ideal detection system at the output of the cavity in the forward direction, and has not been presented previously, to our knowledge. For zero atom-cavity detuning $\Delta = 0$, where

the atom and cavity resonances are degenerate, both the side emission and forward emission spectra show the normal-mode splittings, which however, are different. The splittings are $\Delta\omega_s = 2\sqrt{[g_0^4 + 2g_0^2\kappa(\kappa+\gamma)]^{1/2} - \kappa^2}$ for the side emission, and $\Delta\omega_f = 2\sqrt{g_0^2 - (\kappa^2+\gamma^2)/2}$ for the forward emission, as shown by the thicker curves in Figs. 4.4(a) and 4.4(b) respectively. Both are different from the generalized Rabi splitting $2g$.

Beyond the energy-splitting difference at zero atom-cavity detuning, it is also illuminating to investigate the dependence of the energy eigenvalue structure on the atom-cavity detuning. Shown in Fig. 4.4 are plots of the spectra, in the strong-coupling regime, for seven different values of atom-cavity detuning Δ. As $|\Delta|$ increases, the vacuum Rabi splitting also increases for both the side emission and forward emission spectra. At the same time, for the side emission spectra, the cavity-like peak features stronger emission and the atom-like peak grows smaller. For the forward emission spectra, however, both peaks show the same emission intensity.

4.5 Summary

In this chapter, we built a theoretical model for the interaction of a single two-level optical center and a quantized single-mode field in a cavity. Using Weisskopf-Wigner theory, we examined the Purcell effect when an optical center is weakly coupled to a cavity and derived the vacuum Rabi oscillations when the optical center is strongly coupled to a single mode of a cavity field. The state of the field that is generated in the process of emission from the cavity can be regarded as a single-photon wave-packet state and the composite system can be used as a single-photon source. We defined and calculated the integrated-pulse quantum efficiency for such a single-photon source in the cavity-QED strong-coupling regime. In the last section, we generalized the definition of the Wiener-Khintchine spectrum for a stationary and ergodic process to a non-stationary process appropriate in this case, and derived the analytical formula

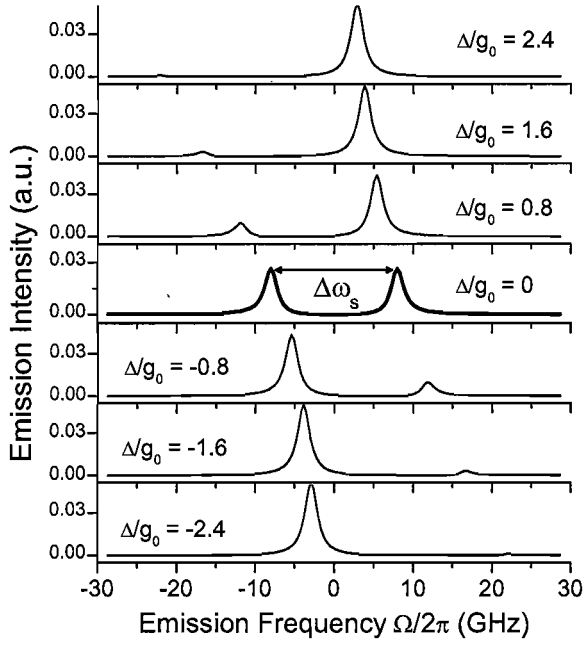

(a)

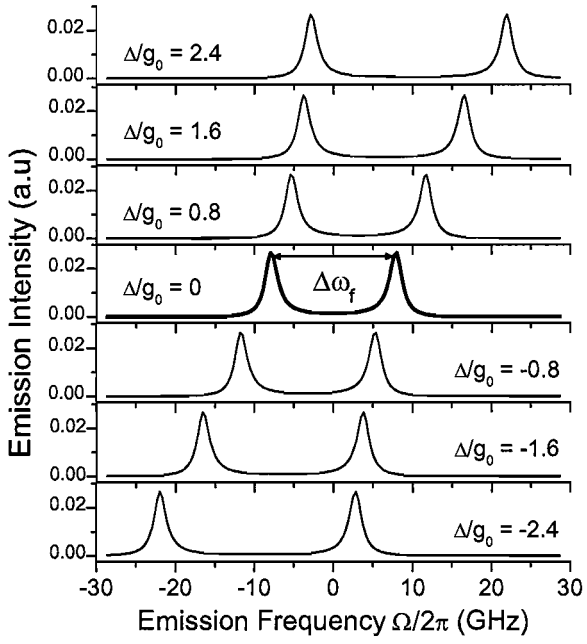

(b)

FIGURE 4.4: Normalized side emission spectra (a), and forward emission spectra (b) for seven different values of atom-cavity detuning, given $(g_0, \kappa, \gamma)/2\pi$ = (8.0, 1.6, 0.32) GHz.

for the cavity-modified forward emission (useful cavity output) and side emission spectra of single photons emitted from a cavity.

In real experiments, all single-quantum systems inevitably interact with certain heat baths, leading to dephasing or loss of coherence, even without change in the populations of the system, the so-called pure dephasing. All the results derived in this chapter are subject to modification by pure dephasing, particularly when temperature tuning of the QD has to be used to tune through cavity resonance. In the next chapter, we study the influence of pure dephasing process on the vacuum Rabi oscillations, the quantum efficiency and the emission spectra.

CHAPTER V

INFLUENCE OF PURE DEPHASING

In this chapter, we investigate the influence of pure dephasing, treated in the phase-diffusion model based on a Wiener-Levy process, on the single-photon sources in the cavity-QED strong-coupling regime. The pure dephasing process can affect several characteristics of a single-photon source: broadening the emission linewidths of the single photons emitted from the source, preventing them from lifetime limited; smearing the visibility of two-photon interference, spoiling the indistinguishability of consecutively emitted photons; and decreasing the quantum efficiency of the single-photon source.

5.1 Introduction

Most if not all single-quantum systems, like an optical center either in gaseous phase or in a solid state matrix, inevitably interacts with certain heat baths, leading to dephasing or loss of coherence, which results from a randomization of the phases of the optical center's wave functions by thermal fluctuations in the environmental fields. Population relaxation processes, treated in the previous chapter, contribute to dephasing with a dephasing rate given by half the population decay rate. It is often necessary to account for other dephasing interactions, such as elastic collisions in an atomic vapor, or elastic phonon scattering in a solid, the so-called pure dephasing process.

Generally speaking, pure dephasing means the decay of the dipole coherence without change in the populations of the system. Any real transition to other states leads to population decay. Thus the pure dephasing is caused by virtual processes

which start from a relevant state and, through some excursion in the intermediate states, return to the same initial state. These virtual processes give rise to the temporal fluctuations of phases of the wave functions, which consequently lead to pure dephasing. Pure dephasing causes the coherent overlap of the upper and lower state wave functions to decay in time, while not affecting the state populations. For example, the pure dephasing rate can be small and ignored for resonant excitation of a single QD at cryogenic temperature (6 K) and low power density [101]. While at elevated temperatures, however, experiments [49, 50] reveal a pure dephasing contribution that dominates excitonic dephasing. Our results are directly applicable to experimental data presented in Refs. [44, 45, 47, 48].

In this chapter, we investigate the effects of pure dephasing, treated in the phase-diffusion model based on a Wiener-Levy process on all the results obtained in Chapter IV. In Sec. 5.2, we built the phase-diffusion model described by a stochastic model of random frequency modulation. Based on this model, we solve the stochastic equations of motion and calculate the influence of pure dephasing on the vacuum Rabi oscillations and the quantum efficiency in Secs. 5.3 and 5.4, respectively. Finally, in Sec. 5.5 we calculate the emission spectra in the presence of the pure dephasing. We found that the depths of the vacuum Rabi oscillations are reduced, the quantum efficiency is decreased, and the emission spectra are broadened in the presence of pure dephasing. Part of the work discussed here has been published in Ref. [52].

5.2 Phase-diffusion Model for Pure Dephasing

The effects of pure dephasing can be calculated numerically, based on the Green function formalism by considering the microscopic details of various virtual processes [178]. Instead, for simplicity we treat this problem analytically in the phase-diffusion model where the incoherence due to elastic collisions or elastic phonon scattering is described by a stochastic model of random frequency modulation, as shown in Fig. 5.1, replacing the previously constant atomic transition frequency as in Eq. (4.6) or

the phase of the wave function by an instantaneous one

$$\begin{aligned} \omega_0 &\rightarrow \omega_0(t) = \omega_0 + f(t) \quad \text{or} \\ \omega_0 t &\rightarrow \int_0^t dt' \omega_0(t') = \omega_0 t + \varphi(t), \end{aligned} \tag{5.1}$$

where $f(t)$ is the instantaneous deviation of the transition frequency due to the elastic collisions or scattering process and $\varphi(t) \equiv \int_0^t f(t')dt'$ is the instantaneous stochastic phase of the wave function. We assume the phase of the wave function is a Wiener-

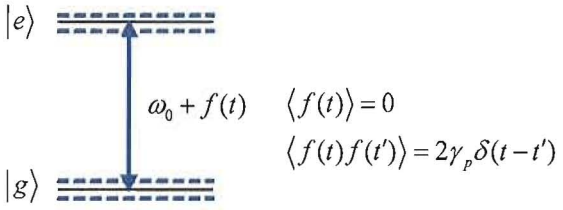

FIGURE 5.1: Schematic diagram and analytical description of pure dephasing processes in the phase-diffusion model.

Levy process [179]. In this phase-diffusion model $f(t) \equiv \dot{\varphi}(t)$ is a random, stationary, Gaussian variable with the mean value and the mean-square correlation given by

$$\langle f(t) \rangle = 0, \; \langle f(t) f(t') \rangle = 2\gamma_p \, \delta(t - t'). \tag{5.2}$$

The angular brackets indicate a statistical average over the random variables of the stochastic process. The Markovian nature of the process is reflected by the presence of the delta function $\delta(t - t')$. The Gaussian property is introduced such that all higher correlation functions can be obtained from the second-order correlation function by permutations and multiplications [176]. $2\gamma_p$ is the pure dephasing rate.

Taking into account the pure dephasing modeled by the stochastic process, the net changes for equations of motion of $E(t)$ and $C(t)$, as given in Chapter IV, are that the phase terms $e^{i\Delta t}$ in Eqs. (4.20) and (4.21) should be replaced by $e^{i[\Delta t + \varphi(t)]}$,

such that

$$\dot{E}(t) = -ig_0 e^{i[\Delta t+\varphi(t)]} C(t) - \gamma E(t), \tag{5.3}$$

$$\dot{C}(t) = -ig_0 e^{-i[\Delta t+\varphi(t)]} E(t) - \kappa C(t). \tag{5.4}$$

We note that the above equations with stochastic random variables are examples of a multiplicative stochastic process, studied intensively previously by various researchers, as shown in Refs. [180, 181, 182]. We solve these equations exactly, using the method developed by Wodkiewicz [182] for a multiplicative stochastic process described by the following general vector equation

$$\frac{d}{dt}\vec{v}(t) = [M_0 + if(t)M_1]\,\vec{v}(t), \tag{5.5}$$

where $\vec{v}(t)$ is an n-dimensional vector, M_0 and M_1 are arbitrary $n \times n$ matrices, in general complex and time independent, and $f(t)$ is the random variable of the stochastic process described by Eq. (5.2). The equations of the type (5.5) can be solved for the quantum expectation value of $\vec{v}(t)$ exactly [182]. For a Wiener-Levy process, the stochastic average of the equation satisfies the following differential equation

$$\frac{d}{dt}\langle\vec{v}(t)\rangle = \left[M_0 - \gamma_p M_1^2\right]\langle\vec{v}(t)\rangle\,. \tag{5.6}$$

The solution to Eq. (5.6) can be written in the Laplace-transform form

$$\langle\vec{v}(t)\rangle = \int_C \frac{dz}{2\pi i}\exp(zt)N^{-1}(z)\,\langle\vec{v}(0)\rangle, \tag{5.7}$$

where the matrix $N^{-1}(z)$ is the inverse to $N(z)$, which itself is given by the formula $N(z) = z\mathbb{I} - (M_0 - \gamma_p M_1^2)$. In Eq. (5.7), the contour of integration C lies parallel to the imaginary axis in the complex z plane, to the right of all singularities of the integrands. In order to find the time behavior of $\langle\vec{v}(t)\rangle$, we have to invert the matrix $N(z)$, whose determinant plays an essential role because the roots of its secular equation are the poles of the integration in Eq. (5.7).

5.3 Vacuum Rabi Oscillations in the Presence of Pure Dephasing

We proceed to solve the stochastic Eqs. (5.3) and (5.4). For simplicity, we consider the case when the emitter and the cavity are in resonance, $\Delta = 0$. The detuning can always be put back without difficulty. First, by making the substitutions $E(t) = \tilde{E}(t)e^{-\gamma t}$ and $C(t) = \tilde{C}(t)e^{-\kappa t}$ for convenience, we obtain the following simpler equations

$$\dot{\tilde{E}}(t) = -ig_0 e^{-\Gamma t} e^{i\varphi(t)} \tilde{C}(t), \tag{5.8}$$

$$\dot{\tilde{C}}(t) = -ig_0 e^{\Gamma t} e^{-i\varphi(t)} \tilde{E}(t). \tag{5.9}$$

Then by defining variable $Y(t) = e^{-\Gamma t + i\varphi(t)}\tilde{C}(t)$ so that the differential equation for $\tilde{E}(t)$ does not explicitly depend on the random variable $\varphi(t)$, we obtain a matrix equation of the type (5.5) for a multiplicative stochastic process, with

$$\vec{v}(t) = \begin{pmatrix} \tilde{E}(t) \\ Y(t) \end{pmatrix}, M_0 = \begin{pmatrix} 0 & -ig_0 \\ -ig_0 & -\Gamma \end{pmatrix}, M_1 = \begin{pmatrix} 0 & 0 \\ 0 & 1 \end{pmatrix} \tag{5.10}$$

and a statistically independent initial condition $\langle \vec{v}(0) \rangle^T = (\tilde{E}(0), Y(0))$. The inverse matrix to the matrix $N(z)$ is

$$N^{-1}(z) = \frac{1}{\det[N(z)]} \begin{pmatrix} z + \Gamma + \gamma_p & -ig_0 \\ -ig_0 & z \end{pmatrix}. \tag{5.11}$$

Plugging Eq. (5.11) back into Eq. (5.7), using the Laplace transform technique and choosing properly the contour of integration C, we obtain the quantum expectation value of the probability amplitude $\langle \tilde{E}(t) \rangle$,

$$\begin{aligned} \left\langle \tilde{E}(t) \right\rangle &= \int_C \frac{dz}{2\pi i} e^{zt} \frac{(z + \Gamma + \gamma_p)\tilde{E}(0) - ig_0 Y(0)}{(z - z_1)(z - z_2)} \\ &= e^{-(\Gamma + \gamma_p)t/2} \\ &\quad \times \left\{ \left[\cos(g_1 t) + \frac{\Gamma + \gamma_p}{2g_1} \sin(g_1 t) \right] \tilde{E}(0) - \left[\frac{ig_0}{g_1} \sin(g_1 t) \right] Y(0) \right\}, \end{aligned} \tag{5.12}$$

where $g_1 \equiv \sqrt{g_0^2 - (\Gamma + \gamma_p)^2/4}$. Similarly, if we define $X(t) = e^{\Gamma t - i\varphi(t)}\tilde{E}(t)$, while keeping $\tilde{C}(t)$ unchanged, we obtain

$$\begin{aligned}\left\langle \tilde{C}(t) \right\rangle =& e^{(\Gamma-\gamma_p)t/2} \\ & \times \left\{ \left[\cos(g_2 t) - \frac{\Gamma - \gamma_p}{2g_2} \sin(g_2 t) \right] \tilde{C}(0) - \left[\frac{ig_0}{g_2} \sin(g_2 t) \right] X(0) \right\},\end{aligned} \tag{5.13}$$

where $g_2 \equiv \sqrt{g_0^2 - (\Gamma - \gamma_p)^2/4}$. Taking into account the definitions of $\tilde{E}(t)$ and $\tilde{C}(t)$, as well as the fact that $X(0) = \tilde{E}(0) = E(0)$ and $Y(0) = \tilde{C}(0) = C(0)$, we transform back to $E(t)$ and $C(t)$,

$$\begin{aligned}\begin{pmatrix} \langle E(t) \rangle \\ \langle C(t) \rangle \end{pmatrix} &= e^{-(\mathrm{K}+\gamma_p)t/2} \\ \times \begin{pmatrix} \cos(g_1 t) + \dfrac{\Gamma + \gamma_p}{2g_1} \sin(g_1 t) & -\dfrac{ig_0}{g_1} \sin(g_1 t) \\ -\dfrac{ig_0}{g_2} \sin(g_2 t) & \cos(g_2 t) - \dfrac{\Gamma - \gamma_p}{2g_2} \sin(g_2 t) \end{pmatrix} & \begin{pmatrix} E(0) \\ C(0) \end{pmatrix}.\end{aligned} \tag{5.14}$$

The generalized Rabi frequencies for $\langle E(t) \rangle$ and $\langle C(t) \rangle$ now are different from each other, as compared to Eq. (4.24) in Chapter IV, where they were the same for both $\langle E(t) \rangle$ and $\langle C(t) \rangle$. This implies the destroying of coherence between the two eigenstates of the system, due to the pure dephasing process. We will show this phase-destroying effect on the vacuum Rabi oscillations explicitly later in this section.

We are more interested in finding the influence of the pure dephasing on the probabilities $|C(t)|^2$ and $|E(t)|^2$, or $I(t) \equiv |\tilde{C}(t)|^2$ and $J(t) \equiv |\tilde{E}(t)|^2$, because they give the normal-mode oscillations and are what one measures in experiment. In order to find the equations of motion for them, we have to introduce two other one-time functions $H(t) \equiv \tilde{E}(t)\tilde{C}^*(t)$ and $H^*(t) \equiv \tilde{E}^*(t)\tilde{C}(t)$. The equations of motion for these functions are

$$\frac{d}{dt} \begin{pmatrix} H(t) \\ H^*(t) \\ I(t) \\ J(t) \end{pmatrix} = \tilde{M}(t) \times \begin{pmatrix} H(t) \\ H^*(t) \\ I(t) \\ J(t) \end{pmatrix}, \tag{5.15}$$

with the matrix $\tilde{M}(t)$ being

$$\tilde{M}(t) = \begin{pmatrix} 0 & 0 & -ig_0 e^{-\Gamma t + i\varphi(t)} & ig_0 e^{\Gamma t + i\varphi(t)} \\ 0 & 0 & ig_0 e^{-\Gamma t - i\varphi(t)} & -ig_0 e^{\Gamma t - i\varphi(t)} \\ -ig_0 e^{\Gamma t - i\varphi(t)} & ig_0 e^{\Gamma t + i\varphi(t)} & 0 & 0 \\ ig_0 e^{-\Gamma t - i\varphi(t)} & -ig_0 e^{-\Gamma t + i\varphi(t)} & 0 & 0 \end{pmatrix}. \quad (5.16)$$

We solve these equations assuming the optical center is prepared in an excited state $E(0) = 1$, $C(0) = 0$ at time $t_0 = 0$. We solve these one-time functions one by one as we did above for solving $\langle E(t)\rangle$ and $\langle C(t)\rangle$. For example, to find the solution to $\langle I(t)\rangle$, defining $U_I(t) = e^{\Gamma t - i\varphi(t)} H(t)$, $U_I^* = e^{\Gamma t + i\varphi(t)} H^*(t)$, $Z_I(t) = e^{2\Gamma t} J(t)$ and keeping $I(t)$ unchanged, we obtain a matrix equation as the standard vector form of Eq. (5.5), with $[\vec{v}_I(t)]^T = [U_I(t),\, U_I^*(t),\, I(t),\, Z_I(t)]$, and

$$M_0 = \begin{pmatrix} \Gamma & 0 & -ig_0 & ig_0 \\ 0 & \Gamma & ig_0 & -ig_0 \\ -ig_0 & ig_0 & 0 & 0 \\ ig_0 & -ig_0 & 0 & 2\Gamma \end{pmatrix}, \; M_1 = \begin{pmatrix} -1 & 0 & 0 & 0 \\ 0 & 1 & 0 & 0 \\ 0 & 0 & 0 & 0 \\ 0 & 0 & 0 & 0 \end{pmatrix} \quad (5.17)$$

and a statistically independent initial condition $\langle \vec{v}_I(0)\rangle^T = (0,\, 0,\, 0,\, 1)$, where we have used the initial conditions at $t_0 = 0$, as well as the definitions of $\tilde{E}(t)$, $\tilde{C}(t)$ and $\vec{v}_I(t)$.

In the cavity-QED strong-coupling regime, $(4g_0^2 - \Gamma^2) \gg \Gamma^2, \gamma_p^2$, the solution for $\langle I(t)\rangle$ is found to be well approximated by (see Appendix B)

$$\langle I(t)\rangle = \frac{g_0^2}{2g^2} e^{[\Gamma - \gamma_p(1+\varepsilon)/2]t} \left[e^{\gamma_p(1+3\varepsilon)t/2} - \frac{\gamma_p}{4g} \sin(2gt) - \cos(2gt) \right], \quad (5.18)$$

where $\varepsilon \equiv (\Gamma/2g)^2$, and $g \equiv \sqrt{g_0^2 - (\Gamma/2)^2}$ is the generalized Rabi frequency, as defined before. Treating γ_p/g as a perturbation parameter, we kept the order to $O(\gamma_p/g)$ in the coefficients and the order to $O(\gamma_p \varepsilon/g)$ in the exponential arguments. Similarly, after some tedious algebra, we find the time evolutions of $\langle J(t)\rangle$ and $\langle H(t)\rangle$

are (see Appendixes B),

$$\langle J(t)\rangle = \frac{g_0^2}{2g^2} e^{-[\Gamma+\gamma_p(1+\varepsilon)/2]t} \times \left\{ e^{\gamma_p(1+3\varepsilon)t/2} - \left[\frac{\gamma_p}{4g} - \frac{g(\Gamma-\gamma_p/2)}{g_0^2}\right]\sin(2gt) - \left(1 - \frac{2g^2}{g_0^2}\right)\cos(2gt)\right\}, \quad (5.19)$$

$$\langle H(t)\rangle = \frac{ig_0}{2g} e^{-\gamma_p(3+\varepsilon)t/2} \times \left[\frac{3\Gamma}{2g} e^{\gamma_p(1-7\varepsilon)t/2} - \frac{\Gamma-\gamma_p}{g} e^{-\gamma_p(1-9\varepsilon)t/2} - \frac{\Gamma+2\gamma_p}{2g}\cos(2gt) + \sin(2gt)\right]. \quad (5.20)$$

Finally, the quantum expectation value of the complex conjugate of $H(t)$ is just the complex conjugate of its quantum expectation value $\langle H^*(t)\rangle = \langle H(t)\rangle^*$. Using the definitions of $\tilde{E}(t)$ and $\tilde{C}(t)$, we can easily find the solutions for $\langle |E(t)|^2\rangle = e^{-2\gamma t}\langle J(t)\rangle$ and $\langle |C(t)|^2\rangle = e^{-2\kappa t}\langle I(t)\rangle$. Therefore, the probability of finding the system in the excited atomic state, including the pure dephasing, is

$$\langle P_e(t)\rangle = \left\langle |E(t)|^2\right\rangle = \frac{g_0^2}{2g^2} e^{-[\mathrm{K}+\gamma_p(1+\varepsilon)/2]t} \times \left\{ e^{\gamma_p(1+3\varepsilon)t/2} - \left[\frac{\gamma_p}{4g} - \frac{g(\Gamma-\gamma_p/2)}{g_0^2}\right]\sin(2gt) - \left(1 - \frac{2g^2}{g_0^2}\right)\cos(2gt)\right\}. \quad (5.21)$$

Shown in Fig. 5.2(a) and 5.2(b) are plots of the probability $P_e(t)$ with linear and logarithmic scales respectively, in the presence of pure dephasing. And the probability of finding the system in the single cavity mode $P_c(t)$, subject to pure dephasing process is

$$\begin{aligned}\langle P_c(t)\rangle &= \left\langle |C(t)|^2\right\rangle \\ &= \frac{g_0^2}{2g^2} e^{-[K+\gamma_p(1+\varepsilon)/2]t}\left[e^{\gamma_p(1+3\varepsilon)t/2} - \frac{\gamma_p}{4g}\sin(2gt) - \cos(2gt)\right].\end{aligned} \quad (5.22)$$

Shown in Fig. 5.3(a) and 5.3(b) are plots of the probability $P_c(t)$ in the presence of pure dephasing. The plotting parameters are the same as those in Fig. 5.2. The modulation depths of the dot and triangle curves, with pure dephasing rates $\gamma_p/2\pi =$ (1.0, 2.5) GHz, are reduced, as compared with the square curves where there is no

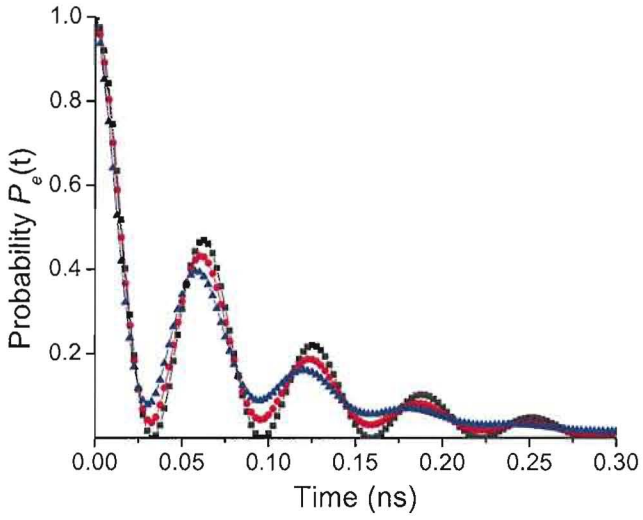

(a)

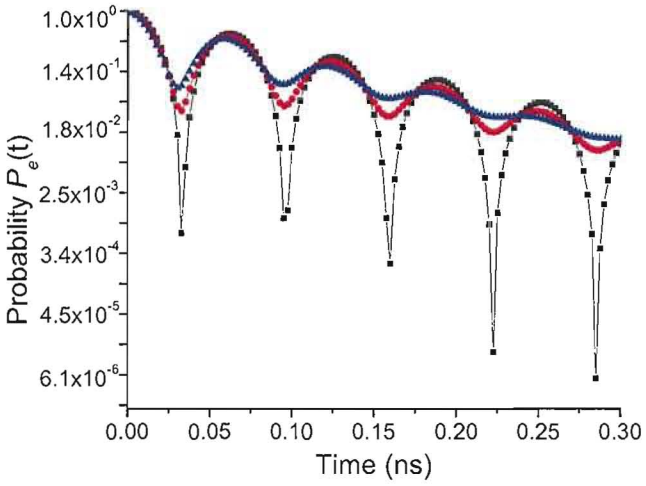

(b)

FIGURE 5.2: The probability of finding the optical center in its excited state: (a) linear scale, and (b) logarithmic scale for three different pure-dephasing rates $\gamma_p/2\pi$ = (0, 1.0, 2.5) GHz (square, dot and triangle respectively), given $(g_0, \kappa, \gamma)/2\pi$ = (8.0, 1.6, 0.32) GHz.

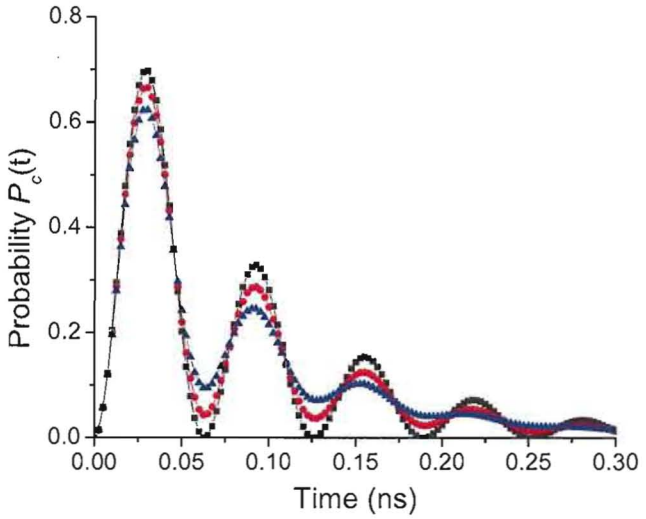

(a)

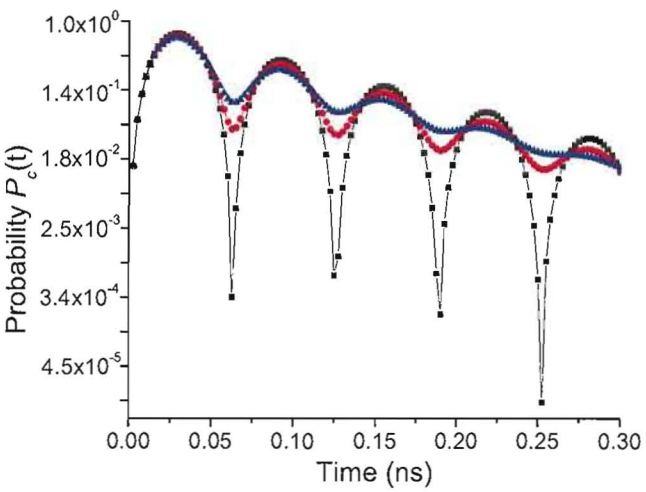

(b)

FIGURE 5.3: The probability of finding a photon in the cavity mode: (a) linear scale, and (b) logarithmic scale for three different pure-dephasing rates $\gamma_p/2\pi$ = (0, 1.0, 2.5) GHz (square, dot and triangle respectively).

pure dephasing. The normal-mode oscillation frequency seems unaffected because we solved for the probabilities only up to first order in γ_p/g. In fact, it will change slightly from $2g$ to $2g(1-\gamma_p^2/32g^2)$ if we approximate to second order in γ_p/g. The normal-mode oscillations are smeared in the presence of the pure dephasing process.

5.4 Quantum Efficiency in the Presence of Pure Dephasing

Consequently, the emission probability of a single photon into the forward beam and the QE with the pure dephasing process, as defined before, are

$$\begin{aligned}\langle P_o(t)\rangle &= 2\kappa\int_0^t dt'\,\langle|C(t')|^2\rangle \\ &= \frac{\kappa g_0^2}{g^2}\left\{\frac{1-e^{-(K-\gamma_p\varepsilon)t}}{K-\gamma_p\varepsilon}-\frac{K+\gamma_p(1+\varepsilon/2)}{[K+\gamma_p(1+\varepsilon)/2]^2+(2g)^2}\right\} \\ &\quad+\frac{\kappa g_0^2}{g^2}\frac{e^{-[K+\gamma_p(1+\varepsilon)/2]t}}{[K+\gamma_p(1+\varepsilon)/2]^2+(2g)^2} \\ &\times\left\{[K+\gamma_p(1+\varepsilon)/2]\left[\frac{\gamma_p}{4g}\sin(2gt)+\cos(2gt)\right]+2g\left[\frac{\gamma_p}{4g}\cos(2gt)-\sin(2gt)\right]\right\},\end{aligned} \tag{5.23}$$

and

$$\eta_q(\gamma_p)\equiv\langle P_o(t\to\infty)\rangle=\frac{g_0^2}{g^2}\frac{\kappa}{K-\gamma_p\varepsilon}\left\{1-\frac{(K-\gamma_p\varepsilon)[K+\gamma_p(1+\varepsilon/2)]}{[K+\gamma_p(1+\varepsilon)/2]^2+(2g)^2}\right\}. \tag{5.24}$$

These results reduce to our earlier results, given in Chapter IV, in the limit $\gamma_p\to 0$. Figure 5.4(a) are plots of the emission probabilities with and without pure dephasing, and Fig. 5.4(b) is the QE η_q as a function of the pure dephasing rate. Other plotting parameters are the same as in Fig. 5.2. The emission probability is also smeared for a pure dephasing rate $\gamma_p/2\pi = 4$ GHz compared with no pure dephasing. The QE decreases only about 1% as the dephasing rate increases from 0 to 4 GHz.

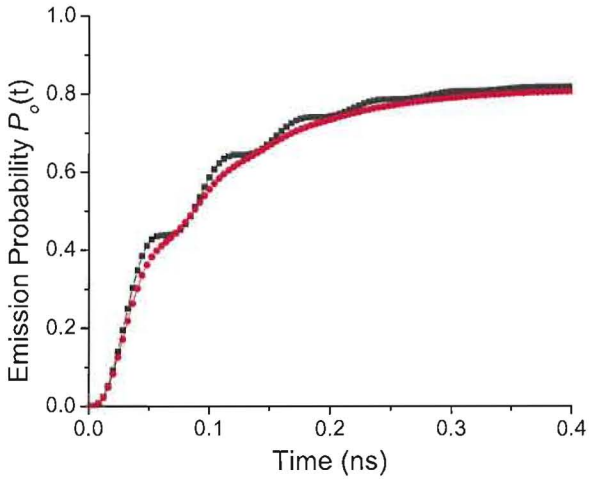

(a)

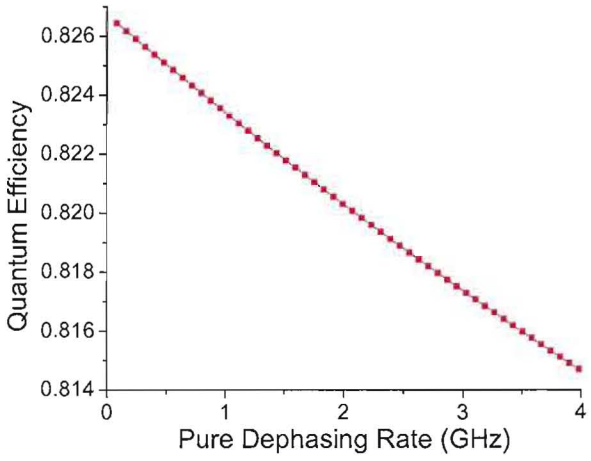

(b)

FIGURE 5.4: (a) Emission probabilities without and with pure dephasing $\gamma_p/2\pi = 4$ GHZ (square and dot curves respectively). (b) The QE η_q as a function of the pure dephasing rate.

5.5 Emission Spectra in the Presence of Pure Dephasing

In order to calculate the emission spectra, we need to find the two-time correlation functions because the emission spectra in the long-time limit are proportional to the Fourier transform of their convolutions. The two-time correlation functions are defined as follows:

$$Q(t,t') \equiv \tilde{E}(t)\tilde{E}^*(t'),\ R(t,t') \equiv \tilde{C}(t)\tilde{E}^*(t'), \tag{5.25}$$

$$F(t,t') \equiv \tilde{E}(t)\tilde{C}^*(t'),\ G(t,t') \equiv \tilde{C}(t)\tilde{C}^*(t'). \tag{5.26}$$

Of these $Q(t,t')$ and $G(t,t')$ are required for calculating the emission spectra. The quantum regression theorem [183, 168], which provides a framework to calculate two-time correlation functions, states that the equations of motion for two-time correlation functions $Q(t,t')$ and $R(t,t')$ and $F(t,t')$ and $G(t,t')$ with respect to variable t obey the same equations of motion as those for $\tilde{E}(t)$ and $\tilde{C}(t)$, respectively,

$$\partial_t Q(t,t') = -ig_0 e^{-\Gamma t} e^{i\varphi(t)} R(t,t'), \tag{5.27}$$

$$\partial_t R(t,t') = -ig_0 e^{\Gamma t} e^{-i\varphi(t)} Q(t,t'), \tag{5.28}$$

$$\partial_t F(t,t') = -ig_0 e^{-\Gamma t} e^{i\varphi(t)} G(t,t'), \tag{5.29}$$

$$\partial_t G(t,t') = -ig_0 e^{\Gamma t} e^{-i\varphi(t)} F(t,t'), \tag{5.30}$$

but now with initial conditions

$$Q(t=t',t') = |\tilde{E}(t')|^2 \equiv J(t'), \tag{5.31}$$

$$R(t=t',t') = \tilde{C}(t')\tilde{E}^*(t') \equiv H^*(t'), \tag{5.32}$$

$$F(t=t',t') = \tilde{E}(t')\tilde{C}^*(t') \equiv H(t'), \tag{5.33}$$

$$G(t=t',t') = |\tilde{C}(t')|^2 \equiv I(t'), \tag{5.34}$$

which are already solved and given explicitly by Eqs. (5.18) to (5.20).

We now specialize to the case $t \geq t'$ and define $t \equiv t' + \tau$. We are particularly interested in the expectation values of $\langle Q(t'+\tau,t')\rangle$ and $\langle G(t'+\tau,t')\rangle$ as pointed

out before. The solutions for their expectation values, according to the quantum regression theorem, have the same forms as the solutions for the one-time averages of $\langle\tilde{E}(t)\rangle$ and $\langle\tilde{C}(t)\rangle$ in Eqs. (5.12) and (5.13), with the initial conditions given above:

$$\langle Q(t'+\tau,t')\rangle = e^{-(\Gamma+\gamma_p)\tau/2} \times\left\{\left[\cos(g_1\tau)+\frac{\Gamma+\gamma_p}{2g_1}\sin(g_1\tau)\right]\langle J(t')\rangle-\left[\frac{ig_0}{g_1}\sin(g_1\tau)\right]\langle H^*(t')\rangle\right\}, \quad (5.35)$$

$$\langle G(t'+\tau,t')\rangle = e^{(\Gamma+\gamma_p)\tau/2} \times\left\{\left[\cos(g_2\tau)-\frac{\Gamma-\gamma_p}{2g_2}\sin(g_2\tau)\right]\langle I(t')\rangle-\left[\frac{ig_0}{g_2}\sin(g_2\tau)\right]\langle H(t')\rangle\right\}. \quad (5.36)$$

By substituting $\tilde{E}(t') = E(t')e^{\gamma t'}$, $\tilde{C}(t') = C(t')e^{\kappa t'}$ and the initial conditions into Eqs. (5.35) and (5.36), we obtain the explicit solutions for $\langle E(t'+\tau)E^*(t')\rangle$ and $\langle C(t'+\tau)C^*(t')\rangle$. The side emission and forward emission spectra are then

$$S_{s.e.}(\Omega) = \frac{2\gamma}{\pi}\mathrm{Re}\left\{\int_0^\infty d\tau e^{i\Omega\tau}\left[\int_0^\infty dt'\,\langle E(t'+\tau)E^*(t')\rangle\right]\right\} \quad (5.37)$$

$$= \frac{g_0^2}{g^2}\mathrm{Re}\left\{\frac{\gamma/\pi}{\left[\left(K+\gamma_p\right)/2-i\Omega\right]^2+g_1^2}\right\} \times\left\{\frac{-3\Gamma}{2\left(K+\gamma_p+4\gamma_p\varepsilon\right)}-\frac{2g^2-\left[K+\gamma_p\left(3+\varepsilon\right)/2\right]\left(\Gamma/2+\gamma_p\right)}{\left[K+\gamma_p\left(3+\varepsilon\right)/2\right]^2+\left(2g\right)^2}+\frac{\Gamma-\gamma_p}{K+2\gamma_p-4\gamma_p\varepsilon}\right\}$$

$$+\frac{g_0^2}{g^2}\mathrm{Re}\left\{\frac{\left(\gamma/\pi\right)\left(\kappa+\gamma_p-i\Omega\right)}{\left[\left(K+\gamma_p\right)/2-i\Omega\right]^2+g_1^2}\right\} \times\left\{\frac{1}{K-\gamma_p\varepsilon}-\frac{K-4g^2\kappa/g_0^2+\gamma_p[1+(1-2g^2/g_0^2)\varepsilon/2]}{\left[K+\gamma_p\left(1+\varepsilon\right)/2\right]^2+\left(2g\right)^2}\right\},$$

$$S_{f.e.}(\Omega) = \frac{2\kappa}{\pi}\mathrm{Re}\left\{\int_0^\infty d\tau e^{i\Omega\tau}\left[\int_0^\infty dt'\,\langle C(t'+\tau)C^*(t')\rangle\right]\right\} \quad (5.38)$$

$$= \frac{g_0^2}{g^2}\mathrm{Re}\left\{\frac{\kappa/\pi}{\left[\left(K+\gamma_p\right)/2-i\Omega\right]^2+g_2^2}\right\} \times\left\{\frac{3\Gamma}{2\left(K+\gamma_p+4\gamma_p\varepsilon\right)}+\frac{2g^2-\left[K+\gamma_p\left(3+\varepsilon\right)/2\right]\left(\Gamma/2+\gamma_p\right)}{\left[K+\gamma_p\left(3+\varepsilon\right)/2\right]^2+\left(2g\right)^2}-\frac{\Gamma-\gamma_p}{K+2\gamma_p-4\gamma_p\varepsilon}\right\}$$

$$+\frac{g_0^2}{g^2}\mathrm{Re}\left\{\frac{\left(\kappa/\pi\right)\left(\gamma+\gamma_p-i\Omega\right)}{\left[\left(K+\gamma_p\right)/2-i\Omega\right]^2+g_2^2}\right\}\left\{\frac{1}{K-\gamma_p\varepsilon}-\frac{K+\gamma_p\left(1+\varepsilon/2\right)}{\left[K+\gamma_p\left(1+\varepsilon\right)/2\right]^2+\left(2g\right)^2}\right\}.$$

Shown in Figs. 5.5(a) and 5.5(b) are the side emission and forward emission spectra in the long-time limit, for different dephasing rates γ_p, while other plotting parameters are the same as those in Fig. 5.2. The effect of pure dephasing is twofold. The phase fluctuations decrease the peak intensities of the spectra, and broaden the linewidths of the two peaks and hence smear out the splittings, which correspond to damping rates of the vacuum Rabi oscillations in the time domain as shown in Figs. 5.2 and 5.3. This effect is further seen to increase with increasing values of pure dephasing rate γ_p.

5.6 Summary

In this chapter, we studied the influence of the pure dephasing process on the single-photon sources, in the case that the pure dephasing rate is significantly less than the coherent coupling rate, that is, up to first order in γ_p/g. These results should be useful in analyzing photoluminescence spectra from strongly coupled semiconductor-QD micro-cavities, where pure dephasing cannot always be assumed negligible because often temperature tuning of the QD has to be used to tune through cavity resonance [44, 45, 47]. One can use this method, for example, to model the time jitter of solid-state SPS, where the excited state of the QD or color center in diamond is often populated by spontaneous phonon emission, by averaging over nonradiative relaxation time. One may also calculate the two-photon interference visibility assuming having two independent but identical SPS and investigate how the pure dephasing processes affect the indistinguishability of the consecutively emitted single photons.

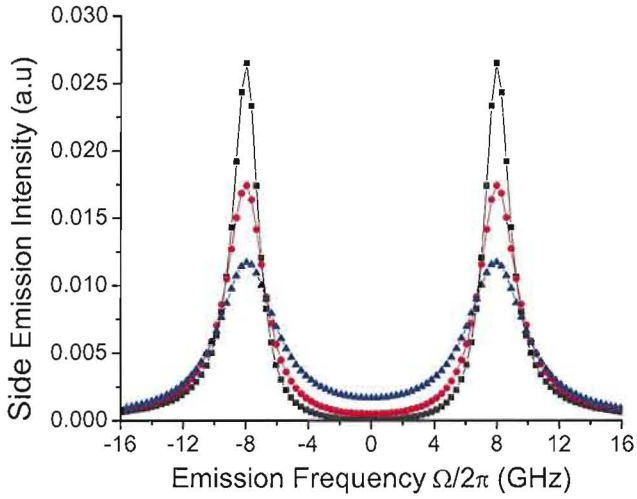

(a)

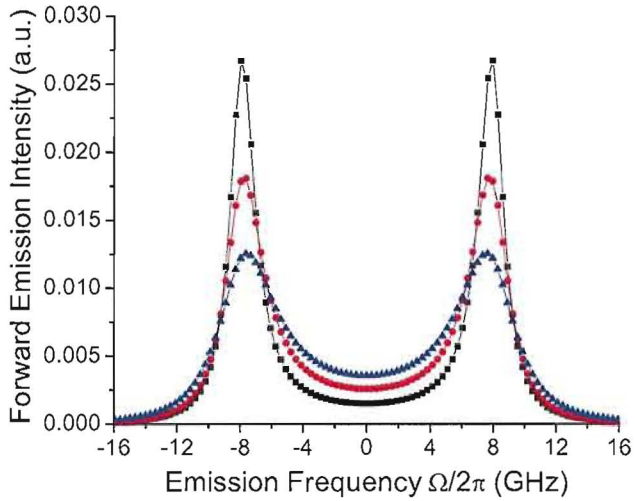

(b)

FIGURE 5.5: Normalized side emission spectra (a), and forward emission spectra (b), for three different pure dephasing rates $\gamma_p/2\pi$ = 0, 1.0, 2.5) GHz (square, dot and triangle respectively).

CHAPTER VI

CONCLUSIONS AND OUTLOOK

In this closing chapter, we first conclude the dissertation with our experimental accomplishment and theoretical contribution, before pointing out the challenges we are facing now. As designed and constructed, this external optical micro-cavity has the flexibility to adapt to other optical centers such as cold atoms in gaseous phase and defect centers in solids for efficient single-photon sources. Then, we give an outlook for possible incorporation of cold atoms on chips and color centers in diamond into this unique system, and for other applications in quantum information science and technology, such as generation of pairs of polarization-entangled photons.

6.1 Conclusions

For the research presented in this dissertation, we have been mainly exploiting the unique properties of nanoscale semiconductor QDs integrated with an external optical micro-cavity for cavity-QED studies, on both experimental and theoretical aspects [6, 52], particularly for efficient single-photon sources [51]. We have designed and constructed a hemispherical, high-solid-angle, external optical micro-cavity with semiconductor QDs at the focus of the cavity and at an antinode of the field to maximize the light-matter interaction.

A unique component of our cavity is the concave micro-mirror. We developed a technique, based on gas bubbles formed by surface tension inside molten glass, for its in-house fabrication, giving a surface roughness on nanometer scale for the dimple surface that is crucial for use in a high-finesse optical cavity. Optical coating of such a small and highly curved micro-mirror is nonstandard and is challenging. We designed

a dielectric coating that succeeded in giving a high reflectivity (99.5% or higher) over a wide angular range of ±40 deg.

We constructed the micro-cavity system on a sophisticated five-axis mechanical assembly to give all the necessary spatial and spectral controls. The whole micro-cavity system operates inside an ultra-high vacuum chamber, to allow cooling the sample to around 10-17 K and to avoid coating of the samples by cryopumping. We tested and characterized the optical properties of the micro-cavity to optimize the coherent interaction rate between the QDs and the micro-cavity. Preliminary spectroscopic results show significant of strong QD-field interaction. We also developed a theory of single-photon sources operating in the cavity-QED strong-coupling regime and investigated the influence of pure dephasing on its behavior in both the time domain and the frequency domain.

Major achievements and contributions are summarized below:

On the experimental side: we engineered a hemispherical, high-solid-angle, optical micro-cavity with a length of 60 μm. The external micro-cavity is comprised of a planar distributed Bragg reflector (DBR) mirror and a concave dielectric mirror. Nanoscale semiconductor QDs are embedded in the center of a one-wavelength spacer layer on top of the DBR mirror, to be placed at the focus of the hemispherical micro-cavity and an antinode of the cavity field to maximize the light-matter interaction. The hemispherical design gives a diffraction-limited spot at the QDs location, leading to higher spatial resolution and smaller cavity mode volume; the external-mirror approach provides maximum flexibility in scanning laterally to position QDs in the center of the cavity as well as providing the capability of scanning the cavity resonance to the spectral position of the isolated QDs, all of which are necessary and crucial for cavity-QED strong coupling and for efficient single-photon generation.

On the theoretical side: We formulated a theory of the interaction between a single quantum optical center and a single mode of a cavity field based on Weisskopf-Wigner theory dealing with spontaneous emission in free space. By solving the dynamics of

the composite system, we derived the Purcell effect in the cavity-QED weak-coupling regime and the vacuum Rabi oscillations in the cavity-QED strong-coupling regime. We advanced the understanding of single-photon emission in the cavity-QED strong-coupling regime that includes intrinsic dissipations of the coupled system. We also calculated the influence of pure dipole dephasing, treated in the phase-diffusion model based on a Wiener-Levy process, on the vacuum Rabi oscillations and the quantum efficiency in the time domain and the emission spectra in the frequency domain. This allows, for the first time, full modeling of the emission quantum efficiency, as well as the spectrum of the single photons emitted into the useful output mode of the cavity.

6.2 Future Work and Outlook

It is ideal to locate a single semiconductor QD in the QW plane in the middle of the one-wavelength spacer layer on the transverse plane of the DBR mirror; however, it is hard to single out an individual QD spatially that is also resonant with a single cavity mode. Most of the times, we observe signatures of interaction between many QDs and a single cavity mode which may also contain multiple photons, as shown by those spectroscopic scans in Chapter III. It is relatively easier to make one photon on average per cavity lifetime occupying a single mode, but it is still difficult to identify single QDs. It could be due to the statistical distribution of the QDs such that there are too many QDs in this particular location at which we are looking at, and also too many in this wavelength region where we are probing. The next logical step is to use a proper laser to probe the right spectral region where the QDs see the strongest field intensity due to their resonance with the spacer layer, as designed. We may also need to manually move the semiconductor sample to a different location by a large amount when opening the UHV chamber next time, if necessary. It is desirable, in the future, to theoretically modify multiple optical centers interacting with a single cavity mode both in the cavity-QED weak-coupling and strong-coupling regimes in order to better understand the physics and simulate the real experiments.

There are two general aspects about the semiconductor QDs that we can possibly improve for making better single-photon sources: the sizes of the QDs and the positions of the QDs on the growth plane. In terms of the uniformity of the sizes of the semiconductor QDs, the self-assembled QDs have more evenly distributed sizes [184], reducing size-dependent emissions, as compared with the IFQDs that we use whose emission wavelengths depend on their sizes. A less desirable feature of these self-assembled QDs is that they still form at random positions on the growth plane, as IFQDs do. However, great progress has been made to control the self-assembled QDs positions within the device structure by patterning nanoscale pits on the growth surface [185, 186]. So in the future, we could use patterned self-assembled QDs as our optical centers for efficient single-photon sources.

Semiconductor QDs are very promising on one hand, but they are intrinsically non-identical, albeit considerable progress has been made [185, 186] towards this goal. Diamond-based optical centers offer a better possibility to have identical emitters, since they are essentially ions or molecules embedded in well-defined, reproducible lattice sites [187]. Their envisioned role in QIP is promising, due to the tight localization of the electron spin and charge at the defect and long dephasing times of ground state spins. Researchers have tried to deposit natural diamond nanocrystals onto silica micro-spheres for cavity-QED studies. Signature of strong interaction between a nitrogen vacancy in diamond and a whispering gallery mode of a micro-sphere has been reported [188].

However, it is not straightforward to integrate diamond with other devices, mainly due to extremely demanding growth conditions for diamond thin films [189]. It is only recently demonstrated that good optical quality diamond thin films with color centers can be grown on certain substrates [190]. In Ref. [191], the author designed a resonator made of a cylindrical or spherical piece of a polymer squeezed between two flat dielectric mirrors. Diamond nanocrystals can be embedded in the polymer for single-photon generation. Another scheme, as reported in Ref. [192], proposed

a diamond based photonic crystal micro-cavity operating in the cavity-QED strong-coupling regime for quantum computing. But it is still challenging to incorporate diamond thin films onto a highly reflective mirror as a substrate, which is required to build a high-finesse optical cavity, because coatings for the commercially available mirrors all fail under the demanding growth conditions for diamond. We investigated this problem and think it is feasible to directly grow diamond in a Si_3N_4 spacer layer on top a specially designed Si_3N_4/SiO_2 DBR mirror [193, 194], or on top of a $Si_3N_4/SiON/SiO_2$ one if minimizing the weak absorption introduced by Si_3N_4 layer in the near infrared region is desired, as pointed out in Chapter II. Another design using AlN/SiO_2 DBR mirror [195, 196, 197] is also promising, since AlN has better optical properties (less absorption in the near infrared region) compared with Si_3N_4 but with more demanding growth conditions. In the future, we could incorporate diamond into our external optical micro-cavity for efficient single-photon sources and for quantum information processing (QIP).

Trapped atoms and ions are intrinsically identical, offering many advantages and already leading to important advances in the field of QIP [16, 159], but typically need relatively large setups, such as a magneto-optical trap, to trap and hold them. The recent developments on atom chips may get around this problem in the future, in combination with the state-of-the-art high-finesse optical micro-cavities [54, 198, 199]. We believe that a micro-cavity/atom chip device operating in the cavity-QED strong-coupling regime will expand the scientific application scope of the ultra-cold atoms in quantum information science and technology, in addition to efficient single-photon sources.

Other than the cavity-QED strong coupling and beyond the efficient single-photon generation. This composite micro-cavity system is also good for producing pairs of polarization-entangled photons [158], which are useful as a resource for quantum communication (teleportation). Entangled photon pairs based on radiative decay cascade of a biexciton in asymmetric semiconductor QDs in free space, like the ones

used in our experiment, have been proposed [200] and demonstrated [123, 201]. A semiconductor QD biexciton decays radiatively through two intermediate optically active exciton states, as shown in Fig. 2.10. In an ideal and symmetric QD, the cascade exciton emission will produce polarization-entangled photon pairs [122]. But in real semiconductor QDs, the frequency degeneracy of the intermediate exciton state is often broken, causing a small frequency splitting between the x-polarized and y-polarized excitons [122]. This is because of the in-plane anisotropy and asymmetry of the structural properties of the QDs, such as elongation of the QD along one crystal axis [111] and in-built strain in the crystal [184]. The splitting in turn provides 'which-path' information, preventing polarization entanglement of the intermediate exciton emissions.

The essential condition that must be met for two photons to be polarization entangled is that two possible paths for creating them must be indistinguishable. So if the 'which-path' information caused by the frequency splitting can be erased, one would again be able to produce polarization-entangled photon pairs. In Ref. [123], researchers used carefully selected unsplit InAs/GaAs QDs, or alternatively use split QDs but tuned to zero by an externally applied in-plane magnetic field to successfully generate polarization-entangled photon pairs. While in Ref. [201], researchers showed they can erase the 'which-path' information by careful spectral-filtering, thus also produce polarization-entangled photon pairs.

Based on the proposal for entangled pair-photon generation in Ref. [158], one can use adjacent longitudinal modes of a cavity to erase the 'which-path' information, ensuring two photons emitted in a cascade from a biexciton state of a QD to be in an indistinguishable fashion and therefore producing polarization-entangled photon pairs. The proposed technique relies on the principle that a QD inside a strongly coupled cavity can emit light only into one of the cavity modes. This determines the possible frequencies of any emitted photons, independently of the center frequency of the exciton emission line. When two exciton emission lines with frequencies are near

a cavity-mode frequency, the cavity can force the two exciton emissions into a cavity mode. Any photon found to be in the cavity mode could have originated from either emission, ensuring indistinguishability.

Considering spectroscopic properties of a biexciton in an IFQD, the biexciton shift ΔE, as shown in Fig. 2.10, is about a few meV and the fine structure splitting δE between the the x-polarized and y-polarized excitons is of the order tens of μeV. Our micro-cavity is in a special length regime (50-500 μm), corresponding to a FSR 1.2-12 meV, and has a linewidth about tens of μeV. It is thus feasible make the FSR equal to the biexciton shift ΔE and the linewidth equal to the fine structure splitting δE for certain IFQDs. Therefore, it should be possible to bring both doublets caused by the fine splitting close to cavity modes simultaneously by fine tuning the cavity length or the FSR to meet the requirements for generating polarization-entangled photon pairs. If necessary, an external DC electric field can be applied to introduce a Stark shift in the doublet, in addition to tune the cavity length alone. To generate polarization-entangle photon pairs based on our system is another promising direction to go for the future.

There have remarkable progresses been made during the past decades in generating efficient single-photon sources and entangled pair photons [83, 32]. Despite all these efforts, there are still many remaining challenges to make integrated and compact, reliable and bright quantum light sources for QIP. Our work demonstrates that we can devise the state-of-the-art facilities in the lab to exploit the quantum nature of light-matter interaction, and develop cutting-edge technology potential for industrial applications as well as for other academic applications, such as for QIP in cavity-QED with cold atoms on chips and color centers in diamond. We consider this research to be an indispensable step towards ultimate integrated devices for QIP in cavity-QED.

APPENDIX A

FABRICATION OF THE MICRO-CONCAVE MIRROR

In this appendix, we describe the detailed procedure of fabricating micro-concave mirror substrates and give a simple method for measuring their radii of curvatures and depths. We thank Ruediger Loeckenhoff for carrying out the initial work in our lab leading to successful fabrication of the micro-mirrors [146].

A.1 Procedure of Fabricating Micro-concave Mirror Substrates

We start with micro-capillaries (Drummond Microcaps) that are usually used to measure exactly one micro-liter of chemicals [202]. They are made of N-51A borosilicate glass from Kimble Glass with a refractive index n = 1.49 and a softening point of 785°C [203]. About 50 capillaries are put into a graphite crucible as shown in Fig. A.1(a) and are melted in a tube-furnace (Lindberg/Blue) at 1100°C in a nitrogen (or argon) atmosphere. While the capillaries collapse they enclose gas-bubbles of 40-100 μm in diameter. The melted glass is cooled down at 3 degree Celsius per minute. In the end, one gets an elliptically shaped glass bulk with major lateral sizes about 10-15 mm and minor sizes about 5-10 mm, as shown in Fig. A.1(b). A faster cooling rate might result in wrinkles.

After it is hardened, we grind and polish the glass bulk on a polishing station using first a 50 μm, and followed by a 15 μm and later a 6 μm grit-size diamond disc (Allied High Tech Products, Inc. [204]), featuring nickel-plated diamonds in a raised dot matrix pattern. By polishing to an arbitrary depth about 50 bubbles are opened.

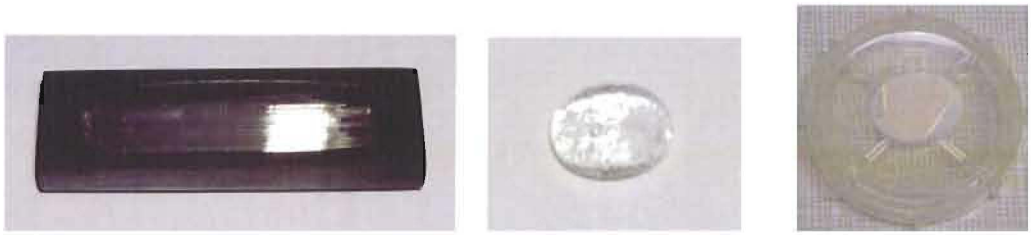

(a) (b) (c)

FIGURE A.1: (a) Glass tubes in a graphite crucible; (b) A hardened glass bulk with trapped gas bubbles; (c) A coated micro-concave mirror substrate.

We examine them under a microscope and if necessary will polish the glass bulk again using the 6 μm grit-size diamond disc until finding the most suitable dimples.

Glass particles sticking to the inner surface of the dimple is a major problem. Below a certain size about 5 μm they are bonded so tightly by Van der Waals force, that they can no longer be removed in the sonicator. By flowing cool soap water during polishing, we found that it forms a monolayer on the surface of the particles and the dimples and prevents sticking. This reduces the number of particles stuck to the inner surface of the dimple to about 1/5 based on our experiments.

The polished surface is temporarily glued to the center of an aluminum plate with Crystalbond 509 heat adhesive [205]. The dimples are thus protected from debris from contamination from the following polishing steps. Together with the sample three 170 μm thick microscope cover glass are glued to the aluminum plate periphery. In the following polishing steps they stabilize the plate and slow down the polishing so that we obtain a flat sample of about 150 μm thick.

A 30 μm grit-size diamond grinding disc is used for roughing followed by 15 μm and 6 μm grit-size diamond discs. The sample is then polished with diamond slurries (Polycrystalline Diamond Suspension, Glycol Based from Allied High Tech Products, Inc. [204]) of 6 μm and 1 μm grit-size on polishing cloths. An optical finish is achieved using a 0.05 μm colloidal silica suspension on a polishing cloth. The resulting thin slide is removed from the sample holder and cleaned in the sonicator with acetone

first to remove the remaining Crystalbond 509 heat adhesive. Soap water, purified water and methanol are then used in sequence to clean the dimple. The dimple is finished cleaning with isopropanol. Later the surface where the dimples are open will be coated with a highly reflective dielectric coating for use in a high-finesse optical cavity, while the other side of the slide with optical finishing is left uncoated. Figure A.1(c) shows the coated surface of a micro-concave mirror substrate.

A.2 Measuring the Radius of Curvature and Depth of a Dimple

For an uncoated clean dimple, we can estimate the radius of curvature of a dimple by measuring the diameter of the rim of the dimple, which is a cross section of the spherical gas bubble and is no larger than the diameter of the dimple. The diameter of the rim can be easily measured with a measuring eyepiece under a microscope. Determining the depth and the radius of curvature of a dimple is much harder since there are no structures at the bottom of a clean dimple that could be imaged. Fortunately for a coated dimple, we developed a simple but effective method to measure the radius of curvature and the depth of a dimple, described in the following.

We use the image of the illumination filament of the microscope that is situated in a distance S in front of the focal plane of the 25× objective. Moving a flat mirror by the distance $S/2 \approx 1000$ μm towards the objective we could see the image of the filament through the microscope. Compared to the size of the dimple ($R_{\mathrm{M}} \approx 50$ μm) we can set $S = \infty$. If we put a dimple under the microscope it will act as a concave spherical mirror imaging the filament at its focus with a distance $R_{\mathrm{M}}/2$ from its bottom. Consequently if we see an image of the polished surface and the filament at the same time through the microscope, the dimple is exactly polished to $R_{\mathrm{M}}/2$ and will have a half angle of 60 deg. Otherwise the sample has to be moved by a distance h to image the filament instead of the surface, as shown in Fig. A.2. Knowing the

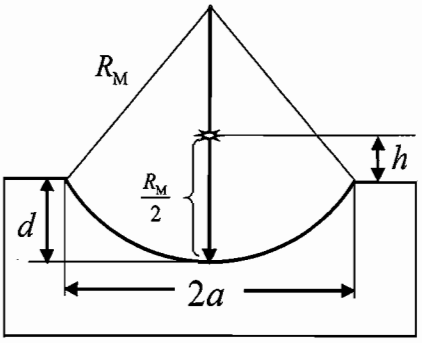

FIGURE A.2: Schematic diagram showing the filament image is above the polished surface, defined by $h > 0$; the opposite case is that the image is below the polished surface and $h < 0$.

diameter of the rim of a dimple $2a$ and the offset h, the radius of curvature R_M and the depth d of a dimple can then be calculated and they are related by

$$R_M = \frac{2}{3}\left(\sqrt{4h^2 + 3a^2} + h\right), \tag{A.1}$$

$$d = \frac{1}{3}\left(\sqrt{4h^2 + 3a^2} - 2h\right). \tag{A.2}$$

Use positive values for h when the image of the filament is above the polished surface and negative values when the image is below the polished surface.

We expect a good sphericity of the dimple since the surface tension is an increasingly strong force compared to other forces like gravity for decreasing dimensions. A Twyman-Green interferometer can be used to check the sphericity of the dimple qualitatively. The sphericity was measured quantitatively with a Wyko interferometer. One example is shown in Fig. 3.3. The surface roughness was also measured using a Wyko interferometer that carries out a Fourier-analysis of the surface to determine the power (spatial) spectral density (PSD) of surface roughness as a function of the lateral size of the errors. Figure 3.4 gives the PSD data of five dimples fabricated in this way presented here, as compared with the best polished dielectric mirrors used elsewhere.

APPENDIX B

TORREY SOLUTIONS TO THE SECULAR EQUATIONS

Here, we give the solutions to the secular equations based on an approximation discussed by H. C. Torrey [206].

B.1 Approximate Solution for $\langle I(t) \rangle$

From the Eq. (5.17) in the context, define matrix $M \equiv M_0 - \gamma_p M_1^2$, given explicitly by

$$M = \begin{pmatrix} \Gamma - \gamma_p & 0 & -ig_0 & ig_0 \\ 0 & \Gamma - \gamma_p & ig_0 & -ig_0 \\ -ig_0 & ig_0 & 0 & 0 \\ ig_0 & -ig_0 & 0 & 2\Gamma \end{pmatrix}. \tag{B.1}$$

Then the matrix $N_I(z) \equiv z\mathbb{I} - M$ and its determinant are

$$N_I(z) = \begin{pmatrix} z + \gamma_p - \Gamma & 0 & ig_0 & -ig_0 \\ 0 & z + \gamma_p - \Gamma & -ig_0 & ig_0 \\ ig_0 & -ig_0 & z & 0 \\ -ig_0 & ig_0 & 0 & z - 2\Gamma \end{pmatrix} \tag{B.2}$$

and

$$\det\left[N_I(z)\right] = (z + \gamma_p - \Gamma)\left[z\,(z - 2\Gamma)\,(z + \gamma_p - \Gamma) + 4g_0^2\,(z - \Gamma)\right]. \tag{B.3}$$

The secular equation is given by the vanishing of the determinant Eq. (B.3), which reduces to a cubic equation, for $z_1 = \Gamma - \gamma_p$,

$$(z - \Gamma)\left[(z - \Gamma)^2 + \gamma_p(z - \Gamma) + 4g_0^2 - \Gamma^2\right] = \gamma_p\Gamma^2, \tag{B.4}$$

which is the standard Torrey equation [206, 207]. This cubic equation can be solved exactly [208], although only in an implicit form. As Torrey has pointed out, in the special case of interest, this equation has a relatively simple explicit solution. We solve it in the strong-coupling regime, $\left(4g_0^2 - \Gamma^2\right) \gg \Gamma^2, \gamma_p^2$, in which case there are two kinds of roots. The first of these follows the assumption that $(z-\Gamma)^2$ is small compared with $\left(4g_0^2 - \Gamma^2\right)$, allowing one to rearrange the cubic equation (B.4) and solve by iteration

$$\begin{aligned} z - \Gamma &= \frac{\gamma_p \Gamma^2}{4g_0^2 - \Gamma^2}\left[1 + \frac{(z-\Gamma)(z-\Gamma+\gamma_p)}{4g_0^2 - \Gamma^2}\right]^{-1}, \\ z_2 &\approx \Gamma + \gamma_p \varepsilon + O\left[\left(\frac{\gamma_p}{g}\right)^3\right], \end{aligned} \tag{B.5}$$

where $\varepsilon \equiv (\Gamma/2g)^2$, and note that $g \equiv \sqrt{g_0^2 - (\Gamma/2)^2}$. The second kind of root occurs when $(z-\Gamma)^2$ is as large as $\left(4g_0^2 - \Gamma^2\right)$, but with opposite sign. The cubic equation (B.4) can be written as

$$(z-\Gamma)^2 + 4g_0^2 - \Gamma^2 = -\gamma_p(z-\Gamma)\left[1 - \frac{\Gamma^2}{(z-\Gamma)^2}\right]. \tag{B.6}$$

To first order in γ_p, the factor $(z-\Gamma)^2$ on the right-hand side, Eq. (B.6) can be replaced by $-(4g_0^2 - \Gamma^2)$. This gives a quadratic equation for $(z-\Gamma)$, $(z-\Gamma)^2 + \gamma_p(1+\varepsilon)(z-\Gamma) + 4g^2 = 0$, whose solutions are the third and fourth roots

$$\begin{aligned} z_{3,4} &\approx \Gamma - \frac{\gamma_p}{2}(1+\varepsilon) \pm i2g\sqrt{1 - (\gamma_p/4g)^2} + O\left[\left(\frac{\gamma_p}{g}\right)^2\right] \\ &\approx \Gamma - \frac{\gamma_p}{2}(1+\varepsilon) \pm i2g + O\left[\left(\frac{\gamma_p}{g}\right)^2\right]. \end{aligned} \tag{B.7}$$

The inverse matrix to the matrix $N_I(z)$ in Eq. (B.2) is

$$N_I^{-1}(z) = \frac{1}{\det\left[N_I(z)\right]} \begin{pmatrix} \bullet & \bullet & \bullet & \bullet \\ \bullet & \bullet & \bullet & \bullet \\ n_{31} & n_{32} & n_{33} & n_{34} \\ \bullet & \bullet & \bullet & \bullet \end{pmatrix}$$

with

$$\begin{aligned} n_{31} &= -ig_0\,(z-2\Gamma)\,(z+\gamma_p-\Gamma) \\ n_{32} &= ig_0\,(z-2\Gamma)\,(z+\gamma_p-\Gamma) \\ n_{33} &= (z+\gamma_p-\Gamma)\left[(z-2\Gamma)\,(z+\gamma_p-\Gamma)+2g_0^2\right] \\ n_{34} &= 2g_0^2\,(z+\gamma_p-\Gamma) \end{aligned}$$

where we only calculate the elements of the third row of $N_I^{-1}(z)$ because they are required to calculate $\langle I(t)\rangle$, which is then

$$\begin{aligned} \langle I(t)\rangle &= \int_C \frac{dz}{2\pi i} e^{zt} \frac{n_{34}}{(z-z_1)\,(z-z_2)\,(z-z_3)\,(z-z_4)} \\ &= \int_C \frac{dz}{2\pi i} e^{zt} \frac{2g_0^2}{(z-z_2)\,(z-z_3)\,(z-z_4)} \\ &\approx \frac{g_0^2}{2g^2} e^{[\Gamma-\gamma_p(1+\varepsilon)/2]t} \left[e^{\gamma_p(1+3\varepsilon)t/2} - \frac{\gamma_p}{4g}\sin(2gt) - \cos(2gt) \right], \end{aligned} \tag{B.8}$$

where we have used the initial condition that $\langle \vec{v}_I(0)\rangle^T = (0,\,0,\,0,\,1)$. Treating γ_p/g as a perturbation parameter, we kept the order to $O(\gamma_p/g)$ in the coefficients and the order to $O(\gamma_p\varepsilon/g)$ in the exponential arguments.

B.2 Approximate Solution for $\langle J(t)\rangle$

As it is clear from the definition of $\vec{v}_I(t)$, we can only obtain the solution for $\langle I(t)\rangle$ in the above calculation. In order to obtain the solution for $\langle J(t)\rangle$, we have to derive another equation of the type Eq. (5.5) with the definition of the vector $[\vec{v}_J(t)]^T = [U_J(t),\, U_J^*(t),\, W_J(t),\, J(t)]$, and the following matrices:

$$M_1 = \begin{pmatrix} -1 & 0 & 0 & 0 \\ 0 & 1 & 0 & 0 \\ 0 & 0 & 0 & 0 \\ 0 & 0 & 0 & 0 \end{pmatrix}, \; M_0 = \begin{pmatrix} -\Gamma & 0 & -ig_0 & ig_0 \\ 0 & -\Gamma & ig_0 & -ig_0 \\ -ig_0 & ig_0 & -2\Gamma & 0 \\ ig_0 & -ig_0 & 0 & 0 \end{pmatrix} \tag{B.9}$$

and with the initial condition $\langle \vec{v}_J(0) \rangle^T = (0, 0, 0, 1)$, where $U_J(t) = e^{-\Gamma t - i\varphi(t)} H(t)$, $U_J^*(t) = e^{-\Gamma t + i\varphi(t)} H^*(t)$, $W_J(t) = e^{-2\Gamma t} I(t)$.

The calculation of $N_J(z)$ is almost the same as the calculation in Sec. B.1. The matrix $M \equiv M_0 - \gamma_p M_1^2$ is

$$M = \begin{pmatrix} -\Gamma - \gamma_p & 0 & -ig_0 & ig_0 \\ 0 & -\Gamma - \gamma_p & ig_0 & -ig_0 \\ -ig_0 & ig_0 & -2\Gamma & 0 \\ ig_0 & -ig_0 & 0 & 0 \end{pmatrix}. \tag{B.10}$$

Then the matrix $N_J(z) \equiv z\mathbb{I} - M$ and its determinant are, respectively,

$$N_J(z) = \begin{pmatrix} z + \gamma_p + \Gamma & 0 & ig_0 & -ig_0 \\ 0 & z + \gamma_p + \Gamma & -ig_0 & ig_0 \\ ig_0 & -ig_0 & z + 2\Gamma & 0 \\ -ig_0 & ig_0 & 0 & z \end{pmatrix}$$

and

$$\det\left[N_J(z)\right] = (z + \gamma_p + \Gamma)\left[z\,(z + 2\Gamma)\,(z + \gamma_p + \Gamma) + 4g_0^2\,(z + \Gamma)\right], \tag{B.11}$$

which is the same as Eq. (B.3) provided that we change Γ to $-\Gamma$. So the roots of the secular equation of the matrix $N_J(z)$ are

$$\begin{aligned} z_1 &\approx -\Gamma - \gamma_p,\ z_2 \approx -\Gamma + \gamma_p \varepsilon + O\left[\left(\frac{\gamma_p}{g}\right)^3\right], \\ z_{3,4} &\approx -\Gamma - \frac{\gamma_p}{2}(1 + \varepsilon) \pm i2g + O\left[\left(\frac{\gamma_p}{g}\right)^2\right]. \end{aligned} \tag{B.12}$$

The inverse matrix to the matrix $N_J(z)$ is therefore

$$N_J^{-1}(z) = \frac{1}{\det\left[N_J(z)\right]} \begin{pmatrix} \bullet & \bullet & \bullet & \bullet \\ \bullet & \bullet & \bullet & \bullet \\ \bullet & \bullet & \bullet & \bullet \\ n_{41} & n_{42} & n_{43} & n_{44} \end{pmatrix}$$

with

$$\begin{aligned} n_{41} &= ig_0\left(z+2\Gamma\right)\left(z+\gamma_p+\Gamma\right), \\ n_{42} &= -ig_0\left(z+2\Gamma\right)\left(z+\gamma_p+\Gamma\right), \\ n_{43} &= 2g_0^2\left(z+\gamma_p+\Gamma\right), \\ n_{44} &= \left(z+\gamma_p+\Gamma\right)\left[\left(z+2\Gamma\right)\left(z+\gamma_p+\Gamma\right)+2g_0^2\right], \end{aligned}$$

where we only calculate the elements of the fourth row of $N_J^{-1}(z)$ because they are required to calculate $\langle J(t)\rangle$, which is then

$$\begin{aligned} \langle J(t)\rangle &= \int_C \frac{dz}{2\pi i} e^{zt} \frac{n_{44}}{\left(z-z_1\right)\left(z-z_2\right)\left(z-z_3\right)\left(z-z_4\right)} \\ &= \int_C \frac{dz}{2\pi i} e^{zt} \frac{\left(z+2\Gamma\right)\left(z+\Gamma+\gamma_p\right)+2g_0^2}{\left(z-z_2\right)\left(z-z_3\right)\left(z-z_4\right)} \\ &\approx \frac{g_0^2}{2g^2} e^{-[\Gamma+\gamma_p(1+\varepsilon)/2]t} \\ &\quad \times \left\{ e^{\gamma_p(1+3\varepsilon)t/2} - \left[\frac{\gamma_p}{4g} - \frac{g\left(\Gamma-\gamma_p/2\right)}{g_0^2}\right]\sin(2gt) - \left(1-\frac{2g^2}{g_0^2}\right)\cos(2gt)\right\}, \end{aligned} \tag{B.13}$$

where we have used the initial condition that $\langle \vec{v}_J(0)\rangle^T = (0,\, 0, 0, 1)$ and kept the order to $O\left(\gamma_p/g\right)$ and $O\left(\Gamma/g\right)$ in the coefficients and the order to $O\left(\gamma_p\varepsilon/g\right)$ in the exponential arguments.

B.3 Approximate Solution for $\langle H(t)\rangle$

In order to obtain the solution for $\langle H(t)\rangle$, we derive another equation of the type Eq. (5.5) with the definition of the vector $[\vec{v}_H(t)]^T = [H(t),\, U_H(t),\, W_H(t),\, Z_H(t)]$, and the following matrices:

$$M_1 = \begin{pmatrix} 0 & 0 & 0 & 0 \\ 0 & 2 & 0 & 0 \\ 0 & 0 & 1 & 0 \\ 0 & 0 & 0 & 1 \end{pmatrix}, \; M_0 = \begin{pmatrix} 0 & 0 & -ig_0 & ig_0 \\ 0 & 0 & ig_0 & -ig_0 \\ -ig_0 & ig_0 & -\Gamma & 0 \\ ig_0 & -ig_0 & 0 & \Gamma \end{pmatrix}$$

and with the initial condition $\langle \vec{v}_H(0) \rangle^T = (0,0,0,1)$, where $U_H(t) = e^{i2\varphi(t)} H^*(t)$, $W_H(t) = e^{-\Gamma t + i\varphi(t)} I(t)$, $Z_H(t) = e^{\Gamma t + i\varphi(t)} J(t)$. The matrix M for the vector $\vec{v}_H(t)$ is

$$M = M_0 - \gamma_p M_1^2 = \begin{pmatrix} 0 & 0 & -ig_0 & ig_0 \\ 0 & -4\gamma_p & ig_0 & -ig_0 \\ -ig_0 & ig_0 & -\Gamma - \gamma_p & 0 \\ ig_0 & -ig_0 & 0 & \Gamma - \gamma_p \end{pmatrix}.$$

Therefore

$$N_H(z) = \begin{pmatrix} z & 0 & ig_0 & -ig_0 \\ 0 & z + 4\gamma_p & -ig_0 & ig_0 \\ ig_0 & -ig_0 & z + (\Gamma + \gamma_p) & 0 \\ -ig_0 & ig_0 & 0 & z - (\Gamma - \gamma_p) \end{pmatrix}$$

and the determinant of the matrix $N_H(z)$ is

$$\det[N_H(z)] = z(z + 4\gamma_p) \left[(z + \gamma_p)^2 - \Gamma^2 \right] + 4g_0^2 (z + \gamma_p)(z + 2\gamma_p). \tag{B.14}$$

The secular equation is given by setting $\det[N_H(z)] = 0$, which gives

$$(z + \gamma_p)^2 (z + 2\gamma_p)^2 + 4g_0^2 (z + \gamma_p)(z + 2\gamma_p) - \Gamma^2 (z + 2\gamma_p)^2 - 4\gamma_p^2 (z + \gamma_p)^2 = -4\gamma_p^2 \Gamma^2. \tag{B.15}$$

In the most general case, no simple factorizations occur, and a quartic equation must be solved. Again the roots are implicit in the general case [209], but explicit in the strong-coupling regime. Similarly, there are two kinds of roots in the strong-coupling regime. The first of these follows from the assumption that both $(z + \gamma_p)^2$ and $(z + 2\gamma_p)^2$ are small compared with $(4g_0^2 - \Gamma^2)$, in which case it is natural to rearrange Eq. (B.15) into the form

$$(z + \gamma_p)(z + 2\gamma_p) \left[(z + \gamma_p)(z + 2\gamma_p) + (4g_0^2 - \Gamma^2 - 4\gamma_p^2) \right] \approx -4\gamma_p^2 \Gamma^2, \tag{B.16}$$

where we used the assumptions $(4g_0^2 - \Gamma^2) \gg \Gamma^2, \gamma_p^2$, $\left| \frac{z + 2\gamma_p}{z + \gamma_p} \right| \approx 1$ and $\left| \frac{z + \gamma_p}{z + 2\gamma_p} \right| \approx 1$. Then

$$(z + \gamma_p)(z + 2\gamma_p) \approx \frac{-4\gamma_p^2 \Gamma^2}{4g_0^2 - \Gamma^2 - 4\gamma_p^2} \left[1 + \frac{(z + \gamma_p)(z + 2\gamma_p)}{4g_0^2 - \Gamma^2 - 4\gamma_p^2} \right]^{-1}, \tag{B.17}$$

which is solved by iteration. The roots are

$$\begin{aligned} z_1 &\approx -\gamma_p(1+4\varepsilon) + O\left[\left(\frac{\gamma_p}{g}\right)^3\right] \\ z_2 &\approx -2\gamma_p(1-2\varepsilon) + O\left[\left(\frac{\gamma_p}{g}\right)^3\right]. \end{aligned} \tag{B.18}$$

The second kind of root occurs if $(z+\gamma_p)(z+2\gamma_p)$ is as large as $\left(4g_0^2-\Gamma^2\right)$, but has the opposite sign. Then the alternative rearrangement of Eq. (B.15) is

$$(z+\gamma_p)(z+2\gamma_p) + \left(4g_0^2-\Gamma^2-4\gamma_p^2\right) \approx \gamma_p\Gamma^2\left[\frac{z-2\gamma_p}{(z+\gamma_p)(z+2\gamma_p)}\right]. \tag{B.19}$$

To first order in γ_p the factor $(z+\gamma_p)(z+2\gamma_p)$ on the right hand side of Eq. (B.20) can be replaced by $-\left(4g_0^2-\Gamma^2\right)$. This gives a simple quadratic equation for z, $z^2+\gamma_p(3+\varepsilon)z+4g^2-4\gamma_p^2+2\gamma_p^2(1-\varepsilon)=0$, whose solutions are the third and fourth roots

$$\begin{aligned} z_{3,4} &\approx -\frac{\gamma_p}{2}(3+\varepsilon) \pm i2g\sqrt{1-(\gamma_p/g)^2} + O\left[\left(\frac{\gamma_p}{g}\right)^2\right] \\ &\approx -\frac{\gamma_p}{2}(3+\varepsilon) \pm i2g + O\left[\left(\frac{\gamma_p}{g}\right)^2\right]. \end{aligned} \tag{B.20}$$

The inverse matrix to $N_H(z)$ is

$$N_H^{-1}(z) = \frac{1}{\det[N(z)]}\begin{pmatrix} n_{11} & n_{12} & n_{13} & n_{14} \\ \bullet & \bullet & \bullet & \bullet \\ \bullet & \bullet & \bullet & \bullet \\ \bullet & \bullet & \bullet & \bullet \end{pmatrix},$$

with

$$\begin{aligned} n_{11} &= (z+4\gamma_p)\left[(z+\gamma_p)^2-\Gamma^2\right] + 2g_0^2(z+\gamma_p), \\ n_{12} &= 0, \\ n_{13} &= -ig_0(z+4\gamma_p)(z+\gamma_p-\Gamma), \\ n_{14} &= ig_0(z+4\gamma_p)(z+\gamma_p+\Gamma). \end{aligned}$$

Therefore $\langle H(t)\rangle$ is given by

$$\begin{aligned}\langle H(t)\rangle &= \int_C \frac{dz}{2\pi i} e^{zt} \frac{n_{14}}{(z-z_1)(z-z_2)(z-z_3)(z-z_4)} \\ &= \int_C \frac{dz}{2\pi i} e^{zt} \frac{ig_0(z+4\gamma_p)(z+\gamma_p+\Gamma)}{(z-z_1)(z-z_2)(z-z_3)(z-z_4)} \\ &\approx \frac{ig_0}{2g} e^{-\gamma_p(3+\varepsilon)t/2} \\ &\quad \times \left[\frac{3\Gamma}{2g} e^{\gamma_p(1-7\varepsilon)t/2} - \frac{\Gamma-\gamma_p}{g} e^{-\gamma_p(1-9\varepsilon)t/2} - \frac{\Gamma+2\gamma_p}{2g}\cos(2gt) + \sin(2gt)\right],\end{aligned} \tag{B.21}$$

where we have used the initial condition that $\langle \vec{v}_H(0)\rangle^T = (0, 0, 0, 1)$ and kept the order to $O(\gamma_p/g)$ and $O(\Gamma/g)$ in the coefficients and the order to $O(\gamma_p\varepsilon/g)$ in the exponential arguments.

BIBLIOGRAPHY

[1] C. Fabry and A. Pérot, "Sur les franges des lames minces argentées et leur application á la mesure de petites épaisseurs d'air," Ann. Chim. Phys. **12**, 459 (1897).

[2] R. K. Chang and A. J. Campillo, eds., *Optical Processes in Microcavities* (World Scientific, Singapore, 1996).

[3] C. Wilmsen, H. Temkin, and L. A. Coldren, *Vertical-Cavity Surface-Emitting Lasers : Design, Fabrication, Characterization, and Applications* (Cambridge University Press, New York, 1999).

[4] K. Vahala, ed., *Optical Microcavities* (World Scientific, Singapore, 2004).

[5] H. J. Kimble, "Structure and dynamics in cavity quantum electrodynamics," in *Cavity Quantum Electrodynamics*, P. R. Berman, ed. (Academic Press, San Diego, 1994), pp. 203–266.

[6] G. Cui, J. M. Hannigan, R. Loeckenhoff, F. M. Matinaga, M. G. Raymer, S. Bhongale, M. Holland, S. Mosor, S. Chatterjee, H. M. Gibbs, and G. Khitrova, "A hemispherical, high-solid-angle optical micro-cavity for cavity-QED studies," Opt. Express **14**, 2289 (2006).

[7] V. B. Braginsky, M. L. Gorodetsky, and V. S. Ilchenko, "Quality-factor and nonlinear properties of optical whispering-gallery modes," Phys. Lett. A **137**, 393 (1989).

[8] E. Yablonovitch, "Inhibited spontaneous emission in solid-state physics and electronics," Phys. Rev. Lett. **58**, 2059 (1987).

[9] M. L. Gorodetsky, A. A. Savchenkov, and V. S. Ilchenko, "Ultimate Q of optical microsphere resonators," Opt. Lett. **21**, 453 (1996).

[10] D. K. Armani, T. J. Kippenberg, S. M. Spillane, and K. J. Vahala, "Ultra-high-Q toroid microcavity on a chip," Nature **421**, 925 (2003).

[11] O. Painter, R. K. Lee, A. Scherer, A. Yariv, J. D. O'Brien, P. D. Dapkus, and I. Kim, "Two-dimensional photonic band-gap defect mode laser," Science **284**, 1819 (1999).

[12] J. Vuckovic, M. Loncar, H. Mabuchi, and A. Scherer, "Design of photonic crystal microcavities for cavity QED," Phys. Rev. E **65**, 016 608 (2002).

[13] K. Srinivasan and O. Painter, "Momentum space design of high-Q photonic crystal optical cavities," Opt. Express **10**, 670 (2002).

[14] S. Lacey, H. Wang, D. Foster, and J. Noeckel, "Directional evanescent escape from nearly spherical optical resonators," Phys. Rev. Lett. **91**, 033 902 (2003).

[15] C. J. Hood, H. J. Kimble, and J. Ye, "Characterization of high-finesse mirrors: Loss, phase shifts, and mode structure in an optical cavity," Phys. Rev. A **64**, 033 806 (2003).

[16] P. R. Berman, ed., *Cavity Quantum Electrodynamics* (Academic Press, Boston, 1994).

[17] J. M. Raimond, M. Brune, and S. Haroche, "Colloquium: Manipulating quantum entanglement with atoms and photons in a cavity," Rev. Mod. Phys. **73**, 565 (2001).

[18] H. Mabuchi and A. C. Doherty, "Cavity quantum electrodynamics: coherence in context," Science **298**, 1372 (2002).

[19] S. J. van Enk, H. J. Kimble, and H. Mabuchi, "Quantum information processing in cavity-QED," Quantum Infomation Processing **3**, 75 (2004).

[20] N. Gisin, G. Ribordy, W. Tittel, and H. Zbinden, "Quantum cryptography," Rev. Mod. Phys. **74**, 145 (2002).

[21] G. Brassard, N. Lutkenhaus, T. Mor, and B. Sanders, "Limitations on practical quantum cryptography," Phys. Rev. Lett. **85**, 1330 (2000).

[22] N. Lütkenhaus, "Security against individual attacks for realistic quantum key distribution," Phys. Rev. A **61**, 052 304 (2000).

[23] D. Bouwmeester, J.-W. Pan, K. Mattle, M. Eibl, H. Weinfurter, and A. Zeilinger, "Experimental quantum teleportation," Nature **390**, 575 (1997).

[24] H.-J. Briegel, W. Dür, J. I. Cirac, and P. Zoller, "Quantum repeaters: the role of imperfect local operations in quantum communication," Phys. Rev. Lett. **81**, 5932 (1998).

[25] E. Knill, R. Laflamme, and G. J. Milburn, "A scheme for efficient quantum computation with linear optics," Nature **409**, 46 (2001).

[26] M. Xiao, L.-A. Wu, and H. J. Kimble, "Precision measurement beyond the shot-noise limit," Phys. Rev. Lett. **59**, 278 (1987).

[27] E. S. Polzik, J. Carri, and H. J. Kimble, "Spectroscopy with squeezed light," Phys. Rev. Lett. **68**, 3020 (1992).

[28] V. Giovannetti, S. Lloyd, and L. Maccone, "Quantum-enhanced measurements: beating the standard quantum limit," Science **306**, 1330 (2004).

[29] J. G. Rarity, P. C. M. Owens, and P. R. Tapster, "Quantum random-number generation and key sharing," J. Mod. Opt **41**, 2435 (1994).

[30] G. Khitrova, H. M. Gibbs, F. Jahnke, M. Kira, and S. W. Koch, "Nonlinear optics of normal-mode-coupling semiconductor microcavities," Rev. Mod. Phys. **71**, 1591 (1999).

[31] Y. Yamamoto, F. Tassone, and H. Cao, *Semiconductor Cavity Quantum Electrodynamics* (Springer, New York, 2000).

[32] A. J. Shields, "Semiconductor quantum light sources," Nature Photonics **1**, 215 (2007).

[33] J. F. Clauser, "Experimental distinction between the quantum and classical field-theoretical prediction for the photoelectric effect," Phys. Rev. D **9**, 853 (1974).

[34] F. Diedrich and H. Walther, "Nonclassical radiation of single stored ion," Phys. Rev. Lett. **58**, 203 (1987).

[35] T. Basche, W. E. Moerner, M. Orrit, and H. Talon, "Photon antibunching in the fluorescence of a single dye molecule trapped in a solid," Phys. Rev. Lett. **69**, 1516 (1992).

[36] C. Kurtsiefer, S. Mayer, P. Zarda, and H. Weinfurter, "Stable solid-state source of single photons," Phys. Rev. Lett. **85**, 290 (2000).

[37] P. Michler, A. Kiraz, C. Becher, W. V. Schoenfeld, P. M. Petroff, L. Zhang, E. Hu, and A. Imamoglu, "A quantum dot single-photon turnstile device," Science **290**, 2282 (2000).

[38] C. Santori, M. Pelton, G. Solomon, Y. Dale, and Y. Yamamoto, "Triggered single photons from a quantum dot," Phys. Rev. Lett. **86**, 1502 (2001).

[39] Z. Yuan, B. E. Kardynal, R. M. Stevenson, A. J. Shields, C. J. Lobo, K. Cooper, N. S. Beattie, D. A. Ritchie, and M. Pepper, "Electrically driven single-photon source," Science **295**, 102 (2002).

[40] C. Santori, "Quantum optics: A brighter source of single photons," Nature Photonics **1**, 686 (2007).

[41] S. Strauf, N. G. Stoltz, M. T. Rakher, L. A. Coldren, P. M. Petroff, and D. Bouwmeester, "High-frequency single-photon source with polarization control," Nature Photonics **1**, 704 (2007).

[42] D. Press, S. Gotzinger, S. Reitzenstein, C. Hofmann, A. Loffler, M. Kamp, A. Forchel, and Y. Yamamoto, "Photon antibunching from a single quantum-dot-microcavity system in the strong coupling regime," Phys. Rev. Lett. **98**, 117402 (2007).

[43] J. M. Hannigan, "Cavity-QED strong-coupling between a semiconductor quantum dot and a micro-cavity," Ph.D. thesis, University of Oregon, Eugene, OR, USA (2008).

[44] J. P. Reithmaier, G. Sek, A. Loffler, C. Hofmann, S. Kuhn, S. Reitzenstein, L. V. Keldysh, V. D. Kulakovskii, T. L. Reinecke, and A. Forchel, "Strong coupling in a single quantum dot-semiconductor microcavity system," Nature **432**, 197 (2004).

[45] T. Yoshie, A. Scherer, J. Hendrickson, G. Khitrova, H. M. Gibbs, G. Rupper, C. Ell, O. B. Shchekin, and D. G. Deppe, "Vacuum Rabi splitting with a single quantum dot in a photonic crystal nanocavity," Nature **432**, 200 (2004).

[46] N. L. Thomas, U. Woggon, O. Schöps, M. V. Artemyev, M. Kazes, and U. Banin, "Cavity QED with semiconductor nanocrystals," Nano Lett. **6**, 557 (2006).

[47] E. Peter, P. Senellart, D. Martrou, A. Lemaitre, J. Hours, J. M. Gerard, and J. Bloch, "Exciton-photon strong-coupling regime for a single quantum dot embedded in a microcavity," Phys. Rev. Lett. **95**, 067401 (2005).

[48] K. Srinivasan and O. Painter, "Linear and nonlinear optical spectroscopy of a strongly-coupled microdisk-quantum dot system," `arXiv:0707.3311v2 [quant-ph]`.

[49] X. Fan, T. Takagahara, J. E. Cunningham, and H. Wang, "Pure dephasing induced by exciton-phonon interactions in narrow GaAs quantum wells," Solid State Commun. **108**, 857 (1998).

[50] M. Bayer and A. Forchel, "Temperature dependence of the exciton homogeneous linewidth in $In_{0.6}Ga_{0.4}As/GaAs$ self-assembled quantum dots," Phys. Rev. B **65**, 041308(R) (2002).

[51] G. Cui and M. G. Raymer, "Quantum efficiency of single-photon sources in the cavity-QED strong-coupling regime," Opt. Express **13**, 9660 (2005).

[52] G. Cui and M. G. Raymer, "Emission spectra and quantum efficiency of single-photon sources in the cavity-QED strong-coupling regime," Phys. Rev. A **73**, 053 807 (2006).

[53] M. Trupke, J. Goldwin, B. Darquié, G. Dutier, S. Eriksson, J. Ashmore, and E. A. Hinds, "Atom detection and photon production in a scalable, open, optical microcavity," Phys. Rev. Lett. **99**, 063 601 (2007).

[54] T. P. Purdy and D. M. Stamper-Kurn, "Integrating cavity quantum electrodynamics and ultracold-atom chips with on-chip dielectric mirrors and temperature stabilization," Appl. Phys. B **90**, 401 (2008).

[55] M. Planck, "On the theory of the energy distribution law of the normal spectrum," Verh. dtsch. phys. Ges. Berlin **2**, 237 (1900).

[56] A. Einstein, "Photoelectric effect," Ann. Phys. **17**, 132 (1905).

[57] W. E. Lamb, "Anti-photon," Appl. Phys. B **60**, 77 (1995).

[58] A. Einstein, "Zur Quantentheorie der Strahlung (On the Quantum Theory of Radiation)," Physikalische Gesellschaft Zurich. Mitteilungen **18**, 220 (1916).

[59] T. H. Maiman, "Stimulated optical radiation in ruby," Nature **187**, 493 (1960).

[60] N. G. Basov, B. M. Vul, and Y. M. Popov, "Quantum-mechanical semiconductor generators and amplifiers of electromagnetic oscillations," J. Exptl. Theoret. Phys. (USSR) **37**, 587 (1959).

[61] R. N. Hall, G. E. Fenner, J. D. Kingsley, T. J. Soltys, and R. O. Carlson, "Coherent light emission from GaAs junctions," Phys. Rev. Lett. **9**, 366 (1962).

[62] Z. I. Alferov, V. M. Andreev, E. L. Portnoi, and M. K. Trukan, "AlAs-GaAs heterojunction injection lasers with a low room-temperature threshold," Fiz. Tekh. Poluprov. **3**, 1328 (1969).

[63] M. B. Panish, I. Hayashi, and S. Sumski, "Double-heterostructure injection lasers with room-temperature thresholds as low as 2300 A/cm^2," Appl. Phys. Lett. **16**, 326 (1970).

[64] R. J. Glauber, "The Quantum Theory of Optical Coherence," Phys. Rev. **130**, 2529 (1963).

[65] R. J. Glauber, *Quantum Theory of Optical Coherence: Selected Papers and Lectures* (Wiley-VCH, Weinheim, Germany, 2007).

[66] K. Garay-Palmett, H. J. McGuinness, O. Cohen, J. S. Lundeen, R. Rangel-Rojo, A. B. U'Ren, M. G. Raymer, C. J. McKinstrie, S. Radic, and I. A. Walmsley, "Photon pair-state preparation with tailored spectral properties by spontaneous four-wave mixing in photonic-crystal fiber," arXiv:0709.3129.

[67] D. F. Walls, "Evidence for the quantum nature of light," Nature **280**, 451 (1979).

[68] H. J. Kimble, M. Dagenais, and L. Mandel, "Photon antibunching in resonance fluorescence," Phys. Rev. Lett. **39**, 691 (1977).

[69] D. C. Burnham and D. L. Weinberg, "Observation of simultaneity in parametric production of optical photon pairs," Phys. Rev. Lett. **25**, 84 (1970).

[70] C. K. Hong and L. Mandel, "Experimental realization of a localized one-photon state," Phys. Rev. Lett. **56**, 58 (1986).

[71] Z. Y. O. C. K. Hong and L. Mandel, "Measurement of subpicosecond time intervals between two photons by interference," Phys. Rev. Lett. **59**, 2044 (1987).

[72] Z. Y. Ou and L. Mandel, "Violation of Bell's inequality and classical probability in a two-photon correlation experiment," Phys. Rev. Lett. **61**, 50 (1988).

[73] Y. H. Shih and C. O. Alley, "New type of Einstein-Podolsky-Rosen-Bohm experiment using pairs of light quanta produced by optical parametric down conversion," Phys. Rev. Lett. **61**, 2921 (1988).

[74] Y. H. Shih and A. V. Sergienko, "Observation of quantum beating in a simple beam-splitting experiment: Two-particle entanglement in spin and space-time," Phys. Rev. A **50**, 2564 (1994).

[75] P. G. Kwiat, K. Mattle, H. Weinfurter, A. Zeilinger, A. V. Sergienko, and Y. Shih, "New high-intensity source of polarization-entangled photon pairs," Phys. Rev. Lett. **75**, 4337 (1995).

[76] S. Fasel, O. Alibart, S. Tanzilli, P. Baldi, A. Beveratos, N. Gisin, and H. Zbinden, "High-quality asynchronous heralded single-photon source at telecom wavelength," New J. Phys. **6**, 163 (2004).

[77] K. Edamatsu, G. Oohata, R. Shimizu, and T. Itoh, "Generation of ultraviolet entangled photons in a semiconductor," Nature **431**, 167 (2004).

[78] M. Orrit and J. Bernard, "Single pentacene molecules detected by fluorescence excitation in a p-terphenyl crystal," Phys. Rev. Lett. **65**, 2716 (1990).

[79] L. Birotheau, A. Izrael, J. Y. Marzin, R. Azoulay, V. Thierry-Mieg, and F. R. Ladan, "Optical investigation of the one-dimensional confinement effects in narrow GaAs/GaAlAs quantum wires," Appl. Phys. Lett. **61**, 3023 (1992).

[80] K. Brunner, U. Bockelmann, G. Abstreiter, M. Walther, G. Böhm, G. Tränkle, and G. Weimann, "Photoluminescence from a single GaAs/AlGaAs quantum dot," Phys. Rev. Lett. **69**, 3216 (1992).

[81] F. De Martini, G. Di Giuseppe, and M. Marrocco, "Single-mode generation of quantum photon states by excited single molecules in a microcavity trap," Phys. Rev. Lett. **76**, 900 (1996).

[82] S. C. Kitson, P. Jonsson, J. G. Rarity, and P. R. Tapster, "Intensity fluctuation spectroscopy of small numbers of dye molecules in a microcavity," Phys. Rev. A **58**, 620 (1998).

[83] B. Lounis and W. E. Moerner, "Single photons on demand from a single molecule at room temperature," Nature **407**, 491 (2000).

[84] P. Michler, A. Imamoglu, M. D. Mason, P. J. Carson, G. F. Strouse, and S. K. Buratto, "Quantum correlation among photons from a single quantum dot at room temperature," Nature **406**, 968 (2000).

[85] G. Messin, J. P. Hermier, E. Giacobino, P. Desbiolles, and M. Dahan, "Bunching and antibunching in the fluorescence of semiconductor nanocrystals," Opt. Lett. **26**, 1891 (2001).

[86] R. Brouri, A. Beveratos, J.-P. Poizat, and P. Grangier, "Photon antibunching in the fluorescence of individual color centers in diamond," Opt. Lett. **25**, 1294 (2000).

[87] E. M. Purcell, "Spontaneous emission probabilities at radio frequencies (Abstract)," Phys. Rev. **69**, 681 (1946).

[88] D. Kleppner, "Inhibited spontaneous emission," Phys. Rev. Lett. **47**, 233 (1981).

[89] R. H. Brown and R. Q. Twiss, "Correlation between photons in two coherent beams of light," Nature **177**, 27 (1956).

[90] D. T. Smithey, M. Beck, M. G. Raymer, and A. Faridani, "Measurement of the Wigner distribution and the density matrix of a light mode using optical homodyne tomography: Application to squeezed states and the vacuum," Phys. Rev. Lett. **70**, 1244 (1993).

[91] C. Santori, D. Fattal, J. Vuckovic, G. S. Solomon, and Y. Yamamoto, "Indistinguishable photons from a single-photon device," Nature **419**, 594 (2002).

[92] A. Kuhn, M. Hennrich, and G. Rempe, "Deterministic single-photon source for distributed quantum networking," Phys. Rev. Lett. **89**, 067901 (2002).

[93] J. McKeever, A. Boca, A. D. Boozer, R. Miller, J. R. Buck, A. Kuzmich, and H. J. Kimble, "Deterministic generation of single photons from one atom trapped in a cavity," Science **303**, 1992 (2004).

[94] K. M. Birnbaum, A. Boca, R. Miller, A. D. Boozer, T. E. Northup, and H. J. Kimble, "Photon blockade in an optical cavity with one trapped atom," Nature **436**, 87 (2005).

[95] A. Kiraz, M. Atatüre, and A. Imamŏglu, "Quantum-dot single-photon sources: Prospects for applicaitons in linear optics quantum-information processing," Phys. Rev. A **69**, 032305 (2004).

[96] A. E. Siegman, *Lasers* (University Science Books, Mill Valley, CA, 1986).

[97] D. H. Foster and J. U. Nöckel, "Methods for 3-d vector microcavity problems involving a planar dielectric mirror," Opt. Commun. **234**, 351 (2004).

[98] D. H. Foster, "Fabry-Pérot and whispering gallery modes in realistic resonator models," Ph.D. thesis, University of Oregon, Eugene, OR, USA (2006).

[99] K. Brunner, G. Abstreiter, G. Bóhm, G. Tránkle, and G. Weimann, "Sharp-line photoluminescence and two-photon absorption of zero-dimensional biexcitons in a GaAs/AlGaAs structure," Phys. Rev. Lett. **73**, 1138 (1994).

[100] A. Zrenner, L. V. Butov, M. Hagn, G. Abstreiter, G. Bohm, and G. Weimann, "Quantum dots formed by interface fluctuations in AlAs/GaAs coupled quantum well structures," Phys. Rev. Lett. **72**, 3382 (1994).

[101] D. Gammon, E. S. Snow, B. V. Shanabrook, D. S. Katzer, and D. Park, "Homogeneous linewidths in the optical spectrum of a single gallium arsenide duantum dot," Science **273**, 87 (1996).

[102] P. M. Petroff and S. P. DenBaars, "MBE and MOCVD growth and properties of self-assembling quantum dot arrays in III-V semiconductor structures," Superlattices and Microstructres **15**, 15 (1994).

[103] R. Nötzel, "Self-organized growth of quantum-dot structures," Semicond. Sci.Tech. **10**, 1365 (1996).

[104] P. M. Petroff, A. Lorke, and A. Imamoglu, "Epitaxially self-assembled quantum dots," Phys. Today **54**, 46 (2001).

[105] W. Wegscheider, G. Schedelbeck, G. Abstreiter, M. Rother, and M. Bichler, "Atomically precise GaAs/AlGaAs auantum dots fabricated by twofold cleaved edge overgrowth," Phys. Rev. Lett. **79**, 1917 (1997).

[106] U. Bockelmann, W. Heller, A. Filoramo, and P. Roussignol, "Microphotoluminescence studies of single quantum dots. I. Time-resolved experiments," Phys. Rev. B **55**, 4456 (1997).

[107] A. P. Alivisatos, "Semiconductor clusters, nanocrystals, and quantum dots," Science **271**, 933 (1996).

[108] A. M. A. Eychmüller and H. Weller, "A quantum dot quantum well: CdS/HgS/CdS," Chem. Phys. Lett. **208**, 59 (1993).

[109] M. A. Hines and P. Guyot-Sionnest, "Synthesis and characterization of strongly luminescing ZnS-capped CdSe nanocrystals," J. Phys. Chem. **100**, 468 (1996).

[110] X. Peng, M. C. Schlamp, A. V. Kadavanich, and A. P. Alivisatos, "Epitaxial growth of highly luminescent CdSe/CdS core/shell nanocrystals with photostability and electronic accessibility," J. Am. Chem. Soc. **119**, 7019 (1997).

[111] D. Gammon, E. S. Snow, B. V. Shanabrook, D. S. Katzer, and D. Park, "Fine structure splitting in the optical spectra of single GaAs quantum dots," Phys. Rev. Lett. **76**, 3005 (1996).

[112] D. Gammon, "High resolution spectroscopy of individual quantum dots in wells," MRS Bul. **23**, 44 (1998).

[113] G. H. Wannier, "The structure of electronic excitation levels in insulating crystals," Phys. Rev. **52**, 191 (1937).

[114] L. J. Sham and T. M. Rice, "Many-particle derivation of the effective-mass equation for the Wannier exciton," Phys. Rev. **144**, 708 (1966).

[115] J. Frenkel, "On the transformation of light into heat in solids. I," Phys. Rev. **37**, 17 (1931).

[116] G. Chen, T. H. Stievater, J. R. Guest, D. G. Steel, D. Gammon, P. Chen, C. Piermarocchi, and L. J. Sham, "Coherent optical spectroscopy and manipulation of single quantum dots," in *Quantum Coherence, Correlation and Decoherence in Semiconductor Nanostructures*, T. Takagahara, ed. (Academic Press, San Diego, 2003), pp. 281–365.

[117] T. Östreich, K. Schönhammer, and L. J. Sham, "Exciton-exciton correlation in the nonlinear optical regime," Phys. Rev. Lett. **74**, 4698 (1995).

[118] S. W. Brown, T. A. Kennedy, D. Gammon, and E. S. Snow, "Spectrally resolved Overhauser shifts in single GaAs/$Al_xGa_{1-x}As$ quantum dots," Phys. Rev. B **54**, R17 339 (1996).

[119] L. Besombes, K. Kheng, and D. Martrou, "Exciton and biexciton fine structure in single elongated islands grown on a vicinal surface," Phys. Rev. Lett. **85**, 425 (2000).

[120] T. Tanaka, J. Singh, Y. Arakawa, and P. Bhattacharya, "Near band edge polarization dependence as a probe of structural symmetry in GaAs/AlGaAs quantum dot structures," Appl. Phys. Lett. **62**, 756 (1993).

[121] V. D. Kulakovskii, G. Bacher, R. Weigand, T. Kümmell, A. Forchel, E. Borovitskaya, K. Leonardi, and D. Hommel, "Fine structure of biexciton emission in symmetric and asymmetric CdSe/ZnSe single quantum dots," Phys. Rev. Lett. **82**, 1780 (1999).

[122] S. V. Gupalov, E. L. Ivchenko, and A. V. Kavokin, "Fine structure of localized exciton levels in quantum wells," JETP **86**, 388 (1998).

[123] R. M. Stevenson, R. J. Young, P. Atkinson, K. Cooper, D. A. Ritchie, and A. J. Shields, "A semiconductor source of triggered entangled photon pairs," Nature **439**, 179 (2006).

[124] E. Spiller, "Multilayer optics for X-rays," in *Physics, Fabrication, and Applications of Multilayered Structures*, P. Dhez and C. Weisbuch, eds. (Plenum Press, New York, 1988), pp. 271–309.

[125] G. Björk and Y. Yamamoto, "Spontaneous emission in dielectric planar microcavities," in *Spontaneous Emission and Laser Oscillation in Microcavities*, H. Yokoyama and K. Ujihara, eds. (CRC Press, Inc., Boca Raton, Florida, 1995), pp. 189–235.

[126] C. Weisbuch, R. Houdré, and R. P. Stanley, "Microcavities and semiconductors: the strong-coupling regime," in *Spontaneous Emission and Laser Oscillation in Microcavities*, H. Yokoyama and K. Ujihara, eds. (CRC Press, Inc., Boca Raton, Florida, 1995), pp. 109–150.

[127] V. Savona, "Linear optical properties of smiconductor microcavities with embedded quantum wells," in *Confined Photon Systems: Fundamentals and Applications*, H. Benisty, J.-M. Gérard, R. Houdré, J. Rarity, and C. Weisbuch, eds. (Springer-Verlag, Berlin, 1999), pp. 173–242.

[128] R. G. Hulet, E. S. Hilfer, and D. Kleppner, "Inhibited spontaneous emission by a Rydberg atom," Phys. Rev. Lett. **55**, 2137 (1985).

[129] F. De Martini, G. Innocenti, G. R. Jacobovitz, and P. Mataloni, "Anomalous spontaneous emission time in a microscopic optical cavity," Phys. Rev. Lett. **59**, 2955 (1987).

[130] D. J. Heinzen, J. J. Childs, J. E. Thomas, and M. S. Feld, "Enhanced and inhibited visible spontaneous emission by atoms in a confocal resonator," Phys. Rev. Lett. **58**, 1320 (1987).

[131] D. J. Heinzen and M. S. Feld, "Vacuum radiative level shift and spontaneous-emission linewidth of an atom in an optical resonator," Phys. Rev. Lett. **59**, 2623 (1987).

[132] S. E. Morin, C. C. Yu, and T. W. Mossberg, "Strong atom-cavity coupling over large volumes and the observation of subnatural intracavity atomic linewidths," Phys. Rev. Lett. **73**, 1489 (1994).

[133] Y. Yamamoto and R. E. Slusher, "Optical processes in microcavities," Phys. Today **46**, 66 (1993).

[134] P. R. Rice and H. J. Carmichael, "Photon statistics of a cavity-QED laser: a comment on the laser-phase-transition analogy," Phys. Rev. A **50**, 4318 (1994).

[135] Q. A. Turchette, C. J. Hood, W. Lange, H. Mabuchi, and H. J. Kimble, "Measurement of conditional phase shifts for quantum logic," Phys. Rev. Lett. **75**, 4710 (1995).

[136] S. Parkins, D. Walls, and A. Imamoğlu, "Single-photon nonlinear optics and quantum control," in *Directions in Quantum Optics: A Collection of Papers Dedicated to the Memory of Dan Walls*, H. J. Carmichael, R. J. Glauber, and M. O. Scully, eds. (Springer, New York, 2001), pp. 217–229.

[137] D. Meschede, H. Walther, and G. Müller, "One-atom maser," Phys. Rev. Lett. **54**, 551 (1985).

[138] M. Brune, J. M. Raimond, L. D. P. Goy, and S. Haroche, "Realization of a two-photon maser oscillator," Phys. Rev. Lett. **59**, 1899 (1987).

[139] G. Rempe, R. J. Thompson, R. J. Brecha, W. D. Lee, and H. J. Kimble, "Optical bistability and photon statistics in cavity quantum electrodynamics," Phys. Rev. Lett. **67**, 1727 (1991).

[140] S. Haroche and D. Kleppner, "Cavity quantum electrodynamics," Phys. Today **42**, 24 (1989).

[141] C. Weisbuch, M. Nishioka, A. Ishikawa, and Y. Arakawa, "Observation of the coupled exciton-photon mode splitting in a semiconductor quantum microcavity," Phys. Rev. Lett. **69**, 3314 (1992).

[142] "Spectrum Thin Films," URL `http://www.spectrumthinfilms.com/`.

[143] M. Trupke, E. A. Hinds, S. Eriksson, E. A. Curtis, Z. Moktadir, E. Kukharenka, and M. Kraft, "Microfabricated high-finesse optical cavity with open access and small volume," Appl. Phys. Lett. **87**, 211 106 (2005).

[144] "Wyko Optical Profiler," URL `http://www.veeco.com/`.

[145] M. Born and E. Wolf, *Principles of Optics*, 7th ed. (Cambridge University Press, New York, 1999), Ch. 7.5.5 The Twyman–Green and related interferometers, pp. 336–341.

[146] R. Loeckenhoff, "Production and application of a 50 μm hemispherical cavity," Unpublihsed lab report. `University of Oregon, 2002`.

[147] R. P. Stanley, R. Houdre, U. Oesterle, M. Gailhanou, and M. Ilegems, "Ultrahigh finesse microcavity with distributed Bragg reflectors," Appl. Phys. Lett. **65**, 1883 (1994).

[148] J. J. LePore, "An improved technique for selective etching of GaAs and $Ga_{1-x}Al_xAs$," J. Appl. Phys. **51**, 6441 (1980).

[149] R. W. P. Drever, J. L. Hall, F. V. Kowalski, J. Hough, G. M. Ford, A. J. Munley, and H. Ward, "Laser phase and frequency stabilization using an optical resonator," Appl. Phys. B **31**, 97 (1983).

[150] E. D. Black, "An introduction to Pound-Drever-Hall laser frequency stabilization," Am. J. Phys. **69**, 79 (2001).

[151] D. Z. Anderson, "Alignment of resonant optical cavities," Appl. Optics **23**, 2944 (1984).

[152] S. Bhongale, M. Holland, and M. G. Raymer, "Quantum dot quantum computing: non-paraxial eigenmodes of microcavity," presented at the APS 34th Meeting of the Division of AMO Physics, Boulder, CO, 20-24 May 2003.

[153] L. C. Andreani, G. Panzarini, and J. M. Gerard, "Strong-coupling regime for quantum boxes in pillar microcavities: theory," Phys. Rev. B **60**, 13 276 (1999).

[154] J. Vuckovic, M. Pelton, A. Scherer, and Y. Yamamoto, "Optimization of three-dimensional micropost microcavities for cavity quantum electrodynamics," Phys. Rev. A **66**, 023 808 (2002).

[155] T. Pellizzari, S. Gardiner, J. Cirac, and P. Zoller, "Decoherence, continous obervation, and quantum computing: a cavity QED model," Phys. Rev. Lett. **75**, 3788 (1995).

[156] J. I. Cirac, P. Zoller, H. J. Kimble, and H. Mabuchi, "Quantum state transfer and entanglement distribution among distant nodes in a quantum network," Phys. Rev. Lett. **78**, 3221 (1997).

[157] A. Kiraz, C. Reese, B. Gayral, L. Zhang, W. V. Schoenfeld, B. D. Gerardot, P. M. Petroff, E. L. Hu, and A. Imamoglu, "Cavity-quantum electrodynamics with quantum dots," J. Opt. B: Quantum Semiclass. Opt. **5**, 129 (2003).

[158] T. M. Stace, G. J. Milburn, and C. H. W. Barnes, "Entangled two-photon source using biexciton emission of an asymmetric quantum dot in a cavity," Phys. Rev. B **67**, 085 317 (2003).

[159] D. Bouwmeester, A. Ekert, and A. Zeilinger, *The Physics of Quantum Information* (Springer, Berlin, 2000).

[160] C. H. Bennett, G. Brassard, and A. Eckert, "Quantum cryptography," Sci. Am. **267**(4), 50 (1992).

[161] R. J. Hughes, J. E. Nordholt, D. Derkacs, and C. G. Peterson, "Practical free-space quantum key distribution over 10 km in daylight and at night," New J. Phys. **4**, 43 (2002).

[162] K. J. Resch, M. Lindenthal, B. Blauensteiner, H. R. Bohm, A. Fedrizzi, C. Kurtsiefer, A. Poppe, T. Schmitt-Manderbach, M. Taraba, R. Ursin, P. Walther, H. Weier, H. Weinfurter, and A. Zeilinger, "Distributing entanglement and single photons through an intra-city, free-space quantum channel," Opt. Express **13**, 202 (2005).

[163] C. Z. Peng, T. Yang, X. H. Bao, J. Zhang, X. M. Jin, F. Y. Feng, B. Yang, J. Yang, J. Yin, Q. Zhang, N. Li, B. L. Tian, and J. W. Pan, "Experimental free-space distribution of entangled photon pairs over 13 km: towards satellite-based global quantum communication," Phys. Rev. Lett. **94**, 150 501 (2005).

[164] L. Allen and J. H. Eberly, *Optical Resonance and Two-Level Atoms* (Dover Publication Inc., New York, 1987), Ch. 3 Two-level atoms in steady fields, pp. 52–77.

[165] E. T. Jaynes and F. W. Cummings, "Comparison of quantum and semiclassical radiation theories with application to the beam maser," Proceedings of the IEEE **51**, 89 (1963).

[166] V. Weisskopf and E. Wigner, "Berechnung der naturlichen Linienbreite auf Grund der Diracschen Lichttheorie," Z. Phys. **63**, 54 (1930).

[167] M. O. Scully and M. S. Zubairy, *Quantum Optics* (Cambridge, New York, 1997), Ch. 6 Atom-field interaction — quantum theory, pp. 193–219.

[168] H. J. Carmichael, *Statistical Methods in Quantum Optics 1* (Springer, New York, 1999), pp. 20–24 and 287–302.

[169] S. E. Morin, "Strong atom-electromagnetic mode coupling in quantum optics : applications in cavity quantum electrodynamics," Ph.D. thesis, University of Oregon, Eugene, OR, USA (1994).

[170] X. Fan, "Cavity-QED studies of composite semiconductor nanostructure and dielectric microsphere systems," Ph.D. thesis, University of Oregon, Eugene, OR, USA (2000).

[171] S. Y. Kilin and T. B. Karlovich, "Single-atom laser: coherent and nonclassical effects in the regime of a strong atom-field correlation," J. Exp. & Theo. Phys. **95**, 805 (2002).

[172] C. K. Law and H. J. Kimble, "Deterministic generation of a bit-stream of single-photon pulses," J. Mod. Opt. **44**, 2067 (1997).

[173] L. A. Lugiato, "Theory of optical bistability," in *Progress in Optics*, E. Wolf, ed., Vol. XXI (Elsevier Science Publishers B.V., New York, 1984), pp. 69–216.

[174] B. Lounis and M. Orrit, "Single-photon sources," Rep. Prog. Phys. **68**, 1129 (2005).

[175] M. Pelton, C. Santori, J. Vuckovic, B. Zhang, G. S. Solomon, J. Plant, and Y. Yamamoto, "Efficient source of single photons: a single quantum dot in a micropost microcavity," Phys. Rev. Lett. **89**, 233 602 (2002).

[176] L. Mandel and E. Wolf, *Optical Coherence and Quantum Optics* (Cambridge University Press, New York, 1997), pp. 21–39 and 56–65.

[177] H. J. Carmichael, R. J. Brecha, M. G. Raizen, and H. J. Kimble, "Subnatural linewidth averaging for coupled atomic and cavity-mode oscillators," Phys. Rev. A **40**, 5516 (1989).

[178] T. Takagahara, "Theory of exciton coherence and decoherence in semiconductor quantum dots," in *Quantum Coherence, Correlation and Decoherence in Semiconductor Nanostructures*, T. Takagahara, ed. (Academic Press, San Diego, 2003), pp. 395–470.

[179] K. Wodkiewicz, "Stochastic incoherences of optical Bloch equations," Phys. Rev. A **19**, 1686 (1979).

[180] K. Kubo, "A stochastic theory of line-shape and relaxation," in *Fluctuation, Relaxation and Resonance in Magnetic Systems*, D. ter Haar, ed. (Oliver and Boyd, Edinberg, 1962), pp. 23–68.

[181] R. F. Fox, "Contributions to the theory of multiplicative stochastic processes," J. Math. Phys. **13**, 1196 (1972).

[182] K. Wodkiewicz, "Exact solutions of some multiplicative stochastic processes," J. Math. Phys. **20**, 45 (1979).

[183] M. Lax, "Formal theory of quantum fluctuations from a driven state," Phys. Rev. **129**, 2342 (1963).

[184] D. Bimberg, M. Grundmann, and N. N. Ledentsov, *Quantum Dot Heterostructures* (John Wiley, Chichester, 1999).

[185] H. Z. Song, T. Usuki, S. Hirose, K. Takemoto, Y. Nakata, N. Yokoyama, and Y. Sakuma, "Site-controlled photoluminescence at telecommunication wavelength from InAs/InP quantum dots," Appl. Phys. Lett. **86**, 113118 (2005).

[186] P. Atkinson, M. B. Ward, S. P. Bremner, D. Anderson, T. Farrow, G. A. C. Jones, A. J. Shields, and D. A. Ritchie, "Site-Control of InAs Quantum Dots using *Ex-Situ* Electron-Beam Lithographic Patterning of GaAs Substrates," Jpn. J. Appl. Phys. **45**, 2519 (2006).

[187] F. Jelezko and J. Wrachtrup, "Single defect centers in diamond: A review," Phys. Stat. Sol. (a) **203**, 3207 (2006).

[188] Y.-S. Park, A. K. Cook, and H. Wang, "Cavity QED with diamond nanocrystals and silica microspheres," Nano Lett. **6**, 2075 (2006).

[189] P. W. May, "Diamond thin films: A 21st-century material," Phil. Trans. R. Soc. Lond. A **358**, 473 (2000).

[190] J. R. Rabeau, Y. L. Chin, S. Prawer, F. Jelezko, T. Gaebel, and J. Wrachtrup, "Fabrication of single nickel-nitrogen defects in diamond by chemical vapor deposition," Appl. Phys. Lett. **86**, 131926 (2005).

[191] T. Plakhotnik, "Simple microcavity for single-photon generation," Opt. Express **13**, 3049 (2005).

[192] S. Tomljenovic-Hanic, M. J. Steel, C. M. de Sterke, and J. Salzman, "Diamond based photonic crystal microcavities," Opt. Express **14**, 3556 (2006).

[193] D. P. Poenar and R. F. Wolffenbuttel, "Optical properties of thin-film silicon-compatible materials," Applied Optics **36**, 5122 (1997).

[194] K. Mallika and R. Komanduri, "Low pressure microwave plasma assisted chemical vapor deposition (MPCVD) of diamond coating on silicon nitride cutting tools," Thin Solid Films **396**, 145 (2001).

[195] G. T. Kiehne, G. K. L. Wong, and J. B. Ketterson, "Optical second-harmonic generation in sputter-deposited AlN films," J. Appl. Phys. **84**, 5922 (1998).

[196] H. Joo, H. J. Kim, S. J. Kim, and S. Y. Kim, "Spectrophotometric analysis of aluminum nitride thin films," J. Vac. Sci. Technol. A **17**, 862 (1999).

[197] M. Centini, G. D'Agugnno, M. Scalora, C. Sibilia, M. Bertolotti, M. J. Bloemer, and C. M. Bowden, "Simultaneously phase-matched enhanced second and third harmonic generation," Phys. Rev. E **64**, 046 606 (2001).

[198] S. Eriksson, M. Trupke, H. F. Powell, D. Sahagun, C. D. J. Sinclair, E. A. Curtis, B. Sauer, E. A. Hinds, Z. Moktadir, C. O. Gollasch, and M. Kraft, "Integrated optical components on atom chips," Eur. Phys. J. D **35**, 135 (2005).

[199] M. Trupke, J. Metz, A. Beige, and E. A. Hinds, "Towards quantum computing with single atoms and optical cavities on atom chips," J. Mod. Optics **54**, 1639 (2007).

[200] O. Benson, C. Santori, M. Pelton, and Y. Yamamoto, "Regulated and entangled photons from a single quantum dot," Phys. Rev. Lett. **84**, 2513 (2000).

[201] N. Akopian, N. H. Lindner, E. Poem, Y. Berlatzky, J. Avron, D. Gershoni, B. D. Gerardot, and P. M. Petroff, "Entangled photon pairs from semiconductor quantum dots," Phys. Rev. Lett. **96**, 130 501 (2006).

[202] "Capillary Tubing (Microcaps)," URL `http://www.drummondsci.com/`.

[203] "Kimble Glasses," URL `http://208.72.236.210/html/TechInfo.html`.

[204] "Grinding/Polishing Consumables," URL `http://www.alliedhightech.com/`.

[205] "Crystalbond 509," URL `http://www.crystalbond.com/`.

[206] H. C. Torrey, "Transient nutations in nuclear magnetic resonance," Phys. Rev. **76**, 1059 (1949).

[207] L. Allen and J. H. Eberly, *Optical Resonance and Two-Level Atoms* (Dover Publication Inc., New York, 1987), pp. 62–67.

[208] E. W. Weisstein, "Cubic Equation," from Mathworld – A Wolfram Web Resource. URL http://mathworld.wolfram.com/CubicEquation.html.

[209] E. W. Weissteim, "Quartic Equation," from Mathworld – A Wolfram Web Resource. URL http://mathworld.wolfram.com/QuarticEquation.html.